

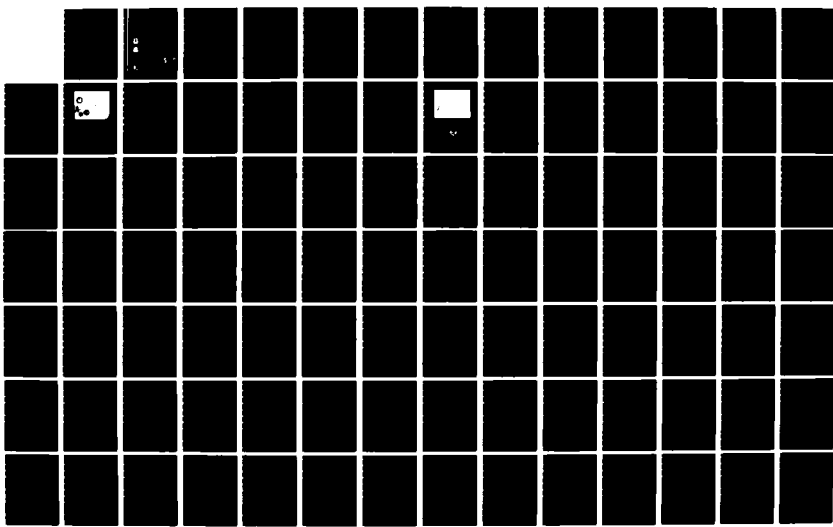
AD-A160 504 CRRES/SPACERAD (COMBINED RELEASE AND RADIATION EFFECTS 1/2
SATELLITE/SPACE RA (U) AIR FORCE GEOPHYSICS LAB
HANSCOM AFB MA M S GUSSENHOVEN ET AL 24 JAN 85

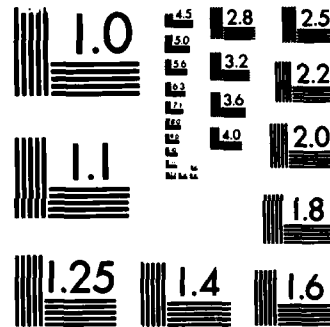
UNCLASSIFIED

AFGL-TR-85-0017

F/G 22/1

NL





MICROCOPY RESOLUTION TEST CHART
NATIONAL BUREAU OF STANDARDS-1963-A

AFGL-TR-85-0017
ENVIRONMENTAL RESEARCH PAPERS, NO. 908

AD-A160 504

CRRES/SPACERAD Experiment Descriptions

Editors:

M. S. GUSSENHOVEN
E. G. MULLEN
R. C. SAGALYN



24 January 1985



Approved for public release; distribution unlimited.



DTIC FILE COPY



SPACE PHYSICS DIVISION
AIR FORCE GEOPHYSICS LABORATORY
HANSOM AFB, MA 01731
PROJECT 7601

DTIC
SELECTED
OCT 22 1985
S A D

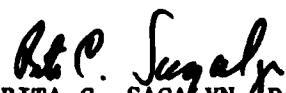
85 10 22 035

"This technical report has been reviewed and is approved for publication"

FOR THE COMMANDER



E. G. MULLEN, Chief
Space Particles Environment Branch
Space Physics Division



RITA C. SAGALYN, Director
Space Physics Division

This report has been reviewed by the ESD public Affairs Office (PA) and is releasable to the National Technical Information Services (NTIS).

Qualified requestors may obtain additional copies from the Defense Technical Information Center. All others should apply to the National Technical Information Service.

If your address has changed, or if you wish to be removed from the mailing list, or if the addressee is no longer employed by your organization, please notify AFGL/DAA, Hanscom AFB, MA 01731. This will assist us in maintaining a current mailing list.

Unclassified

AD-A160 524

SECURITY CLASSIFICATION OF THIS PAGE

REPORT DOCUMENTATION PAGE					
1a. REPORT SECURITY CLASSIFICATION Unclassified		1b. RESTRICTIVE MARKINGS			
2a. SECURITY CLASSIFICATION AUTHORITY		3. DISTRIBUTION/AVAILABILITY OF REPORT Approved for public release; distribution unlimited			
2b. DECLASSIFICATION/DOWNGRADING SCHEDULE					
4. PERFORMING ORGANIZATION REPORT NUMBER(S) AFGL-TR-85-0017 ERP, No. 906		5. MONITORING ORGANIZATION REPORT NUMBER(S)			
6a. NAME OF PERFORMING ORGANIZATION Air Force Geophysics Laboratory	6b. OFFICE SYMBOL (If applicable) PHP	7a. NAME OF MONITORING ORGANIZATION Air Force Geophysics Laboratory (PHP)			
6c. ADDRESS (City, State and ZIP Code) Hanscom AFB Massachusetts 01731		7b. ADDRESS (City, State and ZIP Code) Hanscom AFB Massachusetts 01731			
8a. NAME OF FUNDING/SPONSORING ORGANIZATION	8b. OFFICE SYMBOL (If applicable)	9. PROCUREMENT INSTRUMENT IDENTIFICATION NUMBER			
8c. ADDRESS (City, State and ZIP Code)		10. SOURCE OF FUNDING NOS.			
11. TITLE (Include Security Classification) CRRES/SPACERAD Experiment Descriptions		PROGRAM ELEMENT NO. 62101F	PROJECT NO. 7601	TASK NO. 20	WORK UNIT NO. 01
12. PERSONAL AUTHOR(S) Editors: Gussenhoven, M.S., Mullen, E.G., Sagalyn, R.C.					
13a. TYPE OF REPORT Scientific Interim	13b. TIME COVERED FROM 1/10/84 TO 15/1/85	14. DATE OF REPORT (Yr., Mo., Day) 1985 January 24		15. PAGE COUNT 185	
16. SUPPLEMENTARY NOTATION <i>(cont'd on back)</i>					
17. COSATI CODES		18. SUBJECT TERMS (Continue on reverse if necessary and identify by block number) Space radiation; Protons; Spacecraft charging; Space experiments; Electrons; Radiation damage; Energetic particles; Ions; Microelectronics			
19. ABSTRACT (Continue on reverse if necessary and identify by block number) The Air Force Geophysics Laboratory (AFGL) Space Radiation Effects (SPACERAD) Program is a comprehensive space program whose purposes, among other things, are to: (a) measure radiation-induced single event upsets (SEUs) and total-dose degradation of state-of-the-art microelectronic devices (to include VHSIC and GaAs devices) in a known space environment; (b) space qualify advanced technology microelectronic devices for operational DOD satellite systems; and (c) update the static models of the radiation belts and develop the first dynamic models of the high energy particle populations in the near-Earth environment. To accomplish these goals, AFGL has developed a space experiment complement consisting of a microelectronics experiment package (MEP), dosimeters, energetic-particle detectors, space plasma detectors, and wave and field (electric and magnetic) instruments. The experiments are to be flown as a package on the Joint Air Force (Contd)					
20. DISTRIBUTION/AVAILABILITY OF ABSTRACT UNCLASSIFIED/UNLIMITED <input checked="" type="checkbox"/> SAME AS RPT. <input type="checkbox"/> DTIC USERS <input type="checkbox"/>		21. ABSTRACT SECURITY CLASSIFICATION Unclassified			
22a. NAME OF RESPONSIBLE INDIVIDUAL M. S. Gussenhoven		22b. TELEPHONE NUMBER (Include Area Code) 617-861-3213	22c. OFFICE SYMBOL PHP		

DD FORM 1473, 83 APR

EDITION OF 1 JAN 73 IS OBSOLETE.

Unclassified

SECURITY CLASSIFICATION OF THIS PAGE

For me
Unclassified

SECURITY CLASSIFICATION OF THIS PAGE

Block 19 (Contd).

NASA Combined Release and Radiation Effects Satellite (CRRES) in FY87. The MEP will record SEUs and radiation degradation as a function of orbital position, particle type, device geometry, device technology, device material, device operating conditions, etc. The other instrumentation will be used to simultaneously measure the space environment. This document gives a brief description of the SPACERAD Program and the instruments to be flown on CRRES, to meet the program objectives.

→ Keywords ()

Unclassified

SECURITY CLASSIFICATION OF THIS PAGE

Acknowledgements

We would like to thank the authors and principal investigators of the individual sections for their timely inputs. We also thank Nancy Heinemann of Boston College for editing the manuscript, Anne Novak for manuscript preparation, and Margaret Anderson for typing assistance.

Approved for	
NTIS	CRA&I
DTIC	TAB
Unannounced	
Justification	
By _____	
Distribution/	
Availability Codes	
Dist	Avail and/or Special
A1	

Contents

I.	INTRODUCTION	1
II.	ORBITAL AND SPACECRAFT PARAMETERS	9
III.	ENGINEERING EXPERIMENTS	13
	OVERVIEW	13
1.	THE SPACERAD MICROELECTRONICS EXPERIMENT (AFGL-701-1A), James C. Ritter, Arthur B. Campbell, Robert Wettingfeld, William B. Huber, Warren C. Tolman, and Richard Gonyea	15
2.	THE INTERNAL DISCHARGE MONITOR (AFGL-701-1B) P. Robinson and J. M. Conley	27
3.	THE GALLIUM ARSENIDE SOLAR CELL PANEL EXPERIMENT (AFAPL-801) Terry M. Trumble	35
IV.	COLD PLASMA AND FIELDS AND WAVES	41
	OVERVIEW	41
4.	THE FLUXGATE MAGNETOMETER (AFGL-701-13-1) Howard J. Singer and Frederick J. Rich	43

5. THE PASSIVE PLASMA SOUNDER (AFGL-701-15) AND SEARCH COIL MAGNETOMETER (AFGL 701-13-2) Roger R. Anderson and Donald A. Gurnett	45
6. THE LANGMUIR PROBE INSTRUMENT (AFGL-701-14) W. J. Burke, W. P. Sullivan, M. Smiddy, J. R. Wygant, P. R. Harvey, F. S. Mozer, R. B. Torbert, M. C. Kelley, and N. Maynard	55
V. PARTICLE EXPERIMENTS	65
OVERVIEW	65
7. THE LOW ENERGY PLASMA ANALYZER (AFGL-701-6) D. A. Hardy, A. D. Johnstone, M. F. Smith, P. Gough, A. Huber, J. Pantazis, and R. Burkhardt	69
8. THE MEDIUM ENERGY ELECTRON AND PROTON SPECTROMETERS (AFGL-701-5), Axel Korth, S. Ullaland, and A. Vampola	77
9. THE SPECTROMETER FOR ELECTRONS AND PROTONS (ONR-307-3), J. B. Reagan, E. E. Gaines, S. J. Battel, D. A. Simpson, W. L. Imhof, and R. R. Vondrak	87
10. THE PROTON TELESCOPE (AFGL-701-8, AFGL-701-9) Kevin Riehl, D. A. Hardy, and Ed Boughan	97
11. THE HIGH ENERGY ELECTRON FLUXMETER (AFGL-701-4) D. A. Hardy, F. Hanser, and B. Sellers	111
12. THE RELATIVISTIC PROTON DETECTOR (AFGL-701-7A) A. Kolasinski	121
13. THE PROTON SWITCH (AFGL-701-7B), J. B. Blake	125
14. THE MASS COMPOSITION INSTRUMENTS (AFGL-701-11) T. A. Fritz, D. T. Young, W. C. Feldman, S. J. Bame, J. R. Cessna, D. N. Baker, B. Wilken, W. Studeman, P. Winterhoff, D. A. Bryant, D. S. Hall, J. F. Fennell, D. Chenette, N. Katz, S. I. Imamoto, R. Koga, and F. Soeraas	127
15. THE LOW ENERGY ION MASS SPECTROMETER (ONR-307-8-1, ONR-307-8-2), J. M. Quinn, E. G. Shelley, S. J. Battel, E. Hertzberg, S. Roselle, and T. C. Sanders	141
16. THE MEDIUM ENERGY ION MASS SPECTROMETER (ONR-307-8-3) H. D. Voss, E. G. Shelley, A. G. Ghielmetti, E. Hertzberg, S. J. Battel, K. L. Appert, and R. R. Vondrak	153

17. THE EXPERIMENT FOR HIGH ENERGY, HEAVY NUCLEI COMPOSITION (ONR-604), J.A. Simpson, M.G. Munoz, M. Perkins, and J.P. Wefel	163
18. THE SPACE RADIATION DOSIMETER (AFGL-701-2) D.A. Hardy, F. Hanser, and B. Sellers	175
19. THE MOS DOSIMETER (AFGL-701-3), Leon S. August and James C. Ritter	181

Illustrations

1. Schematic of the CRRES/SPACERAD Program (Section I)	3
2. Sequence of the CRRES Mission (Section II)	10
3. Model of the CRRES Satellite (Section II)	10
4. Cut-Away View of the CRRES Satellite With Placement of Experiments, Booms, and Chemicals (Section II)	11
5. Configuration of the Assembled Microelectronics Flight Package (Paper No. 1)	20
6. Single-Cell Configuration in the Microelectronics Package (Paper No. 1)	21
7. Eggcrate-Cell Configuration and Numbering Scheme for Microelectronics Package (Paper No. 1)	21
8. Function Block Diagram for Microelectronics Package (Paper No. 1)	24
9. Peak Voltage Detector Characteristics as a Function of Pulse Width (Paper No. 2)	28
10. Dielectric Sample Test Configuration for the Internal Discharge Monitor (Paper No. 2)	30
11. Function Block Diagram for the Internal Discharge Monitor (Paper No. 2)	32
12. Schematic Overview of the Gallium Arsenide Solar Cell Panel Experiment (Paper No. 3)	38
13. Schematic Variation of Characteristic Plasma Frequencies as a Function of Radial Distance From the Earth (Paper No. 5)	46
14. Function Block Diagram for the Plasma Wave Experiment (Paper No. 5)	49
15. Frequency Response Curves for the 14 Channels of the Multichannel Spectrum Analyzer in the Plasma Wave Experiment (Paper No. 5)	52
16. Function Block Diagram for the Langmuir Probe Instrument (Paper No. 6)	59
17. Individual Energy Ranges for Electron Experiments (Section V)	67
18. Individual Energy Ranges for Ion Experiments (Section V)	67
19. Schematic Diagram of the Low Energy Plasma Sensor Showing Trajectories Within the Detector for Particles Incident at Two Different Directions (Paper No. 7)	72

Illustrations

20. Function Block Diagram for Low Energy Plasma Analyzer (Paper No. 7)	74
21. Schematic of Collimator and Magnetic Shielding Can for Electron-Proton-Angle Spectrometer (Paper No. 8)	78
22. Schematic of the Magnetic Deflection System and Detectors in the Electron-Proton-Angle Spectrometer (Paper No. 8)	80
23. Function Block Diagram for the Electron-Proton-Angle Spectrometer (Paper No. 8)	83
24. Schematic Diagram of the Analyzing Chamber of the Medium Electron Sensor (Paper No. 8)	84
25. Electronic Logic for Each Channel in the Medium Electron Sensor (Paper No. 8)	85
26. Cross-Section View of the SCATHA SC-3 Energetic Electron/Proton Spectrometer Showing the Various Sensor Elements and the Long Collimator (Paper No. 9)	90
27. Mechanical Arrangement of the Three SEP Telescopes (Paper No. 9)	91
28. Function Block Diagram of the ONR-307-3 SEP Instrument (Paper No. 9)	92
29a. Schematic of the Proton Telescope High Energy Sensor Head (Paper No. 10)	100
29b. Schematic of the Proton Telescope Low Energy Sensor Head (Paper No. 10)	100
30a. Energy Deposition as a Function of Energy for High Mass Particles in the PROTEL Detector (Paper No. 10)	103
30b. Energy Deposition as a Function of Energy for Protons in the PROTEL Low Energy Sensor (Paper No. 10)	103
30c. Energy Deposition as a Function of Energy for Protons in the PROTEL High Energy Sensor (Paper No. 10)	104
31. Function Block Diagram for the PROTEL High Energy Sensor (Paper No. 10)	106
32. Schematic of the High Energy Electron Fluxmeter Sensor Head (Paper No. 11)	114
33. Function Block Diagram for the High Energy Electron Fluxmeter (Paper No. 11)	118
34. Schematic Diagram of sensors in the AFGL-701-7A Package: (a) Cerenkov Counter; (b) Electron Detector; (c) Photometer (Paper No. 12)	123
35. Schematic Diagram of the Proton Switch (Paper No. 13)	126
36. Schematic of the Proton Switch Sensor (Paper No. 13)	126
37. Schematic of the Low Energy Magnetospheric Ion Composition Sensor (LOMICS) (Paper No. 14)	130
38. Schematic Diagram of the Magnetospheric Ion Composition Sensor (MICS) (Paper No. 14)	132
39. Function Block Diagram of the Magnetospheric Ion Composition Sensor (MICS) (Paper No. 14)	133

Illustrations

40. Schematic Diagram of the Heavy Ion Telescope (HIT) (Paper No. 14)	134
41. Function Block Diagram for the Low Energy Magnetospheric Ion Composition (LOMICS) and the Heavy Ion Telescope (HIT) Experiments (Paper No. 14)	135
42. Function Block Diagram for the Data Processing Unit (DPUA) for the Magnetospheric Ion Composition (MICS) Experiment (Paper No. 14)	136
43. Function Block Diagram for the Data Processing Unit (DPUB) for the Heavy Ion Telescope (HIT) (Paper No. 14)	138
44. Function Block Diagram for the Data Processing Unit (DPUB) for the Low Energy Magnetospheric Ion Composition (LOMICS) Experiment (Paper No. 14)	139
45. Schematic Illustration of Ion Mass and Energy Analysis Optics for the Low Energy Ion Mass Spectrometer (IMS-LO) (Paper No. 15)	145
46. Mass Peak Shapes for the Wein Filter Spectrometer (Paper No. 15)	146
47. Schematic Illustration of the Electron Detector for the Low Energy Ion Mass Spectrometer (IMS-LO) (Paper No. 15)	148
48. Function Block Diagram for One of the Two Identical Low Energy Ion Mass Spectrometers (IMS-LO) (Paper No. 15)	150
49. Schematic Diagram of the Medium Energy Ion Mass Spectrometer (IMS-HI) (Paper No. 16)	156
50. Position-Energy Plot for the Medium Energy Ion Mass Spectrometer (IMS-HI) for Singly Charged Ions in a 7-kG Magnetic Field (Paper No. 16)	157
51. Function Block Diagram for the Medium Energy Ion Mass Spectrometer (IMS-HI) (Paper No. 16)	158
52. Schematic of the Cross Section of the Charged Particle Telescope in the Experiment for High Energy, Heavy Nuclei Composition (Paper No. 17)	165
53. Schematic of the Position Sensing Detector (Paper No. 17)	166
54. Kinetic Energy Intervals for Given Detector Penetration Ranges for Isotopes H ¹ Through Ni ⁵⁹ (Paper No. 17)	170
55. Function Block Diagram for the High Energy, Heavy Nuclei Composition Experiments (Paper No. 17)	172
56. Schematic Diagram of One of the Four Sensors of the Space Radiation Dosimeter (Paper No. 18)	177
57. Function Block Diagram for the Space Radiation Dosimeter (Paper No. 18)	179
58. Function Block Diagram for the MOS Dosimeter (Paper No. 19)	183

Tables

1. SPACERAD Experiments (Section I)	7
2. SPACERAD Instrument Locations and Line of Sight (Section II)	12
3. Internal Discharge Monitor: Sample Materials, Thicknesses, and Configuration (Paper No. 2)	31
4. Internal Discharge Monitor: Event Statistics (Paper No. 2)	33
5. Plasma Wave Experiment: Sweep Frequency Receiver Noise Levels and Minimum Detectable Sine Wave Amplitudes (Paper No. 5)	50
6. Discrete Frequencies for the CRRES Plasma Wave Experiment Frequency Receiver in kHz (Paper No. 5)	51
7. Plasma Wave Experiment: Multichannel Spectrum Analyzer Characteristics (Paper No. 5)	52
8. Langmuir Probe: Main Telemetry Quantities (Paper No. 6)	61
9. Langmuir Probe: Burst Telemetered Quantities (Paper No. 6)	62
10. Particle Detector Characteristics (Section V)	66
11. Electron-Proton-Angle Spectrometer Specifications (Paper No. 8)	82
12. Medium Energy Electron Spectrometer: Energy Ranges and Geometric Energy Factors (Paper No. 8)	86
13. Spectrometer for Electrons and Protons: Typical Operating Modes (Paper No. 9)	93
14. Prototype Proton Telescope Detector Stacks (Paper No. 10)	101
15. Proton Telescope: Coincidence Scheme (High Energy) (Paper No. 10)	104
16. Proton Telescope: Detector Assembly Energies in MeV (Paper No. 10)	107
17. High Energy Electron Fluxmeter: Channel Geometric Factors and Particle Detection Ranges (Paper No. 11)	116
18. Mass Composition Instrument Parameters (Paper No. 14)	129
19. Experiment for High Energy, Heavy Nuclei Composition: Vital Statistics (Paper No. 17)	168
20. Experiment for High Energy, Heavy Nuclei Composition: Telescope Geometry and Counting Rates (Paper No. 17)	169

Contents

1. Flight Experiments	2
2. Ground Test Programs	4
3. Modeling	5
4. Summary	6

CRRES/SPACERAD Experiment Descriptions

I. Introduction

The Combined Release and Radiation Effects Satellite (CRRES) Program is a joint U.S. Air Force/National Aeronautics and Space Administration (NASA) program to perform chemical releases in the near-Earth environment and to measure the near-Earth radiation environment and its effects on state-of-the-art microelectronics devices and other spacecraft components. The CRRES Program is jointly managed by the Air Force Space Test Program Office at Space Division (SD/YC) and the NASA Marshall Spaceflight Center. The program is mutually beneficial to both agencies because both perform missions in and through near-Earth space.

The CRRES Program supports, among other experiments, the Air Force Geophysics Laboratory (AFGL) Space Radiation Effects Program (SPACERAD). The SPACERAD Program is a comprehensive space- and ground-test program to:

(a) measure radiation-induced single event upsets (SEUs) and total dose degradation of state-of-the-art microelectronic devices [to include VHSIC (Very High Speed Integrated Circuit) and gallium arsenide (GaAs) devices] in a known space environment;

(b) perform laboratory radiation response and annealing characterizations of parts identical to those which are space tested, and model selected devices for total dose, dose rate, and SEU effects;

(c) develop algorithms to relate space performance of microelectronic compo-

(Received for publication 23 January 1985)

nents to ground test procedures, and update existing radiation ground test guidelines to simulate more accurately the space behavior of microelectronic devices;

(d) space qualify advanced technology microelectronic devices for use in operational DOD satellite systems; and

(e) update the static models of the radiation belts and develop the first dynamic models of the high energy particle populations in the near-Earth environment.

To accomplish the SPACERAD mission goals, AFGL has developed a space experiment complement consisting of a microelectronics experiment package (MEP), dosimeters, energetic particle detectors, space plasma detectors, and wave and field (electric and magnetic) instruments. The experiments are to be flown as a package on CRRES in FY87. The MEP will record SEUs and radiation degradation as a function of orbital position, particle type, device geometry, device technology, device material, device operating conditions, etc. The other instrumentation will simultaneously measure the space environment.

During the SPACERAD portion of the mission, the CRRES satellite will have a low inclination (less than 20 degrees), highly elliptical (400 km to 36,600 km) orbit that will traverse the most radiation intense regions of the Earth's inner (proton dominated) and outer (electron dominated) radiation belts. The satellite's three-year mission goal is to attain a statistically significant data set for the empirical analyses. The CRRES satellite is being built by Ball Aerospace Systems Division under a NASA/Marshall contract. The Air Force Space Test Program Office at Space Division is the DOD focal point for the satellite fabrication and integration.

The SPACERAD Program can be broken up into three main areas, the flight experiments, the ground test programs, and the modeling efforts (Figure 1). The flight experiments from SPACERAD and other supporting DOD programs will be discussed at length in their various sections. Here, however, we present a brief overview of the SPACERAD Program areas.

1. FLIGHT EXPERIMENTS

1.1 Microelectronics Package

Because the MEP is the critical mission payload for a successful SPACERAD mission, great care is being taken to develop an optimal experiment. A working team of experts in radiation hardness electronics testing has been established to oversee the design and fabrication of the package, as well as to select the appropriate devices for testing and to develop appropriate space test procedures. The working team consists of physicists and engineers from the Naval Research Laboratory (NRL), Rome Air Development Center (RADC), Air Force Weapons Laboratory (AFWL), NASA, Jet Propulsion Laboratory (JPL), The Aerospace Corporation,

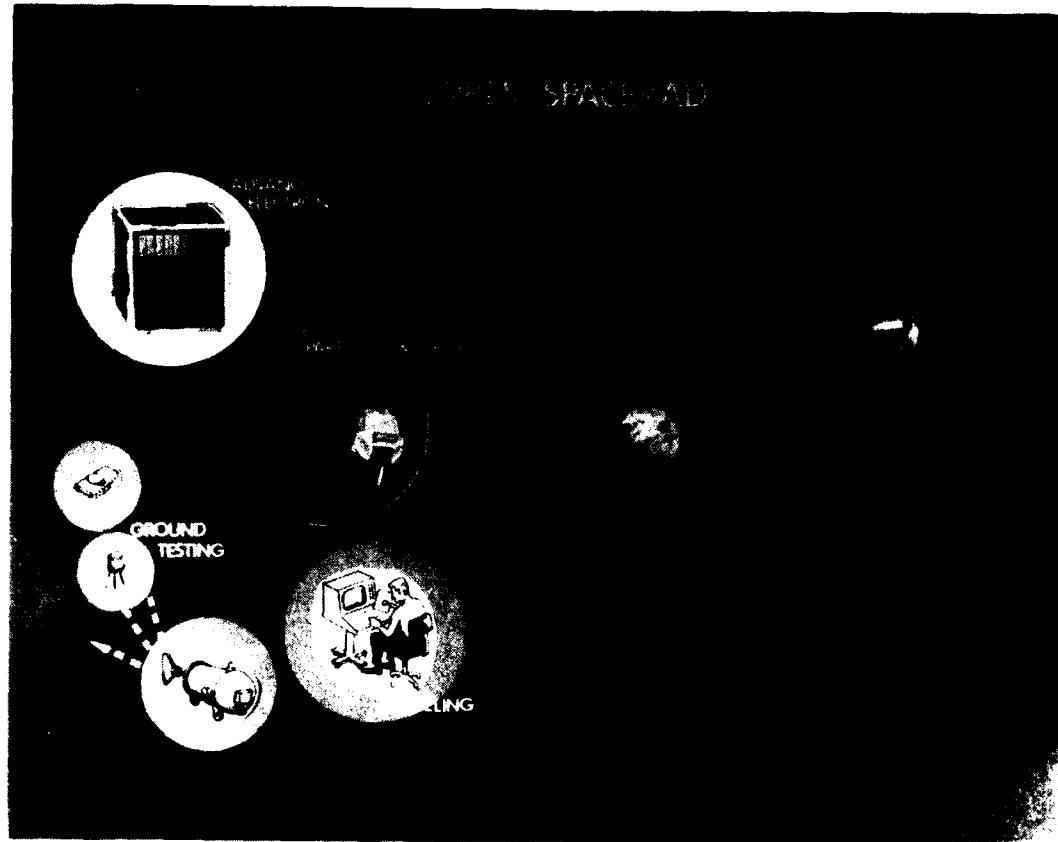


Figure 1. Schematic of the CRRES/SPACERAD Program

Sandia National Laboratory, Defense Nuclear Agency (DNA), Defense Advanced Research Projects Agency (DARPA), industry, and universities. The devices to be tested include RAMs, microprocessors, PROMs, ADCs, latches, inverters, gate arrays, and special test circuits. The special test circuits are devices being developed by JPL and NRL to test, on a single chip, different geometries, feature sizes, and technologies. These devices should give us much needed insight into device behavior for radiation modeling. The total test package device complement includes approximately 65 device types and over 450 total test devices.

The MEP is jointly funded by the Air Force, the Navy, DNA, DARPA, and NASA because it has wide ranging implications for future space systems. DARPA is using the MEP to test its new gallium arsenide (GaAs) RAMs to verify their intrinsic total dose hardness and to get valuable information on their single event upset (SEU) response. DNA is using the MEP to test several of its new processes to harden chips. NASA is testing several specially designed CMOS chips to better

understand both SEU and total dose radiation degradation processes. The Navy and the Air Force want data on devices presently planned for operational space systems. VHSIC chips are being tested to obtain some early data on their radiation response in space so their radiation characteristics can be better modeled and their applicability for future space systems can be determined. Thus, the MEP will test for total dose and SEU over a wide range of device types and technologies important to the entire U.S. space community.

1.2 Particle Detectors

The particle detectors will measure the complete particle spectrum of electrons, protons, and ions from a few eV to hundreds of MeV. About 20 separate instruments will make the measurements. The time and spatial resolution of the measurements will be the best ever measured over the entire energy spectrum from a single satellite. The particle measurements will provide the data necessary to determine the cause and effect relationships between microelectronic performance and the space environment, since the two will be measured simultaneously. Direct measurements of the accumulated dose will also be available to assess microelectronic performance and to test radiation transport codes.

1.3 Plasma and Wave Experiments

Two sets of 100 m tip-to-tip booms will measure the electric fields and plasma density in the vicinity of the spacecraft. A fluxgate magnetometer will determine dc magnetic fields, and a search coil magnetometer will measure ac magnetic fields. The plasma and wave experiment data coupled with the particle data will be used to study the wave-particle interactions (WPI) and dynamics that are responsible for the filling and dumping of the radiation belts. These data will be used to produce the first dynamic models of the radiation belts.

2. GROUND TEST PROGRAMS

An equally important part of the total experiment is the ground testing. Without the ground test data, the space data is of limited use. To demonstrate the relationships between ground and flight test results, the devices to be compared should be manufactured at the same time under identical conditions. Therefore, device manufacturers have been requested to supply devices from the same wafer (lot) whenever possible and to include full documentation of the fabrication and test procedures.

2.1 SEU Ground Testing

The SEU ground testing will be performed by JPL and The Aerospace Corporation at suitable accelerator facilities. All device types will receive irradiations sufficient to determine the linear energy transfer (LET) threshold and maximum cross section at high LET for the device. The test species will range from 130 MeV krypton ions to about 30 MeV protons depending on the device susceptibility.

2.2 Total Dose Testing

In the total dose area, there are indications that present laboratory test techniques do not accurately reflect dose degradation in space. Current Mil Standard radiation tests with Co60 do not accurately represent the full spectrum of the particle environment seen in space, and the high dose rate testing does not properly account for annealing in the space environment. The total dose ground tests will consist of standard 883B Co60 tests as well as Co60 tests at lower dose rates, and proton and electron tests at both accelerated dose rates and dose rates comparable to those measured in space. The devices irradiated by Co60 will be stored under bias and allowed to anneal over one year, with post irradiation characterizations made at scheduled intervals.

2.3 Special Testing

A limited amount of special testing with high energy electrons and protons will be performed to address questions of interface state production, charge trapping, dose enhancement, and total-dose effects on SEU sensitivities.

3. MODELING

Both device modeling and environment modeling will be performed.

3.1 Device Modeling

Device modeling will provide the foundation for predicting both SEUs and space life expectancy for electronic components in the space environment. The modeling effort will not duplicate other more comprehensive modeling programs such as the DNA/DARPA Tree Core Single Event Program, but will verify and improve existing models and modeling techniques using the space test data. The modeling effort will pay particular attention to providing methods for devices still to be developed and not just those specific devices tested as part of SPACERAD.

3.2 Environment Modeling

Existing radiation belt models are static and useful only for long-term (6 months or longer) average conditions. Also, the existing models are made up primarily of data sets that were taken in the mid-sixties. These data sets were often not well calibrated, lacked pitch angle information, and did not contain ion species information. The experiment complement on SPACERAD will be cross-calibrated, contain ion data, have excellent pitch angle and energy resolution, and will provide a simultaneous data set over all energies. The data from these experiments will extend the existing static radiation models in energy range, particle type, pitch angle, and time resolution. That data will also permit development of the first dynamic radiation belt models.

4. SUMMARY

In conclusion, the SPACERAD program as described in this section will measure radiation induced SEUs and total dose degradation in state-of-the-art micro-electronic devices, VHSIC test chips, and advanced material (GaAs) devices both in a known space environment and at particle accelerator facilities. The space flight results will characterize in-space device performance and determine the validity of ground test procedures, device models, upset/degradation prediction codes, and environmental models. The program is being coordinated by the best radiation-test experts in government and industry, most of whom are participating. The program has all the ingredients necessary to accelerate the transfer of new technology microelectronic devices into future space systems and to provide ground test guidelines for testing future devices for the space environment.

This document presents preliminary descriptions of the SPACERAD and other DOD Geosynchronous Transfer Orbit (GTO) instruments to facilitate plans for the comprehensive analysis of the data by the SPACERAD science team and other interested investigators. A summary chart of the SPACERAD experiments listed by experiment number is given in Table 1. Also listed are the agencies contributing to design and fabrication of the experiments. The additional experiments described are supported by the Air Force Wright Aeronautical Laboratories (Gallium Arsenide Solar Cell Panel) and the Office of Naval Research (Lockheed Low and Medium Energy Ion Mass Spectrometers; Lockheed Electron and Proton Spectrometers; and the University of Chicago High Energy, Heavy Nuclei Composition Experiment).

Table 1: SPACERAD Experiments

NUMBER	EXPERIMENT	AGENCY	MEASUREMENT
701-1A	MICROELECTRONICS	NRL/ATC/FST/TELENETICS	MICROELECTRONICS CHARACTERISTICS
701-1B	INTERNAL DISCHARGE MONITOR	AFWL/JPL	DEEP DIELECTRIC CHARGING DISCHARGES
701-2	DOSIMETER	AFGL/PANAMETRICS	TOTAL DOSE/NUCLEAR STARS
701-3	MOS DOSIMETER	NRL	TOTAL DOSE
701-4	HIGH ENERGY ELECTRON SPECTROMETER	AFGL/PANAMETRICS	ELECTRONS 1 TO 10 MEV
701-5A	MEDIUM ENERGY ELECTRON SPECTROMETER	AEROSPACE	ELECTRONS 30 KEV TO 2 MEV
701-5B	MEDIUM ENERGY ELECTRON/PROTON SPECTROMETER	AFGL/EMMANUEL/MULLARD	ELECTRONS 20 TO 250 KEV PROTONS 40 KEV TO 2 MEV
701-6	LOW ENERGY PLASMA ANALYZER	AEROSPACE	ELECTRONS 10 EV TO 30 KEV PROTONS 10 EV TO 30 KEV
701-7A	RELATIVISTIC PROTON DETECTOR	AEROSPACE	PROTONS >320, >440 MEV
701-7B	PROTON SWITCHES	AEROSPACE	PROTONS 20 TO 80 MEV
701-8, 9	PROTON TELESCOPE	AFGL/EMMANUEL/MIT	PROTONS 1 TO 100 MEV
701-11A	MAGNETOSPHERIC ION COMPOSITION SPECTROMETER	AEROSPACE/MAX PLANCK	IONS 30 TO 300 KEV/Q
701-11B	LOW ENERGY MAGNETOSPHERIC ION COMPOSITION SPECTROMETER	AEROSPACE/LASL	IONS 40 EV TO 40 KEV/Q
701-11C	HEAVY ION TELESCOPE	AEROSPACE/LASL	IONS 100 KEV TO 15 MEV/NUC
701-13A	FLUXGATE MAGNETOMETER	AFGL/SCHONSTEDT	DC TO 10 HZ MAG FIELD
701-13B	SEARCH COIL MAGNETOMETER	AFGL/U. OF IOWA	5.6 HZ TO 10 KHZ MAG FIELD
701-14	TERMAL PLASMA PROBE	AFGL/U. OF CAL. BERKELEY/ ANALYTIX/REGIS COLLEGE	THERMAL PLASMA TO 10 EV E-FIELD DC TO 1 KHZ
701-15	PASSIVE PLASMA SOUNDER	AFGL/U. OF IOWA	E-FIELD 5.6 HZ TO 400 KHZ

II. Orbital and Spacecraft Parameters

The CRRES mission sequence is as follows: The satellite will be Shuttle launched, deployed from the Shuttle the first day in orbit, spun up to approximately 20 rpm, and remain at the Low Earth Orbit (LEO) for approximately 60 days while chemical release experiments are conducted. After the LEO mission, the satellite will be boosted into a Geosynchronous Transfer Orbit (GTO) by a boost motor. Hydrazine motors will then raise perigee to 400 km. The satellite will remain in GTO exercising the elliptical orbit experiments, including SPACERAD, for the remainder of its lifetime. The sequence is illustrated in Figure 2. The orbit parameters for the mission are:

	LEO	GTO
Altitude:	300 ± 50 km	400 km \times $35,800$ km
Inclination:	28.5°	$< 28.5^\circ$
Duration:	45-60 days	3 years +

In GTO, the orbital period will be ~ 10.5 hours, and the rate of precession of the line of apsides, $\sim 0.6^\circ$ per day. The satellite will spin at a rate near 2 rpm, and the spin vector of the satellite will be actively controlled to point toward the Sun.

A view of CRRES as designed by Ball Aerospace, the satellite contractor, is shown in Figure 3. The satellite body is octagonal, with the center removed for holding the boost motor. The large solar arrays on top provide the spacecraft power. The main body of the satellite is approximately 3 m wide and 1 m high.

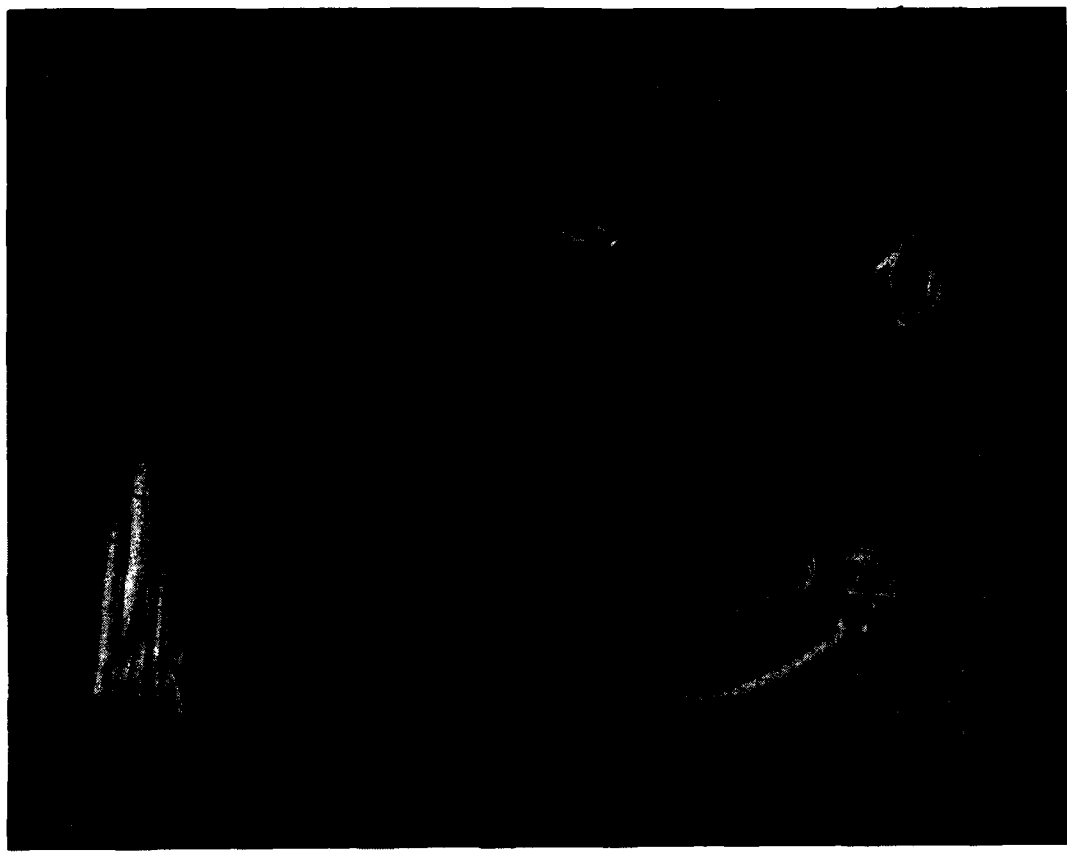


Figure 2. Sequence of the CRRES Mission

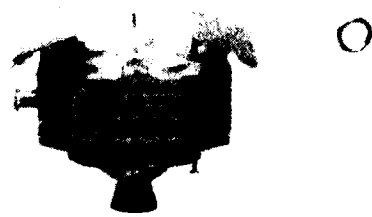


Figure 3. Model of the CRRES Satellite

Four of the eight compartments on the sides of the satellite will contain chemical canisters, and four will contain experiments and subsystems. Some of the experiments will be mounted externally, as will the experiment booms.

All SPACERAD experiments are mounted on the sides and top of the satellite, with the wire booms extending from the top of the satellite and the magnetometer boom from Compartment 2. A cut-away of CRRES perpendicular to the spin axis is shown in Figure 4. Even-numbered compartments contain scientific instruments; odd-numbered compartments contain chemical canisters. Table 2 is a list of the SPACERAD and supportive experiments with their locations (compartment number, top or bottom).

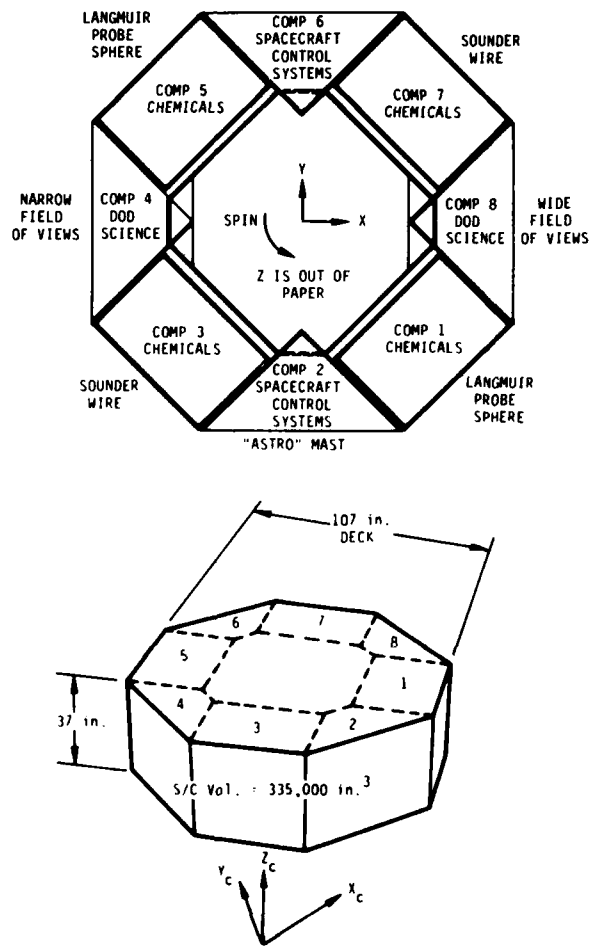


Figure 4. Cut-Away View of the CRRES Satellite With Placement of Experiments, Booms, and Chemicals

Table 2. SPACERAD Instrument Locations and Line of Sight

DESCRIPTION	COMPARTMENT/ LOCATION	LINE OF SIGHT
AFGL-701-1A MICROELECTRONICS	8	IN SPIN PLANE
AFGL-701-1B INTERNAL DISCHARGE MONITOR	8	IN SPIN PLANE
AFGL-701-2 DOSIMETER	8	IN SPIN PLANE
AFGL-701-3 MOS DOSIMETER	8	IN SPIN PLANE
AFGL-701-4 HIGH ENERGY ELECTRONS	4	IN SPIN PLANE
AFGL-701-5 MEDIUM ELECTRONS A	4	IN SPIN PLANE
AFGL-701-5 MEDIUM ELECTRONS B	4	25° BELOW SPIN PLANE
AFGL-701-6 LOW ENERGY PLASMA	8	IN SPIN PLANE
AFGL-701-7A RANGE TELESCOPE	4	IN SPIN PLANE
AFGL-701-7B PROTON SWITCH	4	IN SPIN PLANE
AFGL-701-8, -9 PROTOL	4	IN SPIN PLANE
AFGL-701-11 HIGH MASS IONS A	4	IN SPIN PLANE
AFGL-701-11 HIGH MASS IONS B	4	IN SPIN PLANE
AFGL-701-11 HIGH MASS IONS C	4	IN SPIN PLANE
AFAPL-801 SOLAR PANEL	TOP	SPIN PLANE
AFAPL-801 HEATED SOLAR PANEL	TOP	SPIN PLANE
ONR-307-3 SEP SENSOR	BOTTOM	30°, 70° FROM -Z
ONR-307-8 LEHI MASS SPEC.	BOTTOM	45° FROM -Z
ONR-307-8 LEHI MASS SPEC.	BOTTOM	75° FROM -Z
ONR-307-8 HEHI MASS SPEC.	BOTTOM	75° FROM -Z
ONR-604 ISOTOPES IN FLARES	8	IN SPIN PLANE

III. Engineering Experiments

Overview

High energy particles can degrade the performance of spacecraft in several ways. Three engineering experiments are being flown on CRRES to measure deleterious effects of the harsh near-Earth high energy particle environment. The three experiments are the Microelectronics Package (MEP), the Internal Discharge Monitor (IDM), and the Gallium Arsenide (GaAs) Solar Cell Panel Experiment. The MEP will measure single event upsets (SEUs), total dose, and dose rate effects on advanced technology microelectronic devices. The IDM will measure arc discharges caused by deep dielectric charging in semiconductor materials typically used in or on operational spacecraft. The Solar Cell Experiment will measure the performance characteristics of advanced GaAs solar cells as they degrade in the radiation environment. Spacecraft degradation in the form of SEUs, radiation dose degradation, and arc discharging are discussed below.

SEUs are changes in the logic state of memories, microprocessors, and other microelectronic devices resulting from energy deposited from a single, highly energetic particle traversing the device or initiating a nuclear reaction within it. The resulting errors can be either soft (the cause of incorrect logic execution in the system until it is properly reset or reinitialized) or hard (permanent changes that can prevent the proper function of the device and, in extreme cases, the system). At present, hard errors are less probable than soft errors, but this may change as the size of device elements decreases.

Total-dose effects in electronics parts appear as changes in the operational electrical parameters of the parts. In semiconductor devices, electron-hole pairs (excess charge carriers) are generated, and charges are trapped in the oxide layers until the accumulated trapped charge reaches a level where the device can no longer function as designed. The parameter changes are a function of the total dose received and the electrical bias condition of the device during irradiation. They are also a function of the rate and duration of the irradiation.

In addition to contributing to decreased lifetime because of total dose absorbed, high dose-rates can temporarily cause certain devices to operate out of specification or to cease functioning altogether. The upsets can last from seconds to hours depending on the type of electronics. High dose rates become more critical as a spacecraft gets older since the total dose already absorbed has reduced the amount of radiation necessary to create an anomaly. Therefore, in predicting frequency and periods of satellite upsets, dose rate is a critical parameter.

High energy particles (above \sim 200 keV) can deposit charge in satellite dielectrics and build up electric fields large enough to cause breakdowns and discharges. Energy from discharges in cable dielectrics and printed circuit boards can couple directly into electronic components, and, in an extreme case, can cause burn-out. Although other missions, such as SCATHA, have looked at surface charging effects, no experimental results exist for deep dielectric charging, in a simultaneously measured radiation belt environment. Testing many different dielectric materials will help determine which ones are less sensitive to discharging in space. Interpretation of the engineering experiments depends on the simultaneous measurement of particle and field parameters.

Contents

1. Scientific Objectives	15
2. Application	17
3. Measuring Techniques	19
4. Function Block Diagram	23
Acknowledgments	23
References	25

**1. The SPACERAD Microelectronics
Experiment (AFGL-701-1A)**

by

James C. Ritter, Arthur B. Campbell, Robert Wettingfeld
Naval Research Laboratory
Washington, DC 20375

William B. Huber
Air Force Geophysics Laboratory
Hanscom AFB, MA 01731

Warren C. Tolman
Assurance Technology Corporation
Carlisle, MA 01741

and

Richard Gonyea
Telenetics Corporation
Pikesville, MD 21208

I. SCIENTIFIC OBJECTIVES

The purpose of the SPACERAD Microelectronics Experiment is to study radiation induced single event upsets (SEUs) and total dose damage in advanced micro-electronic devices in the measured space environment and at particle accelerators. The space experiment will monitor the operations of state-of-the-art silicon de-

vices, VHSIC (Very High Speed Integrated Circuit) devices, and advanced material devices such as gallium arsenide (GaAs) random access memories (RAMs). The devices have been selected because of their present and proposed use in DOD and NASA space programs and their scientific interest, such as comparison of feature sizes, technologies, or materials, etc. The space experiment is complemented by ground test and device modeling programs to provide a direct comparison of their data with space measurements. Ground testing of devices from the same lot and wafer (when available) will be used in conjunction with present radiation belt and device models to predict, prior to flight, the expected SEUs in space.

The satellite contains a complete set of particle instruments to measure simultaneously the cosmic rays, high energy protons, and high energy electrons in the space environment. Thus, the SEUs and the total-dose damage will be directly related to the particle environments producing them. Space results will check model predictions and determine the validity of ground test procedures and existing device models.

The primary scientific objectives of the experiment are:

- (1) To determine SEU rates in an elliptical orbit as a function of orbital position, particle type, device feature size, technology, material, total dose, and operating conditions;
- (2) To compare measured SEU rates in space to predicted rates based on device modeling, to correlate SEU rates in measured space particle environments to measured rates in simulated environments in the laboratory;
- (3) To compare total-dose effects observed in measured space environments with preflight laboratory tests, with postflight simulations, and with model predictions;
- (4) To measure SEU and total-dose effects in space radiation environments for state-of-the-art VHSICs, GaAs RAMs, and microprocessors that are used in or proposed for DOD and NASA space programs; and
- (5) To develop testing and modeling procedures and feature-size scaling factors that can be used with the SPACERAD dynamic radiation belt models to predict SEU rates, and device degradation and annealing factors for future devices not tested in the SPACERAD program.

This is the first comprehensive, systematic SEU experiment ever to be performed on a satellite. Inadvertent "experiments" have occurred on a variety of operational spacecraft. However, during those events, the particle environments were not simultaneously measured. Some total dose measurements have previously been made in space, but never with such an extensive complement of state-of-the-art devices nor with simultaneous particle measurements. This space measurement program is the only one to be backed up with extensive ground tests

on devices from the same lot and wafer and with detailed device modeling and analysis.

2. APPLICATION

The basic suggestion that SEUs might be due to cosmic rays was made by Wallmark and Marcus.¹ The first observation and corresponding explanation was made by Binder et al.² Both of these papers were initially generally ignored. The field became active in 1978 with the discovery of alpha particle induced upsets by May and Woods,³ and further discussion of cosmic ray induced upsets by Pickel and Blandford.⁴ In 1979, Guenzer et al⁵ showed that SEUs could be produced indirectly by particles from nuclear reactions induced by energetic neutrons and protons, and Wyatt et al⁶ reported upsets produced by energetic protons. These two papers spurred DNA and DARPA to establish the first comprehensive research program on single-event radiation effects in microcircuits. Also in 1979, Kolasinski et al⁷ reported the first single heavy ion induced latchup, and Sivo et al⁸ performed model calculations to interpret this result. A basic approach to cosmic ray upset rates was presented by Pickel and Blandford,⁹ resulting in what they called the CRIER (Cosmic Ray Induced Error Rate Analysis) code.

-
1. Wallmark, J.T., and Marcus, S.M. (1962) Minimum size and maximum packing density of nonredundant semiconductor devices, Proc. IRE 286.
 2. Binder, D., Smith, E.C., and Holman, A.B. (1975) Satellite anomalies from galactic cosmic rays, IEEE Trans. Nucl. Sci. (NS-22) 7:2675.
 3. May, Timothy C., and Woods, Murray H. (1979) Alpha-particle-induced soft errors in dynamic memories, IEEE Trans. Electron Devices (ED-26) 1:2.
 4. Pickel, J.C., and Blandford, J.T., Jr. (1978) Cosmic ray induced errors in MOS memory cells, IEEE Trans. Nucl. Sci. (NS-25) 6:1166.
 5. Guenzer, C.S., Wolicki, E.A., and Allas, R.G. (1979) Single event upset of dynamic RAMs by neutrons and protons, IEEE Trans. Nucl. Sci. (NS-26) 6:5048.
 6. Wyatt, R.C., McNulty, P.J., Toumbas, P., Rothwell, P.L., and Filz, R.C. (1979) Soft errors induced by energetic protons, IEEE Trans. Nucl. Sci. (NS-26) 6:4905.
 7. Kolasinski, W.A., Blake, J.B., Anthony, J.K., Price, W.E., and Smith, E.C. (1979) Simulation of cosmic-ray induced soft errors and latchup in integrated circuit computer memories, IEEE Trans. Nucl. Sci. (NS-26) 6:5087.
 8. Sivo, L.L., Peden, J.C., Brettschneider, M., Price, W., and Pentecost, P. (1979) Cosmic ray-induced soft errors in static MOS memory cells, IEEE Trans. Nucl. Sci. (NS-26) 6:5042.
 9. Pickel, James C., and Blandford, James T., Jr. (1980) Cosmic-ray-induced errors in MOS devices, IEEE Trans. Nucl. Sci. (NS-27) 2:1006.

In 1981, attention was focused on the single-event effects produced by protons from the Earth's radiation belts.¹⁰ In the same year, the idea for the SPACERAD SEU experiment was also conceived and developed.

The SEU area has become so important that the IEEE Conference on Nuclear and Space Radiation Effects now devotes an entire session to it. The December 1983 issue of IEEE Transactions on Nuclear Science contains the proceedings of this conference and is the best source of up-to-date information about SEUs.

At the present time, the SEU sensitivity of many devices, including the latest state-of-the-art devices, has been studied in the laboratory, using ion accelerators. However, we still do not know the relationship between these measurements and what will happen in a space environment. Simple models have been developed,^{11, 12, 13} but, as yet, none has been verified with a space experiment.

Much work has progressed on modeling total dose damage from Co60 irradiations, and a limited number of advanced technology devices have been successfully hardened to megarad levels. There is, however, current controversy over the effect of different types of radiation on device performance.^{14, 15} This work is important for spacecraft devices since total dose exposure in space is caused by energetic particles and not by gamma rays. It has also been shown¹⁶ that dose rate is significant for determining the type and level of effects observed in devices. The IEEE Transactions on Nuclear Science is also an excellent reference for up-to-date information on device total dose and dose rate effects.

Overall, both of these areas continue to develop rapidly with ground-based analysis, but definitive measurements in space environments are still needed.

-
10. Petersen, Edward (1981) Soft errors due to protons in the radiation belt, IEEE Trans. Nucl. Sci. (NS-28) 6:3981.
 11. Petersen, E.L., Shapiro, P., Adams, J.H., Jr., and Burke, E.A. (1982) Calculation of cosmic-ray induced soft upsets and scaling in VLSI devices, IEEE Trans. Nucl. Sci. (NS-29) 6:2055.
 12. Petersen, E.L., Langworthy, J.B., and Diehl, S.E. (1983) Suggested single event figure of merit, IEEE Trans. Nucl. Sci. (NS-30) 6:4533.
 13. Bendel, W.L., and Petersen, E.L. (1983) Proton upsets in orbit, IEEE Trans. Nucl. Sci. (NS-30) 6:4481.
 14. Brucker, G.J., Stassinopoulos, E.G., Van Gunten, O., August, L.S., and Jordan, T.M. (1982) The damage equivalence of electrons, protons, and gamma rays in MOS devices, IEEE Trans. Nucl. Sci. (NS-29) 6:1966.
 15. Stassinopoulos, E.G., Van Gunten, O., Brucker, G.J., Knudson, A.R., and Jordan, T.M. (1983) The damage equivalence of electrons, protons, alpha and gamma rays in rad-hard MOS devices, IEEE Trans. Nucl. Sci. (NS-30) 6:4363.
 16. Stassinopoulos, E.G., Brucker, G.J., and Van Gunten, O. (1984) Total dose and dose-rate dependence of proton damage in MOS devices during and after irradiation, IEEE Trans. Nucl. Sci. (NS-31) 6:1444.

Radiation belt models are used to predict the extent of hazards high energy particle populations present to electronic devices on spacecraft. Existing static radiation belt models will be used to predict the total dose damage to specific devices during the lifetime of the SPACERAD microelectronics experiment. A calculation of the particle environments specific to the SPACERAD orbit was made for the microelectronics experiment based on the latest NASA National Space Science Data Center Model of the Earth's radiation belts.¹⁷ The space flight results will be compared with predicted preflight results obtained using the NASA model.

For predicting electronic degradation and failure and SEUs in future space systems, the SPACERAD experiment should provide an updated model not only of the principal components of the belts (that is, electrons and protons), but also of minor constituents of the belts and of cosmic ray LET (linear energy transfer or stopping power) spectra as a function of orbital position and local time.

3. MEASURING TECHNIQUES

The microelectronics package (MEP), the flight package of the microelectronics experiment program, has two broad measurement areas: (1) SEUs in selected memory, microprocessor, and VHSIC devices, and (2) parameter shifts caused by accumulated total radiation dose in the memory, microprocessor, and VHSIC devices, as well as in inverters, operational amplifiers, comparators, A/D converters, and discrete transistors.

Semiconductor dosimeters are distributed throughout the MEP to measure the radiation exposure accumulated in flight on the circuit boards where the microelectronics test devices are mounted. Temperature sensors will also be mounted on the test circuit boards to help differentiate between radiation effects and normal parameter shifts induced by temperature changes. Silicon and GaAs thin barrier radiation detectors with associated linear amplifiers and pulse height analyzers will also be in the MEP to measure the energy spectrum of the radiation environment as seen by the devices under test.

Approximately 65 device types and over 450 devices will be space tested. The memory devices include GaAs RAMs, CMOS and MNOS PROMS, and CMOS and CMOS/SOS gate arrays. The microprocessor test candidates include both CMOS and bipolar types. The inverters are CMOS. The op amps and comparators are bipolar. The A/D converters are both CMOS and bipolar. The discrete transistors and semiconductor dosimeters are CMOS.

17. Stassinopoulos, E.G., and Barth, J.M. (1982) Predicted Charged Particle Environment for the Chemical Release and Radiation Effects Satellite. NASA Rpt. X-601-83-1.

The flight package is configured as shown in Figure 5. It consists of three basic units, a front experiment unit 45 by 15 by 2.5 inches, a second experiment unit 25 by 15 by 2 inches, and a power/control unit 13 by 15 by 7.5 inches. The experimental units will be made up of 5- by 5-inch "eggcrate" cells configured with three boards as shown in Figure 6. The devices under test (DUTs) will be placed according to their radiation hardness level and desired exposure level. The cells in the outermost compartment are numbered 1 through 27 as shown in Figure 7. The numbers are used to identify parts placement location. The package weighs approximately 96 pounds and will dissipate between 50 and 75 watts average power. The 45- by 15-inch face of the package is exposed to the environment through an opening in the spacecraft skin. The cover on this face will be approximately 15-mil aluminum to permit high dose rates to the devices. All microelectronics circuit boards are mounted parallel to this face. The radiation

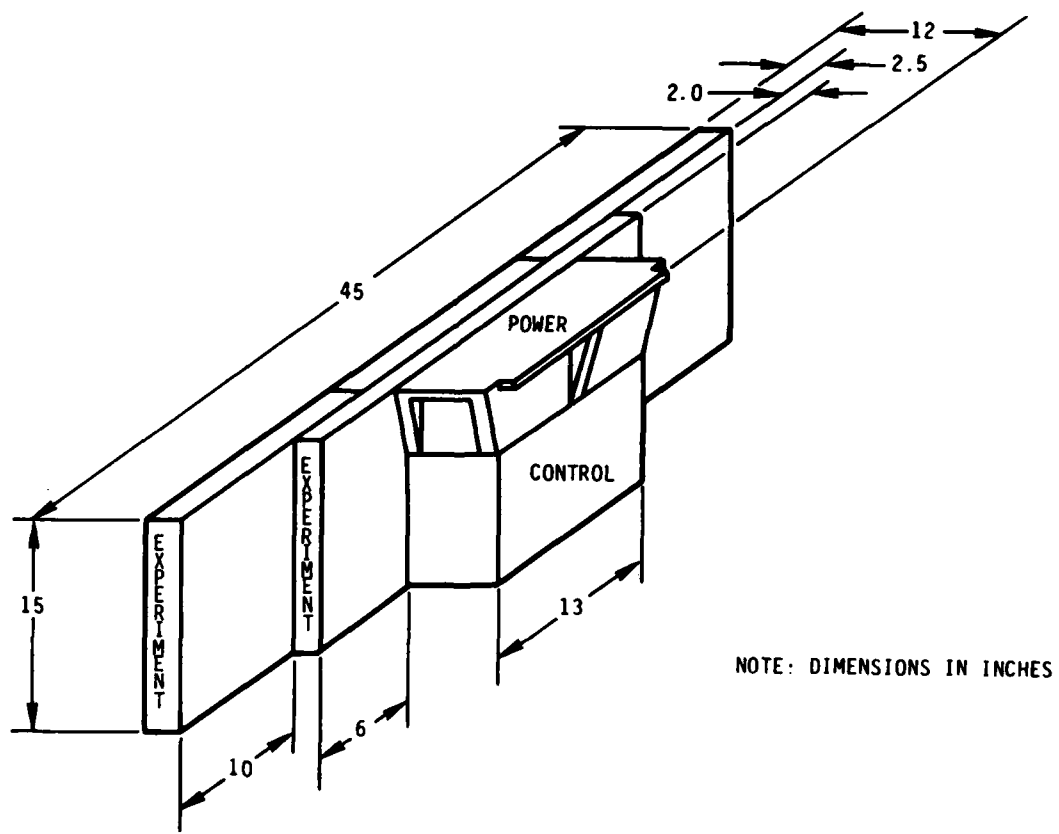


Figure 5. Configuration of the Assembled Microelectronics Flight Package

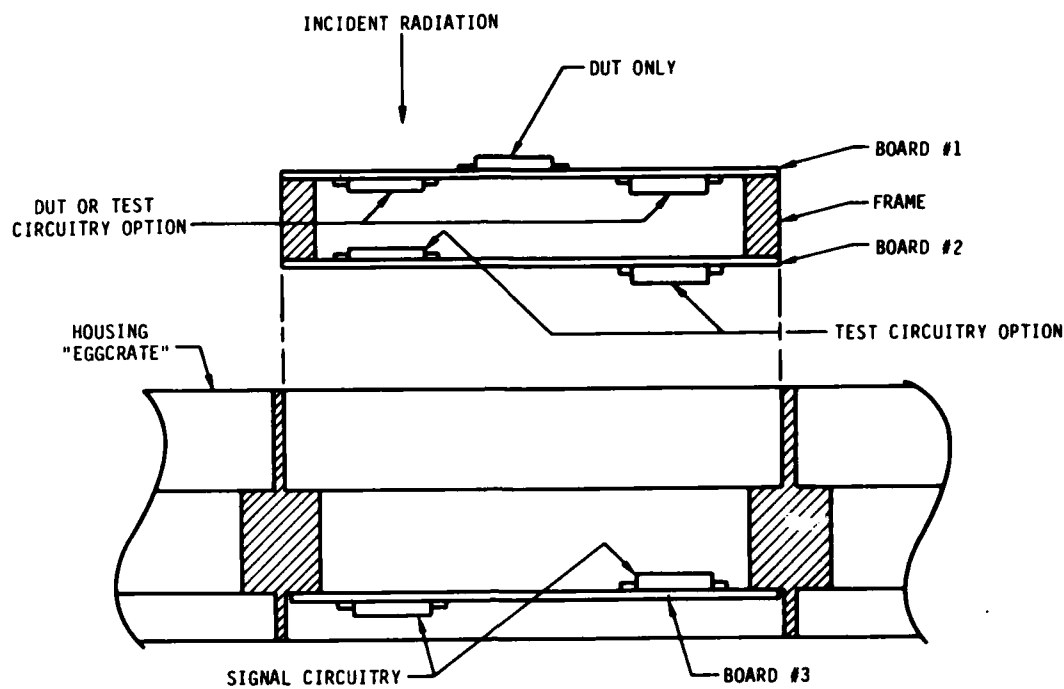


Figure 6. Single-Cell Configuration in the Microelectronics Package

1	2	3	4	5	6	7	8	9
10	11	12	13	14	15	16	17	18
19	20	21	22	23	24	25	26	27

Figure 7. Eggcrate-Cell Configuration and Numbering Scheme for Microelectronics Package

hard parts for total dose measurement are located on the first board. Softer parts are awarded space on succeeding boards. The SEU measurement parts that are susceptible to the highest energetic penetrating particles are assigned to the boards deepest in the experimental compartments.

Control electronics, power conditioners, experiment memory, measurement support circuits, command decoder, and telemetry formatting circuits are at the back of the package to minimize radiation exposure.

The experiment controller is a Sandia SA3000 microprocessor, a radhard, CMOS, 10-V version of the Intel 8085. It is supported by I/O ports, 3- to 8-line decoders, level shifters, and bus transceivers in radhard versions from Sandia.

The software for the controller synchronizes the processing of SEU, total dose, pulse height analyzer (PHA), and dosimeter data. The SEU data is processed with 1- to 4-second resolution. The software performs all total dose measurements once per orbit and dumps the PHA data once per orbit. The controller is also used to format the telemetry data for delivery to the spacecraft tape recorder and to receive ground commands via the spacecraft command decoder for changing the MEP flight program. The telemetry data rate is 312 bits per second (bps) in a 16-Kbps data stream. The telemetry data is formatted by type; that is, SEU, total dose, PHA, and housekeeping (HK) data have different formats.

The DUTs are powered in blocks. Each block contains the same or similar devices. All device types are divided into redundant half-test blocks. Thus, if one block of devices is automatically shut down because of excessive power dissipation, the redundant half can be powered up for continued tests. All DUT blocks contain power current monitors that automatically shut down power to the block if an excess power drain occurs. These blocks may be powered up by ground command to allow for fault clearing.

The initial device test program is established in a ROM and copied into RAM at experiment initialization. As devices are lost because of radiation degradation during the experiment lifetime, the RAM program is modified automatically and by ground command. In case of power shutdown, the experiment can be reinitialized and totally reprogrammed by ground commands. These are established by the latest ground data analysis of previous flight data.

For memory-type devices, the SEU tests consist of writing regular patterns to the test RAMs, reading these patterns and other fixed patterns from ROMs and arrays, and then checking the read patterns for errors. All errors are reported to TLM with their address location. Permanent errors (hard errors) are masked and reported only once and are identified as hard errors. The test microprocessors perform repeatable processing cycles with the answers checked against the correct results. Wrong answers are flagged and reported. The SEU tests can handle up to five upsets per second in the normal data mode. For solar flares,

when upsets in the experiment may exceed this rate, an alternate compressed data mode (histogram mode) is set, and upset count only is reported. When the upset rate returns to normal, the SEU tests again report device and address location for each upset.

Total dose measurements include device input threshold voltage measurements, output current sourcing and sinking measurements, and output current voltage (I-V) curves. The dosimeters are p-channel CMOS inverters of the CD4007 type. Input threshold voltage shift is the measure of total dose received. There are 64 dosimeters located throughout the package; 32 are sensitive dosimeters, and 32 are less sensitive as determined by the bias voltage applied during exposure.

4. FUNCTION BLOCK DIAGRAM

The function block diagram shown in Figure 8 is a diagram simplified to demonstrate the redundancy used throughout the experiment design. Five basic functions are shown: power supplies, Control Unit (CU) for spacecraft signal interfacing and memory control, Shared Memory, the Instrument Control Unit (ICU) for controlling power and measurements for the redundant experiment blocks, and the Bus Structure (Control and Instrument). Four out of five functions have totally redundant circuits. In the memory, shadowing is used for redundancy; that is, all memory presently used for measurement or data routing is written in two places. If an error is detected by parity checks or a checksum, the operation is aborted and the second memory location is used.

Acknowledgments

The CRRES Microelectronics Working Group has assisted in the development of the entire Microelectronics Experiment and has been responsible for recommending most of the devices on the device list.

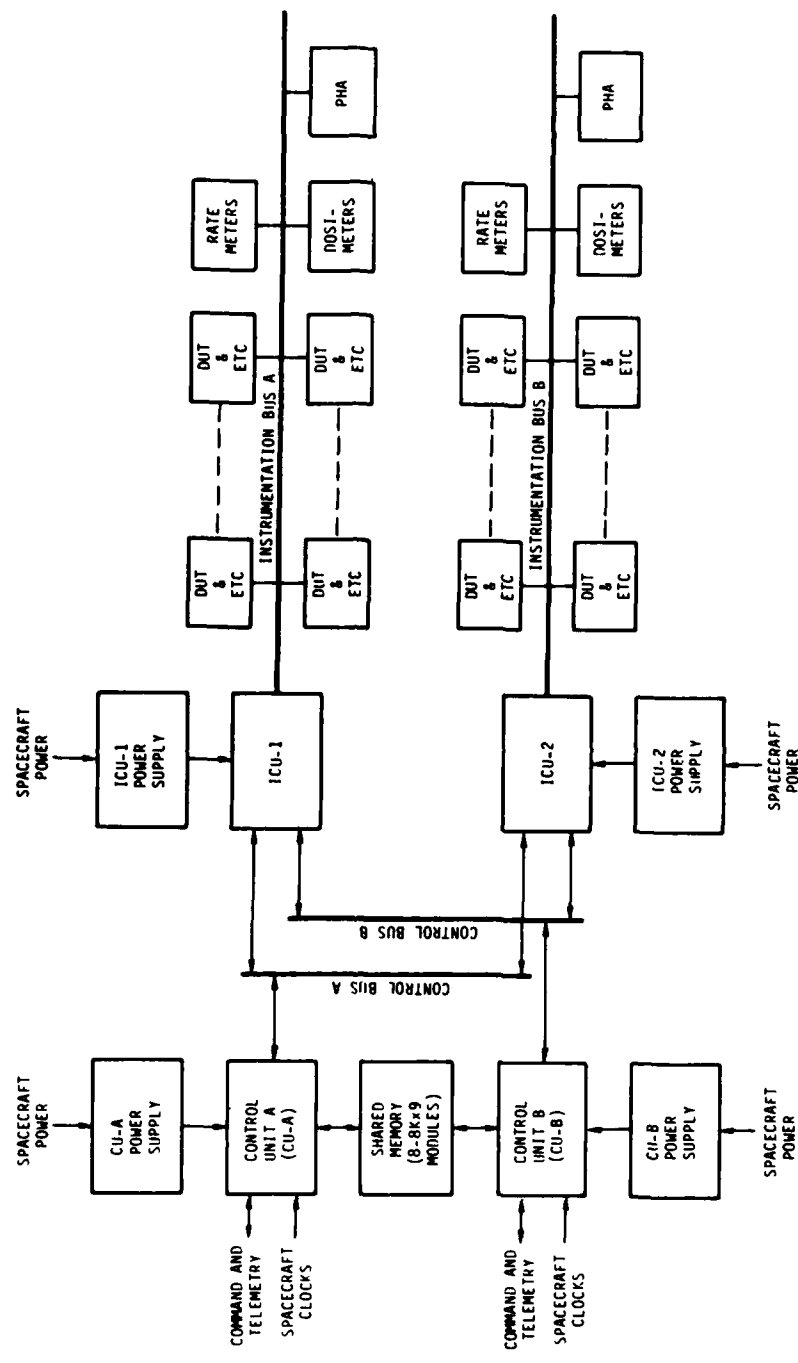


Figure 8. Function Block Diagram for Microelectronics Package

References

1. Wallmark, J. T., and Marcus, S. M. (1962) Minimum size and maximum packing density of nonredundant semiconductor devices, Proc. IRE 50:286.
2. Binder, D., Smith, E.C., and Holman, A.B. (1975) Satellite anomalies from galactic cosmic rays, IEEE Trans. Nucl. Sci. (NS-22) 7:2675.
3. May, Timothy C., and Woods, Murray H. (1979) Alpha-particle-induced soft errors in dynamic memories, IEEE Trans. Electron Devices (ED-26) 1:2.
4. Pickel, J. C., and Blandford, J. T., Jr. (1978) Cosmic ray induced errors in MOS memory cells, IEEE Trans. Nucl. Sci. (NS-25) 6:1166.
5. Guenzer, C.S., Wolicki, E.A., and Allas, R.G. (1979) Single event upset of dynamic RAMs by neutrons and protons, IEEE Trans. Nucl. Sci. (NS-26) 6:5048.
6. Wyatt, R.C., McNulty, P.J., Toumbas, P., Rothwell, P. L., and Filz, R. C. (1979) Soft errors induced by energetic protons, IEEE Trans. Nucl. Sci. (NS-26) 6:4905.
7. Kolasinski, W.A., Blake, J.B., Anthony, J.K., Price, W.E., and Smith, E.C. (1979) Simulation of cosmic-ray induced soft errors and latchup in integrated circuit computer memories, IEEE Trans. Nucl. Sci. (NS-26) 6:5087.
8. Sivo, L.L., Peden, J.C., Brettschneider, M., Price, W., and Pentecost, P. (1979) Cosmic ray-induced soft errors in static MOS memory cells, IEEE Trans. Nucl. Sci. (NS-26) 6:5042.
9. Pickel, James C., and Blandford, James T., Jr. (1980) Cosmic-ray-induced errors in MOS devices, IEEE Trans. Nucl. Sci. (NS-27) 2:1006.
10. Petersen, Edward (1981) Soft errors due to protons in the radiation belt, IEEE Trans. Nucl. Sci. (NS-28) 6:3981.

11. Petersen, E. L., Shapiro, P., Adams, J. H., Jr., and Burke, E. A. (1982) Calculation of cosmic-ray induced soft upsets and scaling in VLSI devices, IEEE Trans. Nucl. Sci. (NS-29) 6:2055.
12. Petersen, E. L., Langworthy, J. B., and Diehl, S. E. (1983) Suggested single event figure of merit, IEEE Trans. Nucl. Sci. (NS-30) 6:4533.
13. Bendel, W. L., and Petersen, E. L. (1983) Proton upsets in orbit, IEEE Trans. Nucl. Sci. (NS-30) 6:4481.
14. Brucker, G. J., Stassinopoulos, E. G., Van Gunten, O., August, L. S., and Jordan, T. M. (1982) The damage equivalence of electrons, protons, and gamma rays in MOS devices, IEEE Trans. Nucl. Sci. (NS-29) 6:1966.
15. Stassinopoulos, E. G., Van Gunten, O., Brucker, G. J., Knudson, A. R., and Jordan, T. M. (1983) The damage equivalence of electrons, protons, alpha and gamma rays in rad-hard MOS devices, IEEE Trans. Nucl. Sci. (NS-30) 6:4363.
16. Stassinopoulos, E. G., Brucker, G. J., and Van Gunten, O. (1984) Total-dose and dose-rate dependence of proton damage in MOS devices during and after irradiation, IEEE Trans. Nucl. Sci. (NS-31) 6:1444.
17. Stassinopoulos, E. G., and Barth, J. M. (1982) Predicted Charged Particle Environment for the Chemical Release and Radiation Effects Satellite, NASA Rpt. X-601-83-1.

Contents

1. Scientific Objectives	27
2. Applications	29
3. Measuring Techniques	29
4. Function Block Diagram	31
Acknowledgments	34

2. The Internal Discharge Monitor (AFGL-701-B)

by

P. Robinson and J.M. Conley
Jet Propulsion Laboratory
Pasadena, CA 91109

1. SCIENTIFIC OBJECTIVES

The objective of the Internal Discharge Monitor (IDM) experiment is to characterize internal electrostatic discharge events that may damage or upset (disturb) electronic circuits in spacecraft subjected to high energy charged-particle radiation environments. Discharges caused by high energy electron charge buildup have been tentatively identified as the cause of anomalies on the Voyager and other spacecraft operating in intense electron radiation fields. These discharges are apparently the result of penetrating electrons that are stopped in electronic dielectric materials inside the spacecraft. After sufficient charge has accumulated within the dielectric, a discharge may occur to nearby electronics or cabling, resulting in upset or damage to sensitive components. The IDM experiment is part of the Air Force Weapons Laboratory (AFWL) on-going electron-caused electromagnetic pulse (ECEMP) effort. The IDM experiment is designed to determine whether or not internal discharge phenomena indeed occur under the CRRES orbital conditions, and, if so, to measure the characteristics of the discharge.

The IDM instrument will test 16 dielectric samples. The dielectric materials and geometric configurations were selected after ground tests in which samples

were irradiated with 1 to 3 MeV electrons in the JPL dynamitron. The experiment data will be correlated with the orbital environment to determine the quantitative dependence of the discharge phenomena on ionizing radiation flux and spectrum, and on material properties.

To obtain the experiment goal, five specific instrument design objectives have been identified:

(1) To detect and record discharge data for comparison with laboratory tests. The goal is to measure the smallest legitimate pulses, which are on the order of 10 mV and 1 nsec. The data will also include as much information as possible about the wave shape of the discharge.

(2) To detect discharges that could destroy or disrupt electronics. The upset level of advanced electronic parts is a function of the part type, technology, etc. Figure 9 shows the best current understanding of part sensitivity. This figure shows peak voltage versus pulse width. If the peak voltage is above a certain value, and if the pulse is long enough, damage or disruption will occur. If the pulse is not long enough, a certain minimum energy (in addition to a minimum voltage) is required. (In some cases, a minimum charge may be required.) This translates into the two solid curves shown in the figure.

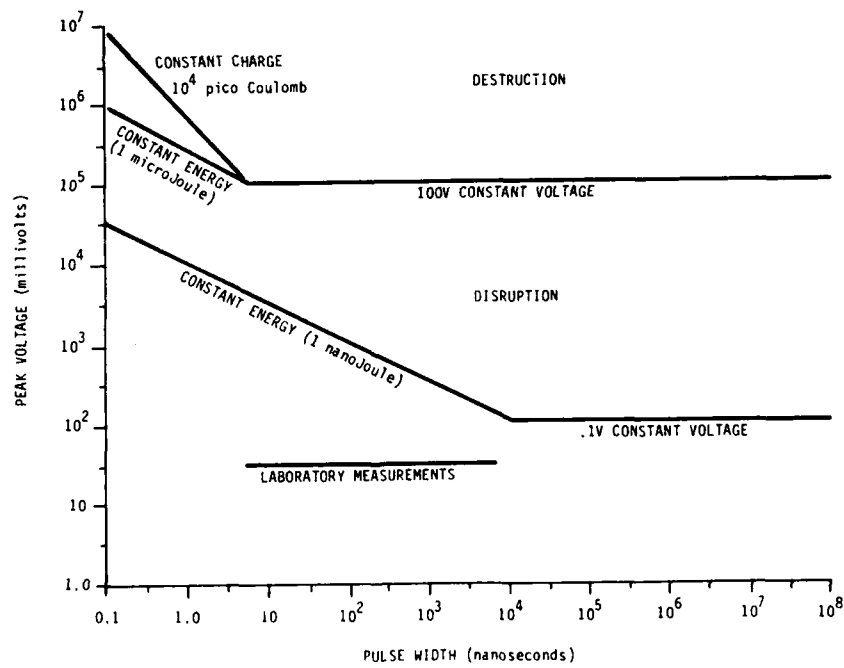


Figure 9. Peak Voltage Detector Characteristics as a Function of Pulse Width

(3) To eliminate detection of pulses or other phenomena that are not significant to actual spacecraft operations. This implies a lower limit to detector sensitivity somewhere below, but not significantly below, the disruption curve shown in Figure 9.

(4) To protect the detector against large pulses. For signals greater than 10 V, detailed wave shape information for the pulses will be sacrificed.

(5) To meet reliability, cost, power, and weight requirements.

These objectives constrain the circuit design of the IDM.

2. APPLICATIONS

A successful IDM experiment will accomplish the following scientific and engineering objectives:

- (1) To verify the existence of ECEMP events in the CRRES orbit;
- (2) To verify the ground testing techniques for determining material ECEMP properties; and
- (3) To provide a data base for comparison with theoretical calculations of the ECEMP rates and magnitudes.

At the conclusion of the IDM experiment, the radiation effects community will have a good engineering understanding of discharges caused by penetrating radiation in the Earth's radiation belts, and possibly a good basis for extrapolation to other environments.

As part of this understanding, a good data base for the environment to which CRRES has been exposed is essential. We expect the complement of scientific instruments on CRRES measuring electron and ion spectra and dose to provide this data base for correlation with the IDM results.

3. MEASURING TECHNIQUES

3.1 Sample Materials and Layout

We selected dielectric samples from six basic configurations, three planar types and three cylindrical types. Schematics of the sample geometrics, numbered 1 to 6, are shown in Figure 10. Based upon tests with electron beams, six sample materials were selected in four of the basic configurations. The 16 flight samples are listed in Table 3, 12 planar and 4 cylindrical (that is, coaxial cable). For these samples, 16 RF-shielded compartments are provided, 12 for square planar samples and 4 longer compartments for samples of cable or wire.

The signal electrode of each sample is wired through the front face of the

instrument chassis to the input of the electronic circuit and terminated in a 50-ohm resistor as indicated schematically in Figure 10. The electronics characterizes the fast transient voltage signal that appears at the 50-ohm load when a discharge takes place. Specifically, a measurement of the peak voltage (and thus current) is the primary measurement of interest. Since the signal is essentially a noise pulse, it should be characterized in as much detail as possible so that false events, such as those caused by electromagnetic interference (EMI), are not mistaken for ECEMPs.

3.2 Ground Test Inputs

A wide variety of waveforms has been reported in ECEMP discharges observed in ground testing with the dynamitron electron beam. Several samples of the waveform recorded in the dynamitron sample selection tests show that the

SAMPLE TEST CONFIGURATIONS

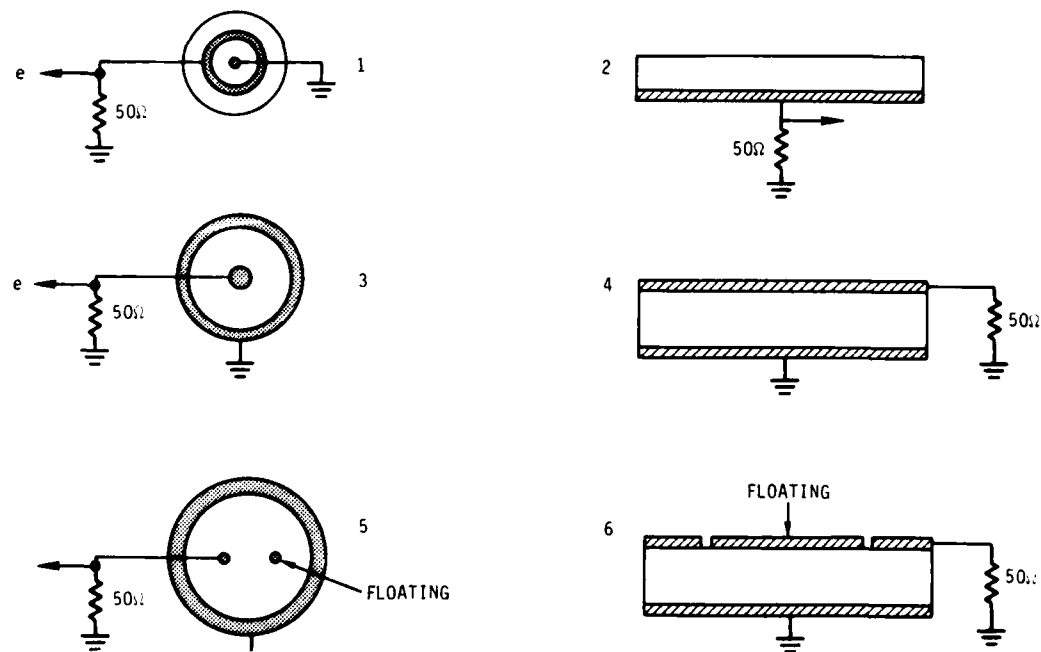


Figure 10. Dielectric Sample Test Configuration for the Internal Discharge Monitor

range of duration of these signals is 50 to 100 nsec. These signals are the baseline for determining the performance requirements of the instrument.

3.3 Electrical Property Measurement

Resistivity and capacitance will be measured and recorded at the signal contact with respect to the signal ground contact with the sample installed in the fully assembled sample container and with the cover in place, but without the parallel resistance of the feed-through insulator.

4. FUNCTION BLOCK DIAGRAM

The function block diagram for the system is given in Figure 11. The sample

Table 3. Internal Discharge Monitor Sample Materials, Thicknesses, and Configuration

Sample No.		Dielectric Thickness	Configuration
1, 16	Cu clad FR4 Fiberglass	0.125	2
2	Cu clad FR4 Fiberglass	0.125	6
3	Cu clad FR4 Fiberglass	0.125	4
4	Cu clad FEP	0.090	6
5	Cu clad FEP	0.090	4
6	Alumina	0.040	6
7	Cu clad FEP	0.090	2
8	Cu clad FR4 Fiberglass	0.047	2
9	RG316 cable	-	3
10	Aljac cable	-	3
11	SIB cable	-	1
12	PTFE	93	4
13	Cu clad PTFE reinforced fiberglass	93	2
14	TS Triax	-	5
15	Cu clad FR4 Fiberglass	30	6

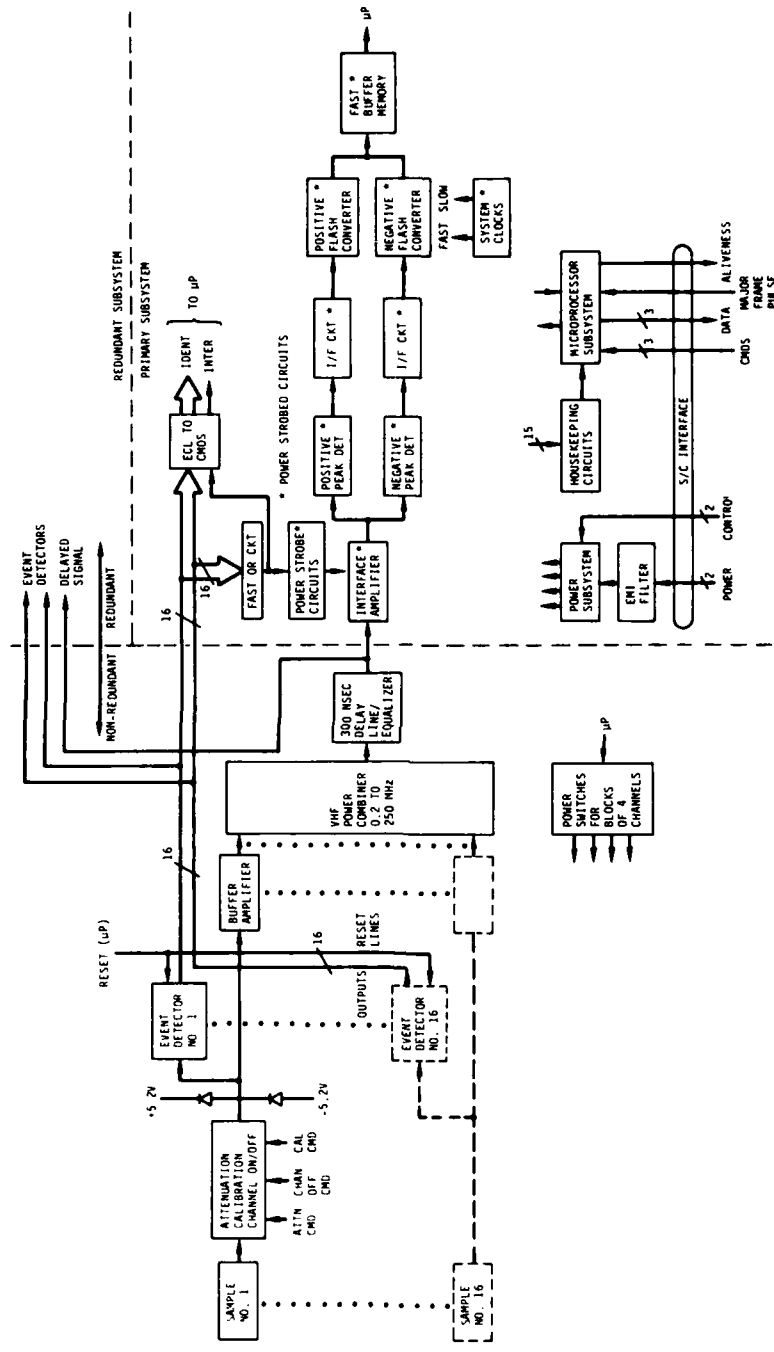


Figure 11. Function Block Diagram for the Internal Discharge Monitor

outputs will be loaded with the equivalence of a 50-ohm resistor designed to attenuate the maximum signal required to be measured for that sample to ± 5 V. This will be followed by limiting diodes tied to the +5.2 and -5.2 V supplies. The 16 event detectors will interrupt the microprocessor, identify to the microprocessor the sample that has arced, and initiate the power strobe circuitry to activate the signal processing circuits downstream of the delay line.

The buffer amplifier achieves event-detector isolation at the following specification levels:

Sensitivity:	5 mV for a 2-nsec rise time positive- or negative-going signal
Isolation, channel-to-channel:	≥ 60 dB
Delay:	≥ 300 nsec

The Calibrate/Inhibit circuit provides an artificial stimulus to the electronics input to verify proper operation of the instrument. These functions can be commanded through both the GSE and the command uplink.

The high power requirements of circuits operating at the speeds necessary to characterize the discharge pulses prohibit separate peak detectors for each sample; thus, the power combiner sums the inputs of the 16 samples. The short duration and infrequent occurrences of the upsets should assure that the samples do not interfere with one another. If the upsets are frequent enough to create interference between samples, the multiple outputs of the event counters will serve as veto signals for discounting multiple events. The signal statistics are summarized in Table 4.

Table 4. Internal Discharge Monitor Event Statistics

EVENT RATE:	1 PER DAY (1.16×10^{-5} /SEC)
DURATION:	10^{-6} SEC
NO. OF CHANNELS:	16
PROBABILITY OF SIMULTANEOUS EVENTS (UNCORRELATED):	1.8×10^{-10} PER DAY

The Delay Line/Equalizer allows the signal processing circuits to be powered and stabilized before processing the signal.

The peak detectors measure the maximum positive- and negative-going excursions of the transient signal relative to the local ground. The measurement

period of the peak detector is 10 nsec, the same as the cycle time of the flash A/D converter that digitizes the signal from the peak detector.

The buffer memory is a 12-bit-wide ECL assembly that allows the two flash converters to be read-in in parallel (simultaneously). The read time for this memory determines the system dead time.

The power strobe circuits are required to deliver power to the strobed circuits when a pulse is detected by an event detector.

The power subsystem conditions the raw spacecraft power for other subsystems.

The instrument incorporates internal in-flight calibration circuits (stimulators) capable of verifying both overall functionality of the electromechanical system and the quantitative response to signals in terms of amplitude and time. This internal calibration circuitry operates at regular intervals as a default mode when the instrument is powered, but is capable of being reprogrammed by command to vary the calibration interval, operate upon command, or cease operation entirely.

Acknowledgments

This experiment would not be possible without the help of a large number of active researchers. Among them are: Dr. M. Treadway of Jaycor; Dr. B. Beers of Beers Associates; Dr. P. Coakley of Jaycor; Capt. D. Hanifen formerly of AFWL; Lt. J. Harris of AFWL; Dr. J. Wilkenfeld of IRT; Dr. G. Inouye of TRW; Mr. R. Fredrickson of RADC; and Mr. G. Mullen of AFGL. The AFWL's encouragement and support of research in this direction is gratefully acknowledged.

Contents

1. Scientific Objectives	35
2. Application	36
3. Measuring Techniques	37
References	39

3. The Gallium Arsenide Solar Cell Panel Experiment (AFAPL-801)

by

Terry M. Trumble
Air Force Wright Aeronautical Laboratories
Wright Patterson AFB, OH 45433

I. SCIENTIFIC OBJECTIVES

The five major objectives of the Gallium Arsenide (GaAs) Solar Cell Panel experiment are:

- (1) To measure in the space environment the performance characteristics of differently configured advanced solar cell strings while measuring the radiation species (protons, electrons, ions), their flux levels, and their energy distributions;
- (2) To quantify radiation damage of GaAs and advanced silicon (Si) solar cells;
- (3) To select the optimum method (continuous heating, forward current bias heating, or intermittent heating) for annealing radiation damaged cells;
- (4) To determine optimum panel annealing parameters and operating characteristics;
- (5) To determine the optimum configuration for solar cell panels operating in a high radiation environment.

2. APPLICATIONS

Several different government and commercial organizations are conducting or sponsoring laboratory research on radiation damage to solar cells in space.^{1, 2} AFAPL-801 is confining its efforts primarily to GaAs with some evaluation of advanced Si solar cells. The following radiation measurements will be used for solar cell damage assessment:

RADIATION	ENERGY	FLUENCE
Electron	0.7 MEV	$1 \times 10^{15} e/cm^2$
	1.0 MEV	$1 \times 10^{13} - 1 \times 10^{16} e/cm^2$
	1.9 MEV	$1 \times 10^{15} e/cm^2$
Proton	0.05 MEV	
	0.1 MEV	$1 \times 10^{10} - 1 \times 10^{13} P/cm^2$
	0.2 MEV	
	0.3 MEV	$1 \times 10^{10} - 1 \times 10^{13} P/cm^2$
	0.5 MEV	
	1.0 MEV	
	10.0 MEV	
15 to 40 MEV		$5 \times 10^{10} - 5 \times 10^{13} P/cm^2$
Neutron	1.0 MEV (EQUIV)	$1 \times 10^{10} - 1 \times 10^{13} N/cm^2$

Space flight testing of GaAs solar cells has been limited to two flight programs, the Navy Test Satellite (NTS 2) and the Living Plume Shield (LIPS II). Neither was designed to quantify and qualify radiation damage. They were used only to evaluate GaAs solar cell space performance characteristics and demonstrate the feasibility of using GaAs solar cells as a prime source of space electrical power.^{3, 4}

AFAPL-801 will evaluate and improve radiation damage models of GaAs solar

-
1. Loo, R.Y., Kamath, G.S., and Knectli, R.C. (1982) Medium Energy Proton Radiation Damage to (AlGa)As-GaAs Solar Cells, NASA Report 165946.
 2. Masloski, Kenneth, and Valley, Charles (1982) Neutron and Gamma Irradiation Tests on Advanced Solar Cells, AFWAL-TR-82-2084.
 3. Walker, D. H. (1981) Performance of the Solar Cell Experiments Aboard the NTS-2 Satellite After Three Years in Orbit, NRL Memorandum RPT #4580.
 4. Trumble, T. M. (1982) Space applications of GaAs solar cells, 16th IEEE Photovoltaic Specialist Conference.

cells and will make significant contributions to the JPL Solar Cell Radiation Handbook.⁵ The radiation damage model portion of this experiment depends heavily on the success of the high energy particle measurement experiments on board the CRRES satellite.

3. MEASURING TECHNIQUES

The experiment consists of two solar panels, an ambient panel with 12 cell strings, and an annealing panel with 8 cell strings. The experiment matrix will consist of different cell efficiencies, coverglass material and thickness, inter-connect methods, and temperatures for each panel. During flight, when the cell strings are exposed to the sun, each string will be loaded down with a resistor load bank. At different loads, the open circuit voltage, the short circuit current, and 14 other points of current (I) and voltage (V) will be measured to produce an I-V curve. The I-V curves taken in space will be compared with curves produced from data taken in the laboratory. Changes in the characteristic shapes of these curves and comparisons of different cell strings will provide information on the type of damage and optimum cell string design. Cell string damage will be correlated with on-board radiation measurements.

Radiation types, energy levels, flux levels encountered, and fluence for electrons and protons at specific energy levels will be used for damage correlation studies. This technique is similar to previous laboratory studies.^{1, 2, 3, 4, 5} (See also IEEE Catalog #81.⁶) No previous attempts have been made to optimize GaAs solar cell panel measurements to provide radiation damage and solar cell panel design criteria in consonance with space radiation measurements. This experiment will establish a precedent. An overview of the experiment is given in Figure 12.

-
5. Solar Cell Radiation Handbook, 3rd ed., JPL Publications 82-69.
 6. IEEE Catalog #81 CH1644-4 (1981) Enhanced annealing of GaAs solar cell radiation damage, 15th IEEE Photovoltaic Specialist Conference.

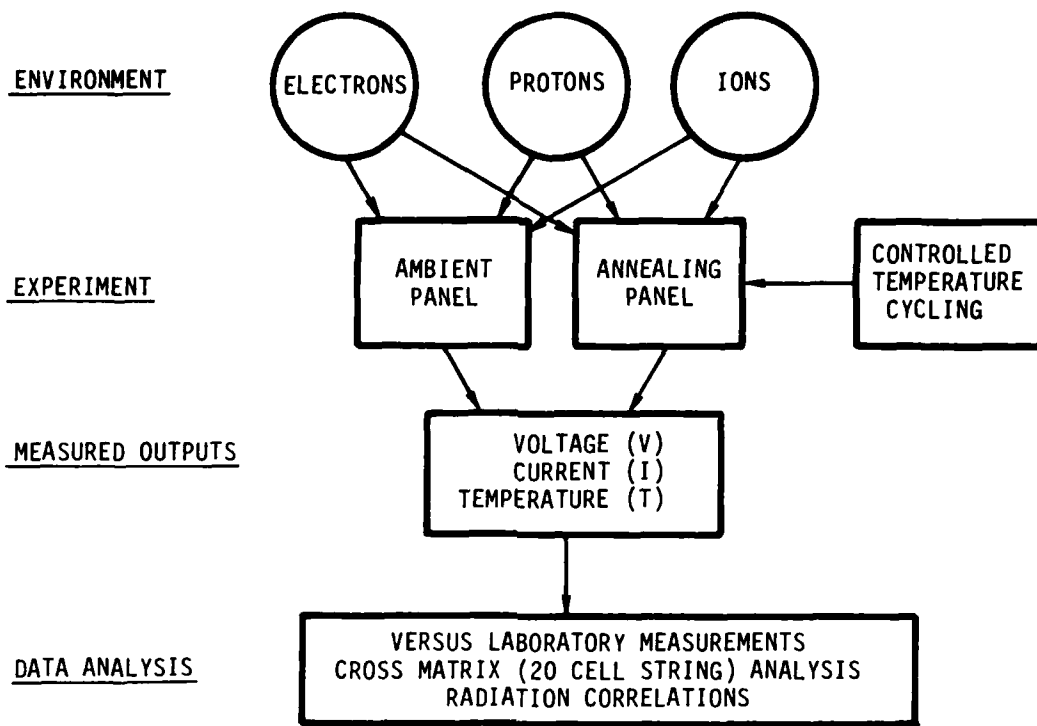


Figure 12. Schematic Overview of the Gallium Arsenide Solar Cell Panel Experiment

References

1. Loo, R. Y., Kamath, G.S., and Knectli, R.C. (1982) Medium Energy Proton Radiation Damage to (AlGa)As-GaAs Solar Cells, NASA Report 165946.
2. Maslowski, Kenneth, and Valley, Charles (1982) Neutron and Gamma Irradiation Tests on Advanced Solar Cells, AFWAL-TR-82-2084.
3. Walker, D. H. (1981) Performance of the Solar Cell Experiments Aboard the NTS-2 Satellite After Three Years in Orbit, NRL Memorandum RPT #4580.
4. Trumble, T. M. (1982) Space applications of GaAs solar cells, 16th IEEE Photovoltaic Specialist Conference.
5. Solar Cell Radiation Handbook, 3rd ed., JPL Publications 82-69.
6. IEEE Catalog #81 CH1644-4 (1982) Enhanced annealing of GaAs solar cell radiation damage, 15th IEEE Photovoltaic Specialist Conference.

IV. Cold Plasma and Fields and Waves

Overview

One of the primary objectives of the CRRES mission is to identify and model critical dynamical processes in the Earth's radiation belts. These dynamical processes involve the transport of energetic charged particles into, within, and out of the radiation belts. Cosmic ray scattering as well as storm and substorm injections are the major sources for new particles. Adiabatic drift motions and cross-L diffusion, maintaining the first and second invariants while violating the third, are the most common interbelt transport processes. L-shell splitting in the outer belts, Coulomb collisions and charge exchange in the inner belts, and ubiquitous pitch angle diffusion processes are the main loss terms. The cold plasma and field sensors on CRRES were specifically designed to study the evolution of particle pitch angle distributions and to identify wave modes and free energy sources responsible for that diffusion.

The plasma and field instruments are a triaxial fluxgate magnetometer, a search coil magnetometer, a passive plasma sounder, and a Langmuir probe. The measurements will be made from three booms. A 6-m "Astromast" boom will hold the fluxgate and search coil magnetometers. The remaining probes are: one fine-wire boom, 100-m tip-to-tip (two 50-m booms); a matched pair of spheres on a nine-wire cable inside a wire boom, 100-m tip-to-tip (two 50-m booms). The wire booms extend out from the top of the satellite (Figure 3) and the Astromast boom extends from Compartment 2 (Figure 4).

The fluxgate magnetometer measures the local geomagnetic field. The particle detectors onboard will use the magnetic field measurement for accurate determination of pitch angle. The local plasma sounder has two components, a single-axis search coil and a cylindrical double probe. It will measure electrostatic and electromagnetic fluctuations over the frequency range 5.6 Hz to 400 kHz. Upper hybrid resonance lines and continuum radiation cutoffs will be used to specify plasma densities (n) in regions where $n < 2000 \text{ cm}^{-3}$. Experience with similar instrumentation on ISEE shows that other wave modes, such as whistlers, chorus, plasmaspheric hiss, ion-cyclotron, electron-cyclotron, and Bernstein waves will be detected at various times and places in the CRRES orbit.

The Langmuir probe electronics box will be connected to both sets of 100-m tip-to-tip booms. Data from the cylindrical booms will be used primarily to monitor the quasi-dc electric field. The second set of booms will employ spherical sensors. It will be programmed to measure either quasi-dc electric field or plasma densities in regions with $n > 1 \text{ cm}^{-3}$. The Langmuir probe is also equipped with a programmable microprocessor with a burst memory. This last feature will allow access to very small scale boundary features that so often in the past have held the keys for significantly advancing our understanding of the magnetosphere.

Contents

1. Scientific Objectives	43
2. Measuring Technique	43

4. The Fluxgate Magnetometer (AFGL-701-13-1)

by

Howard J. Singer and Frederick J. Rich
Air Force Geophysics Laboratory
Hanscom AFB, MA 01731

1. SCIENTIFIC OBJECTIVES

The purpose of the Fluxgate Magnetometer Experiment is to measure the ambient geomagnetic field and low frequency variations in that field from dc to 8 Hz. This measurement will be used--

- (1) together with the look angles of the particle experiments to obtain pitch angles of the measured particles;
- (2) as a diagnostic of global geomagnetic disturbances;
- (3) as a diagnostic of very low frequency waves in the ambient environment;
- (4) to provide plasma gyrofrequencies;
- (5) to measure $v \times B$ electric fields; and
- (6) to provide a secondary source of spacecraft attitude information.

2. MEASURING TECHNIQUE

A Schonstedt Instrument Company triaxial fluxgate magnetometer will measure the Earth's field 16 times per second in the range $\pm 45,000$ nT. The signal from

each sensor will be sent to the Langmuir Probe electronics where it is filtered with an 8-Hz lowpass cutoff to prevent aliasing, and sampled by a 12-bit A/D converter in the ranges $\pm 45,000$ nT and ± 900 nT to provide low and high sensitivity, respectively. For each sample from each axis, a microprocessor will determine whether to enter the high or low sensitivity value into the telemetry stream. Whenever the field strength along an axis is in the high sensitivity range, that value will be entered into the telemetry stream with an appropriate range indicator bit; otherwise, the low sensitivity signal will be sent. Furthermore, once per second the field strength at low sensitivity from all axes will be included in the data stream. More than 70 percent of the time in the planned CRRES orbit will be in field strengths where all three magnetometer axes will be sending data in the high sensitivity range. The magnetometer data can also be sampled in a burst mode as described in the Langmuir probe instrument section. Additionally, the fluxgate signal will be lowpass filtered with a 20-Hz cutoff and provided to the spacecraft in analog form in two different ranges, $\pm 45,000$ nT and $\pm 1,000$ nT.

The three axes of the magnetometer are mutually orthogonal to approximately 0.08° . The sensors are mounted on a rigid, 6.1-m-long Astromast boom (Figure 4) and are far enough away from the spacecraft body so that the vehicle-generated magnetic field will have a strength less than a few nT at the sensor locations. The analog electronics to operate the sensors are mounted inside the spacecraft with a link to the Langmuir probe electronics that will provide voltage regulation and telemetry formatting.

The instrument requires a large dynamic range to measure fields near perigee where the field is $\sim 45,000$ nT and in the vicinity of synchronous orbit where the field is ~ 100 nT or less with periodic variations of amplitude down to fractions of 1 nT. Given the instrument ranges and the 12-bit A/D converter, the least significant bit resolution in each sensor is ~ 22 nT and ~ 0.4 nT at low and high sensitivity respectively. The quantization noise level in high sensitivity is $\sim 2 \times 10^{-3}$ nT²/Hz. On command, the signal from one axis of the magnetometer can be amplified six times to provide better amplitude resolution at low field strengths near apogee. The improved sensitivity will permit the detection of high frequency, low amplitude waves that interact strongly with the plasma environment. The high sensitivity signal from this single axis can also be used to add confidence to the increased accuracy obtained from the other axes by digital averaging.

Contents

1. Scientific Objectives	45
2. Application	47
3. Measuring Techniques	48
References	53

5. The Passive Plasma Sounder (AFGL-701-15) and Search Coil Magnetometer (AFGL-701-13-2)

by

Roger R. Anderson and Donald A. Gurnett
The University of Iowa
Iowa City, IO 52242

I. SCIENTIFIC OBJECTIVES

The purpose of the University of Iowa Passive Plasma Sounder (AFGL-701-15) and Search Coil Magnetometer (AFGL-701-13-2) Experiments, collectively known as the Plasma Wave Experiment on the SPACERAD GTO portion of CRRES, is to measure the plasma wave environment in the Earth's radiation belts. Emphasis will be on high frequency and time resolution, high sensitivities (low noise levels), a large dynamic range, and sufficient frequency response to cover all the characteristic frequencies of the plasma that are of interest. The dynamic range for all the receivers will be about 100 dB (a factor of 10^5 in amplitude) beginning at the respective receiver's noise level. Past plasma wave measurements in the radiation belts show that this range will adequately cover the expected range of plasma wave amplitudes detected by the electric and magnetic sensors. With a 100-m tip-to-tip antenna, this range will allow measurements from the weak levels expected for the continuum radiation and $(n + 1/2) f_g^-$ emissions (f_g^- is the electron gyrofrequency) outside the plasmasphere to the intense levels produced by upper hybrid resonance

noise and ground transmitters observed inside the plasmasphere. It is important to have sufficient sensitivity to measure the weak continuum radiation because the lower cutoff of this radiation is at f_p^- , the electron plasma frequency. The electron number density, N, is determined from $f_p^- = 8.98 \text{ kHz} \times (N)^{1/2}$ where N is in units of electrons per cm^3 . Figure 13 is a plot of the expected variation in the

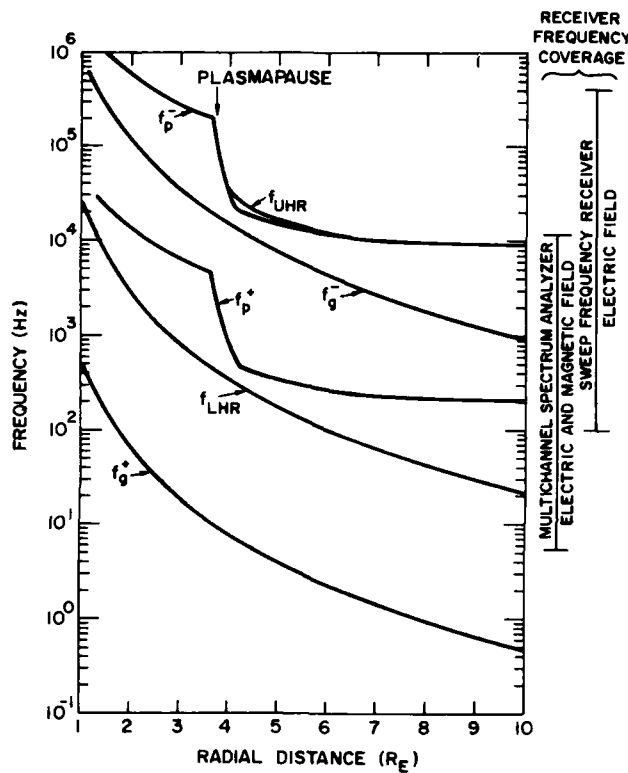


Figure 13. Schematic Variation of Characteristic Plasma Frequencies as a Function of Radial Distance From the Earth

characteristic frequencies of the plasma for a typical CRRES GTO dayside pass. The plots include, in addition to f_p^- and f_g^- , the proton gyrofrequency and plasma frequency, f_p^+ and f_g^+ ; the upper hybrid resonance frequency, $f_{UHR} = [(f_g^-)^2 + (f_p^-)^2]^{1/2}$; and the lower hybrid resonance frequency, $f_{LHR} \approx (f_g^- \times f_g^+)^{1/2}$. Plasma wave emissions tend to occur at these characteristic frequencies or to be bounded by them. The 5.6 Hz to 400 kHz frequency range of the SPACERAD Plasma Wave Instrument covers most of the important characteristic frequencies that CRRES

will encounter in the region above about $2 R_E$ (Earth radii). Below about $2 R_E$, when the plasma frequency exceeds 400 kHz, the Langmuir Probe Experiment will provide the electron number density measurements. Electromagnetic plasma waves below 5.6 Hz will be in the frequency range covered by the Fluxgate Magnetometer Experiment. Electric field fluctuations below 5.6 Hz will be measured by the Langmuir Probe Experiment.

2. APPLICATION

Plasma waves play a major role in changing the energetic particle population in the Earth's radiation belts through pitch angle scattering, ion heating, and other wave-particle interactions (WPI) that exchange energy and/or momentum between the waves and the particles. Identification and characterization of plasma waves involved in WPI in the Earth's radiation belts and magnetosphere have been an important part of space physics research over the past two decades. Kennel and Petschek¹ pioneered studies of the role of electron and ion pitch angle diffusion resulting from plasma wave turbulence in the limiting of stably trapped particle fluxes. They found that resonant cyclotron interactions between whistler and ion cyclotron waves and energetic electrons and protons predicted a reasonable upper limit to trapped particle intensities in rough agreement with observations. Their work provided the framework for many following studies of cyclotron resonance WPI. An extensive review of the role of plasma wave turbulence in particle diffusion in the radiation belts is contained in Schulz and Lanzerotti² and Lyons.³

Extensive reviews of magnetospheric plasma wave observations and WIP studies up to the present time can be found in Shawhan^{4,5} and Anderson.⁶ Lyons concluded that, while the dominant long-term-averaged quiet-time source and

-
1. Kennel, C.F., and Petschek, H.E. (1966) Limit on stably trapped particle fluxes, J. Geophys. Res. 71:1.
 2. Schultz, M., and Lanzerotti, L.J. (1974) Particle Diffusion in the Radiation Belts, Springer-Verlag, Berlin.
 3. Lyons, L.R. (1979) Plasma processes in the Earth's radiation belts, in Solar System Plasma Physics (Vol. 3), L.J. Lanzerotti, C.F. Kennel, and E.N. Parker, Eds., North-Holland Publishing Company, Amsterdam.
 4. Shawhan, S.D. (1979a) Magnetospheric plasma waves, in Solar System Plasma Physics (Vol. 3), L.J. Lanzerotti, C.F. Kennel, and E.N. Parker, Eds., North-Holland Publishing Company, Amsterdam.
 5. Shawhan, S.D. (1979b) Magnetospheric plasma wave research 1975-1978, Rev. Geophys. Space Phys. 17:705.
 6. Anderson, R.R. (1983) Plasma waves in planetary magnetospheres, Rev. Geophys. Space Phys. 21:474.

loss processes for radiation belt electrons and equatorially mirroring protons within the plasmasphere have been correctly identified and quantitatively evaluated, variations of wave distributions and resulting diffusion rates for time scales of a day or less and WPI outside the plasmasphere are less well understood.

The SPACERAD Plasma Wave Experiment instrumentation will not only measure and characterize the plasma wave environment, but will also measure the electron number density and help identify the region of space the satellite is in. Characterization of the plasma waves is important for identifying the wave modes in the WPI and for evaluating the effect of the waves on the particles. The electron number density is a necessary parameter for evaluating wave dispersion relations and determining the resonant energy in the various WPIs. A comparison of the plasma wave measurements with the energetic particle measurements will be used to study the various WPI processes.

3. MEASURING TECHNIQUES

A block diagram of the SPACERAD Plasma Wave Experiment is shown in Figure 14. The Plasma Wave Experiment will measure the electromagnetic and/or electrostatic fields detected by three sensors: (1) a 100-m tip-to-tip extendable fine wire long electric dipole, (2) a search coil magnetometer mounted at the end of a 6-m boom, and (3) a 100-m tip-to-tip spherical double probe electric antenna. The first two sensors are the primary sensors for the Plasma Wave Experiment, and the third is the primary sensor for the Langmuir Probe Experiment. The booms extend from the top of the satellite, as shown in Figure 3. High-input-impedance preamplifiers are located on the spacecraft near the base of each half of the extendable fine wire long electric dipole. The search coil magnetometer contains a high permeability μ -metal core 0.41 m long, wound with 10,000 turns of #42 wire, and a preamplifier. Signals from the sensors, after buffering by appropriate preamplifiers and differential amplifiers, are routed via antenna selection switches to the Sweep Frequency Receiver and the Multichannel Spectrum Analyzer in the Plasma Wave Experiment and to the Langmuir Probe Experiment.

The Sweep Frequency Receiver covers the frequency range from 100 Hz to 400 kHz in four bands with 32 steps per band. The fractional step separation of the Sweep Frequency Receiver, df/f , is about 6.7 percent across the entire frequency range. Band 1 (100 Hz to 810 Hz) is sampled one step per second or 32 seconds per sweep, Band 2 (810 Hz to 6.4 kHz) is sampled two steps per second or 16 seconds per sweep, and Band 3 (6.4 kHz to 51.7 kHz) and Band 4 (51.7 kHz to 400 kHz) are each sampled four steps per second or 8 seconds per sweep. The nominal bandwidths of the four bands are 7 Hz, 56 Hz, 448 Hz, and 3.6 kHz. The four bands

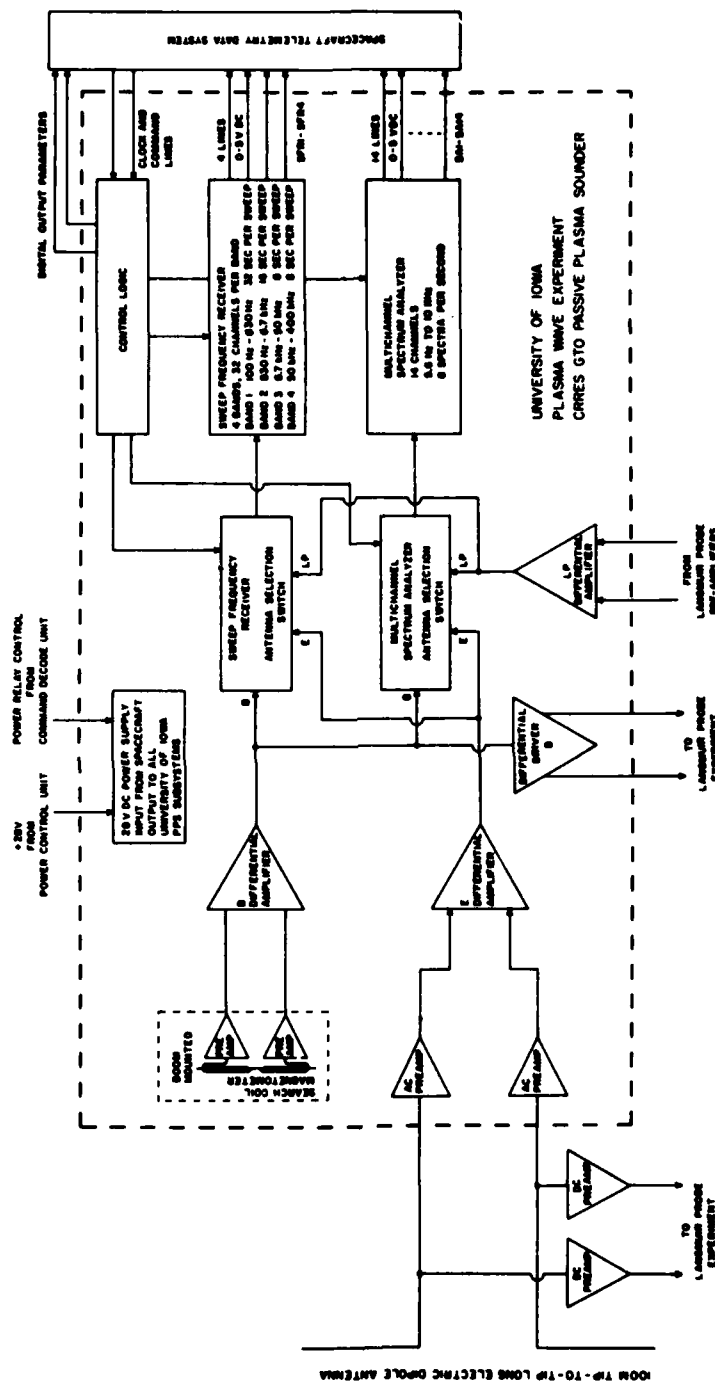


Figure 14. Function Block Diagram for the Plasma Wave Experiment

each have a logarithmic compressor that measures the signal amplitude over about a 100-dB dynamic range beginning at the noise level of the receiver and produces a 0.0 to 5.10-V dc analog output proportional to the logarithm of the input amplitude. Table 5 lists the noise levels and the minimum detectable sine wave amplitudes for the four Sweep Frequency Receiver bands. Table 6 lists the 128 discrete frequencies for the Sweep Frequency Receiver.

The Multichannel Spectrum Analyzer consists of 14 narrow band filters logarithmically spaced in frequency (4 filters per decade in frequency) from 5.6 Hz to 10 kHz followed by 14 logarithmic compressors, each with a dynamic range of about 110 dB. The nominal 3-dB sine wave bandwidth of each narrow band filter is ± 15 percent of the center frequency except for the two highest frequency channels (5.62 kHz and 10.0 kHz) with bandwidths ± 7.5 percent of the center frequency. Frequency response curves for the 14 channels of the Multichannel Spectrum Analyzer are shown in Figure 15. The channel center frequencies, effective noise bandwidths, noise levels, and minimum detectable sine wave amplitudes are listed in Table 7. The 14 0.0- to 5.10-V dc analog outputs are sample simultaneously eight times per second to produce high time resolution spectra.

The Spacecraft Telemetry Data System will provide the clock and command lines for controlling the receivers and the sampling and the analog to digital conversions of the 0.0- to 5.10-V dc analog outputs of the receivers. The Passive Plasma Sounder (PPS) has two high-level relay commands and one 16-bit serial command. The high-level relay commands turn the experiment power on and off. The serial command determines which sensor is connected to which receiver, and whether or not the receivers are locked onto a single sensor or cycle through all the sensors.

Table 5. Plasma Wave Experiment: Sweep Frequency Receiver Noise Levels and Minimum Detectable Sine Wave Amplitude

	Noise Level (V ² Hz)	Minimum Detectable Sine Wave Amplitude (V)
Band 1 (100 Hz to 810 Hz) (Bandwidth = 7 Hz)	2.5×10^{-12}	4.2×10^{-6}
Band 2 (810 Hz to 6.4 kHz) (Bandwidth = 56 Hz)	4.5×10^{-13}	5.0×10^{-6}
Band 3 (6.4 kHz to 51.7 kHz) (Bandwidth = 448 Hz)	3.9×10^{-14}	4.2×10^{-6}
Band 4 (51.7 kHz to 400 kHz) (Bandwidth = 3.6 kHz)	1.3×10^{-14}	6.9×10^{-6}

Table 6. Discrete Frequencies for the CRRES Plasma Wave Experiment
Frequency Receiver in kHz

Step No.	Band 1	Band 2	Band 3	Band 4
01	0.104	0.836	6.69	53.5
02	0.113	0.904	7.23	57.9
03	0.122	0.973	7.78	62.2
04	0.130	1.04	8.33	66.7
05	0.139	1.11	8.89	71.1
06	0.148	1.18	9.45	75.6
07	0.157	1.25	10.0	80.2
08	0.166	1.32	10.6	84.7
09	0.175	1.40	11.2	89.4
10	0.184	1.47	11.8	94.0
11	0.202	1.61	12.9	103
12	0.211	1.69	13.5	108
13	0.230	1.84	14.7	118
14	0.250	2.00	16.0	128
15	0.259	2.07	16.6	133
16	0.279	2.23	17.9	143
17	0.289	2.31	18.5	148
18	0.309	2.47	20.0	158
19	0.330	2.64	21.1	169
20	0.351	2.81	22.5	180
21	0.372	2.98	23.8	191
22	0.394	3.15	25.2	202
23	0.428	3.42	27.4	219
24	0.451	3.61	28.8	231
25	0.486	3.89	31.1	249
26	0.510	4.08	32.6	261
27	0.547	4.38	35.0	280
28	0.585	4.68	37.4	299
29	0.624	4.99	39.9	320
30	0.678	5.43	43.4	347
31	0.721	5.77	46.1	369
32	0.799	6.23	49.9	399

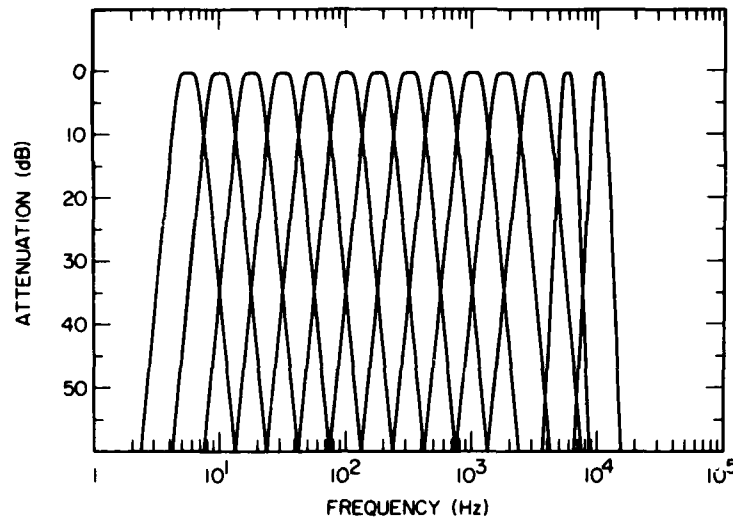


Figure 15. Frequency Response Curves for the 14 Channels of the Multichannel Spectrum Analyzer in the Plasma Wave Experiment

Table 7. Plasma Wave Experiment: Multichannel Spectrum Analyzer Characteristics

Channel Number	Center Frequency	Effective Noise Bandwidth	Noise Level (V^2/Hz)	Minimum Detectable Sine Wave Amplitude (V)
01	5.6 Hz	1.12 Hz	3.5×10^{-10}	2.0×10^{-5}
02	10.0 Hz	2.00 Hz	9.4×10^{-11}	1.4×10^{-5}
03	17.8 Hz	3.56 Hz	4.3×10^{-11}	1.2×10^{-5}
04	31.1 Hz	6.22 Hz	1.6×10^{-11}	1.0×10^{-5}
05	56.2 Hz	11.20 Hz	8.4×10^{-12}	9.7×10^{-6}
06	100. Hz	20.0 Hz	4.4×10^{-12}	9.4×10^{-6}
07	178. Hz	35.6 Hz	1.8×10^{-12}	7.9×10^{-6}
08	311. Hz	62.2 Hz	5.0×10^{-13}	5.6×10^{-6}
09	562. Hz	112. Hz	1.8×10^{-13}	4.4×10^{-6}
10	1.00 kHz	200. Hz	8.5×10^{-14}	4.1×10^{-6}
11	1.78 kHz	356. Hz	2.6×10^{-14}	3.1×10^{-6}
12	3.11 kHz	622. Hz	1.6×10^{-14}	3.2×10^{-6}
13	5.62 kHz	560. Hz	2.3×10^{-14}	3.6×10^{-6}
14	10.0 kHz	1.00 kHz	3.5×10^{-15}	1.9×10^{-6}

The PPS experiment has three status words: two analog words, the Low Voltage Power Supply Monitor (LVPS) located in Frame 1 of Subcom 18 and the Search Coil Magnetometer temperature (TEMP) located in Frame 3 of Subcom 18, and the PPS Serial/Digital (S/D) Status word located in Frame 1 of Subcom 19. Calibration tables or algorithms for determining the LVPS and TEMP values will be available when the instrument is completed.

References

1. Kennel, C.F., and Petschek, H.E. (1966) Limit on stably trapped particle fluxes, J. Geophys. Res. 71:1.
2. Schultz, M., and Lanzerotti, L.J. (1974) Particle Diffusion in the Radiation Belts, Springer-Verlag, Berlin.
3. Lyons, L.R. (1979) Plasma processes in the Earth's radiation belts, in Solar System Plasma Physics (Vol. 3), L.J. Lanzerotti, C.F. Kennel, and E.N. Parker, Eds., North-Holland Publishing Company, Amsterdam.
4. Shawhan, S.D. (1979a) Magnetospheric plasma waves, in Solar System Plasma Physics (Vol. 3), L.J. Lanzerotti, C.F. Kennel, and E.N. Parker, Eds., North-Holland Publishing Company, Amsterdam.
5. Shawhan, S.D. (1979b) Magnetospheric plasma wave research 1975-1978, Rev. Geophys. Space Phys. 17:705.
6. Anderson, R.R. (1983) Plasma waves in planetary magnetospheres, Rev. Geophys. Space Phys. 21:474.

Contents

1. Scientific Objectives	55
2. Applications	57
3. Measuring Techniques	57
References	63

6. The Langmuir Probe Instrument (AFGL-701-14)

by

W.J. Burke, W.P. Sullivan, and M. Smiddy
Air Force Geophysics Laboratory
Hanscom AFB, MA 01731

J R. Wygant, P.R. Harvey, and F.S. Mozer
Space Sciences Laboratory
University of California
Berkeley, CA 94720

R.B. Torbert
Center for Astrophysics and Space Sciences
University of California at San Diego
La Jolla, CA 92093

M.C. Kelley
School of Electrical Engineering
Cornell University
Ithaca, NY 14853

N. Maynard
Code 696 NASA/Goddard Space Flight Center
Greenbelt, MD 20771

1. SCIENTIFIC OBJECTIVES

The Langmuir probe instrument for CRRES is designed to measure variations in cold electron temperature and density and in electric fields, which are crucial to the understanding of the wave modes and instabilities responsible for wave-par-

ticle interactions (WPI). Such interactions are responsible for pitch angle scattering of radiation belt protons and electrons into the atmosphere. During strong geomagnetic substorms, CRRES may observe processes characteristic of auroral magnetic field lines including solitary waves, double layers, and other plasma structures with electric fields parallel to the magnetic field. Such nonlinear wave modes have been observed at lower altitudes by the S3-3 satellite¹ and may account for ion beams streaming out of the ionosphere. Such ions may be a major constituent of the radiation belts during magnetically active periods.

In addition, the ability of the instrument to measure quasistatic dc electric fields at and within geosynchronous orbit allows a detailed study of electric fields responsible for the earthward convection of particles from the plasma sheet, and the radial diffusion and energization of radiation belt particles to energies up to 1 MeV. Theoretical models describing the penetration of fluctuating electric fields from the outer magnetosphere into the plasmasphere have not been tested in a systematic way with in situ measurements of plasmaspheric electric fields. Mozer² provided evidence that electric fields fluctuating with periods of less than about 10 hours effectively penetrate the Alfvénic shielding layer, while slower varying fields are shielded from the plasmasphere. The only measured radial diffusion coefficient is based on balloon measurements of electric fields in the ionosphere at L=6 by Holzworth et al.³ Measurements of ionospheric electric fields by radar have established that penetration of electric fields to low latitudes can occur during substorms.^{4, 5, 6}

-
1. Temerin, M., Cerny, K., Lotko, W., and Mozer, F.S. (1982) Observations of double layers and solitary waves in the auroral plasma, Phys. Rev. Lett. 48:1175.
 2. Mozer, F.S. (1971) Power spectra of the magnetospheric electric field, J. Geophys. Res. 76:3651.
 3. Holzworth, R.H., and Mozer, F.S. (1979) Direct measurement of the radial diffusion coefficient near L=6 due to electric field fluctuations, J. Geophys. Res. 84:2559.
 4. Holzworth, R., Wygant, J.R., Mozer, F.S., Gonzales, C.A., Greenwald, R., Blanc, M., Vickery, J., and Kishi, A. (1981) Global ionospheric electric field measurements in April 1978, J. Geophys. Res. 86:6859.
 5. Fejer, B.G., Gonzales, C.A., Farley, D.T., Kelley, M.C., and Woodman, R.F. (1979) Equatorial electric fields during magnetically disturbed conditions: 1. The effect of the interplanetary field, J. Geophys. Res. 84:5797.
 6. Gonzales, C.A., Kelley, M.C., Fejer, B.G., Vickery, J.F., and Woodman, R.F. (1979) Auroral and equatorial electric fields during magnetically disturbed conditions: 2. Implications of simultaneous auroral and equatorial measurements, J. Geophys. Res. 84:5803.

2. APPLICATIONS

A discussion of the physics of the measurements of electric fields under the variety of conditions offered by space plasmas is presented in Mozer.⁷ Similar double probe sensors have been flown at ionospheric altitudes on S3-2⁸ and S3-3,⁹ and in the magnetosphere on the International Sun-Earth Explorer.^{10, 11}

The CRRES instrument is even more sophisticated than the ISEE-1 instrument in several ways. Advances in the technology of high density RAM memory have allowed 192 kbytes of burst memory to be incorporated in the present instrument rather than the 256 bytes in the ISEE-1 instrument. The frequency response of the CRRES instrument is improved over that of the ISEE-1 instrument. The inherent frequency response of the electric field instrument on CRRES is several megahertz, while that on ISEE-1 was about 100 kilohertz. Finally, the addition of electrostatic guards that can be biased at arbitrary potentials relative to the spherical probes allow the control and limitation of photoelectron flux from the spherical sensors to the spacecraft. This limits asymmetric charging effects that contributed to several mV/m offsets in the electric field measurements on the ISEE-1 and GEOS spacecrafats when they were in low density plasmas.¹¹

3. MEASURING TECHNIQUES

The CRRES Langmuir probe instrument consists of two pairs of orthogonal booms with 100-m tip-to-tip separations in the spin plane of the satellite. At the tips of opposing booms are conducting sensors. For one set of booms, these sen-

-
7. Mozer, F.S. (1973) Analysis of techniques for measuring dc and ac electric fields, Space Sci. Rev. 14:272.
 8. Burke, W.J., Hardy, D.A., Rich, F.J., Kelley, M.C., Smiddy, M., Shuman, B., Sagalyn, R.C., Vancour, R.P., Wildman, P.J.L., and Lai, S.T. (1980) Electrodynamical structure of the late evening sector of the auroral zone, J. Geophys. Res. 85:1179.
 9. Mozer, F.S., Cattell, C.A., Hudson, M.K., Lysak, R.L., Temerin, M., and Torbert, R.B. (1980) Satellite measurements and theories of low altitude particle acceleration, Space Sci. Rev. 27:155.
 10. Mozer, F.S., Torbert, R.B., Fahleson, U.V., Falthammar, C.-G., Gonfalone, A., and Pedersen, A. (1978) Measurements of quasistatic and low frequency electric fields with spherical double probes on the ISEE-1 space-craft, IEEE Trans. Geosci. Electronics GE-16:258.
 11. Pedersen, A., Cattell, C.A., Falthammar, C.-G., Formisano, V., Lindqvist, P.-A., Mozer, F., and Torbert, R. (1984) Quasistatic electric field measurements with spherical double probes on the GEOS and ISEE satellites, Space Sci. Rev. 37:269.

sors are spheres. For the other, they are cylindrical antennas shared by the Passive Plasma Sounder and the Langmuir probe. The Langmuir probe has two different operating modes controlled by an on-board microprocessor. In the Langmuir probe mode, the spherical sensors are biased at fixed potentials relative to the plasma, and the current collected by the spheres is measured to provide information on cold electron temperature and density. In the electric field mode, the sensors are current-biased and measure electric fields by determining the potential difference between opposing sensors.

Figure 16 illustrates the primary components of the spherical and cylindrical probe units. Inboard and outboard of the sphere are stub segments several meters long and short guard segments. These stubs and guards are driven at potentials with respect to the sphere that are controlled by the microprocessor and/or determined for each by ground command. They control the photoelectron flux from the sphere to the spacecraft, which can produce several mV/m offsets in the electric field measurement.

The surface of each sensor is connected to a high input impedance unity gain preamplifier inside each sphere and at the bases of the cylindrical wire antennas. The preamps have an input impedance greater than 10^8 ohms, exceeding the dc source impedance of the plasma by two orders of magnitude. The input capacitance of the sphere preamps is 0.25 pF, while the coupling capacitance of the 8-cm-diameter spheres is about 5 pF. Thus, the ac signals are attenuated a few percent. The sphere preamplifier bandwidth is more than 1 MHz, and the dc differential signal dynamic range is ± 100 V. The high input impedance preamplifiers at the base of the cylindrical probes have a frequency response from dc to over 1 MHz and a dynamic range over ± 35 V. The sphere and cylinder preamplifiers have a calibration mode in which arbitrary dc potentials can be placed on the input of the preamps to verify the output gains and operations of the instrument electronics.

3.1 Current Biasing

An important capability of the experiment in the electric field mode is putting a bias current on the sensors. The impedance between the sensor and the plasma is a nonlinear function of the current flowing from the sensor to the plasma (bias current). Thus, the accuracy of the electric field experiment can be maximized by determining the impedance as the function of bias current and by applying the optimum value of bias current to the sensor. The value of the bias current to the sensors can be adjusted between $+0.36 \mu\text{A}$ and $-0.36 \mu\text{A}$ in 256 linear steps. The bias current can either be set by ground command, or set to an optimum value determined by the digital control circuitry through on-board microprocessor analysis of bias sweeps or to a current that varies sinusoidally at the spin frequency.

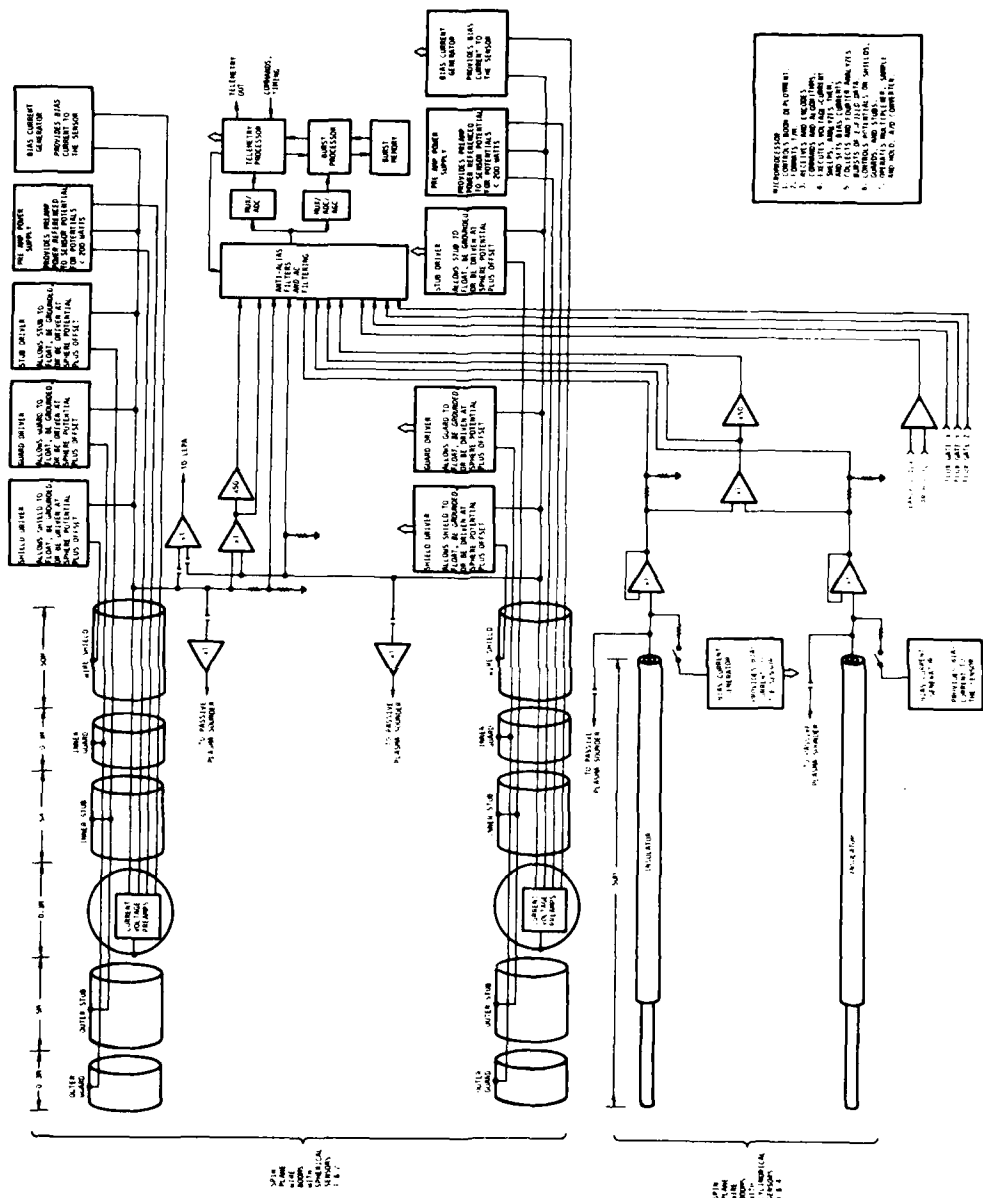


Figure 16. Function Block Diagram for the Langmuir Probe Experiment

3.2 Langmuir Probe Mode

During the Langmuir probe modes of operation, the spheres are biased at fixed voltages and their collected currents are measured. These modes measure the temperature and density of electrons with energies on the order of a few electron volts. Sphere currents are digitized by both the telemetry and burst electronics. During this mode of operation, voltage sweeps are used in the place of current sweeps as described above.

To determine the contributions of photoelectron fluxes from the stubs, guards, and spacecraft to the total current drawn by the spheres, a diagnostic sequence of voltage values is placed on the stubs and guards. Each offset value is put on the stub for a programmable number of cycles of the voltage biasing.

3.3 MUX and Analog to Digital Electronics

Selected potential difference measurements, the analog outputs of bandpass filter banks, the potentials of each sensor, analog data from the three component measurement of the fluxgate magnetometer, and high frequency measurements from the search coil magnetometer are fed through a network of programmable and fixed anti-aliasing filters and into the telemetry and burst multiplexors. The voltage, current, and magnetometer measurements that have been processed by an Automatic Gain Control (AGC) circuit also go into the burst and telemetry multiplexors. Each multiplexor has a dedicated 12-bit A-D converter. The list of digitizable main telemetry quantities is given in Table 8, and a list of digitizable burst quantities is given in Table 9.

The Langmuir probe will provide potential difference measurements to the low energy Plasma Analyzer (AFGL-701-6) for on-board correlation with particle measurements and also to the Passive Plasma Sounder (AFGL-701-15).

3.4 Microprocessor Control

The Langmuir probe has two microprocessors. One is responsible for telemetry formatting, command reception and execution, sensing burst conditions, boom deployment, current and voltage sweeps, gain decisions, and other control functions. The second microprocessor is responsible for continuously collecting burst data and playing it back through the telemetry. Both contain sufficient RAM memory for substantial ground reprogramming. This capability was very useful in the ISEE-1 MOM experiment, although the amount of RAM available was far too small and hindered some experimentation.

3.5 Burst Memory

Filling the burst memory is controlled by the burst microprocessor, which

Table 8. Langmuir Probe: Main Telemetry Quantities

- | | |
|------|--|
| (1) | Potential difference between spherical probe 1 and the spacecraft or current gathered from spherical probe 2 (low frequency) |
| (2) | Potential difference between spherical probes or current collected by sphere 1 (low frequency signal) |
| (3) | Potential difference between spherical probe 1 and spacecraft or the current gathered by sphere 1 |
| (4) | Automatic Gain Control (AGC) |
| (5) | Potential difference between spherical probe 1 and spacecraft or the current gathered by sphere 1 |
| (6) | Potential difference between Cylindrical Probes |
| (7) | Bandpass filter 1 (center frequency = 32 Hz) |
| (8) | Bandpass filter (center frequency = 256 Hz) |
| (9) | Bandpass filter filter 3 (center frequency = 2046 Hz) |
| (10) | Search coil |
| (11) | Potential difference between spherical probe 1 and spacecraft |
| (12) | Potential difference between cylindrical probe 3 and spacecraft |
| (13) | Potential difference between cylindrical probe 4 and spacecraft |
| (14) | Fluxgate magnetometer x component |
| (15) | Fluxgate magnetometer y component |
| (16) | Fluxgate magnetometer z component |

monitors electric and magnetic field data to determine when a threshold set by ground command is exceeded. All or part of the burst memory is filled at the occurrence of this "event." The data rate, duration of filling the memory, and the sequence of quantities fed into the memory are controlled by ground command. Because of the fast digitization rate, a separate 12-bit A-D converter is used for burst data collections. Data are sampled at commandable rates less than or equal to the maximum rate of 50,000 quantities per second and are stored in the burst memory for a commanded length of time or until the memory is filled. The size

Table 9. Langmuir Probe: Burst Telemetered Quantities

- | | |
|------|--|
| (1) | Voltage between spherical probe 2 and spacecraft or current collected from spherical probe 2 |
| (2) | Potential difference between spherical probe 2 and spherical probe 1 or current collected by spherical probe 1 |
| (3) | Signal from search coil magnetometer or potential between spherical probe 2 and spacecraft |
| (4) | Potential between spherical probe 2 and spacecraft |
| (5) | Potential differential between two cylindrical probes (high frequency) |
| (6) | Potential difference between cylindrical probe 3 and spacecraft |
| (7) | DC potential difference between the two cylindrical probes |
| (8) | Potential difference between spherical probe 1 and spherical probe 2 (high frequency) |
| (9) | Potential difference between probe 3 and the spacecraft |
| (10) | Fluxgate magnetometer x axis |
| (11) | Fluxgate magnetometer y axis |
| (12) | Fluxgate magnetometer z axis |
| (13) | Automatic Gain Control (AGC) |

of this memory is 192 kbytes (8 bits per byte). The ROM algorithm for burst sampling allows a great deal of flexibility in sampling these data. The quantities to be sampled, their ordering, the frequency of the samples, and the amount of the event preamble to be saved are all ground programmable. The microprocessor allows up to 16 quantities sampled. This yields the possibility for more sophisticated sampling scenarios where some quantities are sampled more often than others, effectively giving higher resolution to those quantities.

References

1. Temerin, M., Cerny, K., Lotko, W., and Mozer, F.S. (1982) Observations of double layers and solitary waves in the auroral plasma, Phys. Rev. Lett. 48:1175.
2. Mozer, F.S. (1971) Power spectra of the magnetospheric electric field, J. Geophys. Res. 76:3651.
3. Holzworth, R.H., and Mozer, F.S. (1979) Direct measurement of the radial diffusion coefficient near L=6 due to electric field fluctuations, J. Geophys. Res. 84:2559.
4. Holzworth, R., Wygant, J.R., Mozer, F.S., Gonzales, C.A., Greenwald, R., Blanc, M., Vickery, J., and Kishi, A. (1981) Global ionospheric electric field measurements in April 1978, J. Geophys. Res. 86:6859.
5. Fejer, B.G., Gonzales, C.A., Farley, D.T., Kelley, M.C., and Woodman, R.F. (1979) Equatorial electric fields during magnetically disturbed conditions: 1. The effect of the interplanetary field, J. Geophys. Res. 84:5797.
6. Gonzales, C.A., Kelley, M.C., Fejer, B.G., Vickery, J.F., and Woodman, R.F. (1979) Auroral and equatorial electric fields during magnetically disturbed conditions: 2. Implications of simultaneous auroral and equatorial measurements, J. Geophys. Res. 84:5803.
7. Mozer, F.S. (1973) Analysis of techniques for measuring dc and ac electric fields, Space Sci. Rev. 14:272.
8. Burke, W.J., Hardy, D.A., Rich, F.J., Kelley, M.C., Smiddy, M., Shuman, B., Sagalyn, R.C., Vancour, R.P., Wildman, P.J.L., and Lai, S.T. (1980) Electrodynamical structure of the late evening sector of the auroral zone, J. Geophys. Res. 85:1179.
9. Mozer, F.S., Cattell, C.A., Hudson, M.K., Lysak, R.L., Temerin, M., and Torbert, R.B. (1980) Satellite measurements and theories of low altitude particle acceleration, Space Sci. Rev. 27:155.

10. Mozer, F.S., Torbert, R.B., Fahleson, U.V., Falthammar, C.-G., Gon-falone, A., and Pedersen, A. (1978) Measurements of quasistatic and low frequency electric fields with spherical double probes on the ISEE-1 space-craft, IEEE Trans. Geosci. Electronics GE-16:258.
11. Pedersen, A., Cattell, C.A., Falthammar, C.-G., Formisano, V., Lindqvist, P.-A., Mozer, F., and Torbert, R. (1984) Quasistatic electric field measurements with spherical double probes on the GEOS and ISEE satellites, Space Sci. Rev. 37:269.

V. Particle Experiments

Overview

SPACERAD particle detectors are designed to give measurements with high time, angular, and energy resolution of: electrons, from 10 eV to 10 MeV; protons, from 10 eV to 600 MeV; and the major ion species, from 40 eV/Q to 15 MeV/ion. Additional information will be provided by supporting experiments from the Lockheed Electron and Proton Spectrometer and Mass Composition Experiments, and the University of Chicago Cosmic Ray Experiment. In addition, SPACERAD will provide dose measurements by two very different methods.

The data from these experiments will be used (a) to provide concurrent environmental specification for the Engineering Experiments, particularly for the Microelectronics Experiment; (b) to extend existing static radiation belt models in energy, pitch angle, and ion composition; and (c) to study in detail the dynamic processes of the radiation belts.

Table 10 is a summary list of the particle detectors, their energy ranges, energy resolution, and angular resolution. Figures 17 and 18 show graphically the energy ranges covered for electrons and ions, respectively. They also show, by cross-hatched regions, where cross-calibration of the particle detectors will be made. Each instrument will be fully calibrated at the facility listed in the right-hand column.

Table 10. Particle Detector Characteristics

NUMBER	AGENCY	MEASUREMENT	ENERGY RESOLUTION	ANGULAR RESOLUTION
701-6	AFGL/EMMANUEL/MULLARD	ELECTRONS/PHOTONS 10 eV - 30 keV	3%	$\pm 2.8^\circ \times \pm 4.0^\circ$ STANDARD MODE $\pm 2.8^\circ \times \pm 0.5^\circ$ LOSS CONE MODE
701-5B	AEROSPACE/MAX PLANCK	ELECTRONS PROTONS	20 - 250 keV 40 keV - 2 MeV	$\pm 2.0^\circ \times \pm 3.0^\circ$ $\pm 2.0^\circ \times \pm 5.0^\circ$
307-3	LOCKHEED	ELECTRONS PROTONS	20 keV - 5 MeV 500 keV - 10 MeV	24 CHANNELS* 48 CHANNELS*
307-8A	LOCKHEED	IONS	0.1 - 32 keV/Q	6° CONICAL
307-8B	LOCKHEED	IONS	20 - 8000 keV-AMU/Q	6° CONICAL
701-11B	AEROSPACE/LASL	IONS	40 eV/Q - 40 keV/Q	10%
701-11A	AEROSPACE/MAX PLANCK	IONS	30 - 300 keV/Q	10%
701-11C	AEROSPACE/LASL	IONS	100 keV/AMU - 15 MeV/AMU	<10% 6° CONICAL
701-5A	AEROSPACE	ELECTRONS	30 keV - 2 MeV	18 CHANNELS*
701-4	AFGL/PANAMETRICS	ELECTRONS	1 - 10 MeV	10 CHANNELS*
701-8, 9	AFGL/EMMANUEL/MIT	PROTONS	1 - 100 MeV	24 CHANNELS*
701-7A	AEROSPACE	PROTONS	20 - 80 MeV	$\pm 10^\circ \times \pm 10^\circ$ LOW ENERGY $\pm 12^\circ \times \pm 17^\circ$ HIGH ENERGY
701-7B	AEROSPACE	PROTONS	>320, >440 MeV	2 CHANNELS
604	U. CHICAGO	IONS	20 - >500 MeV/AMU	<1% 1° CONICAL

* CHANNEL DEPENDENT ENERGY RESOLUTION

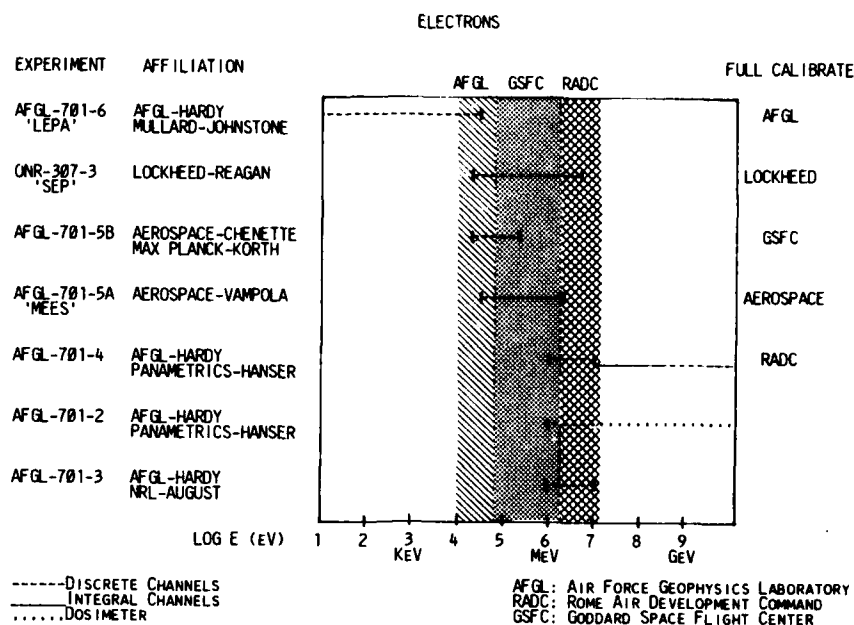


Figure 17. Individual Energy Ranges for Electron Experiments

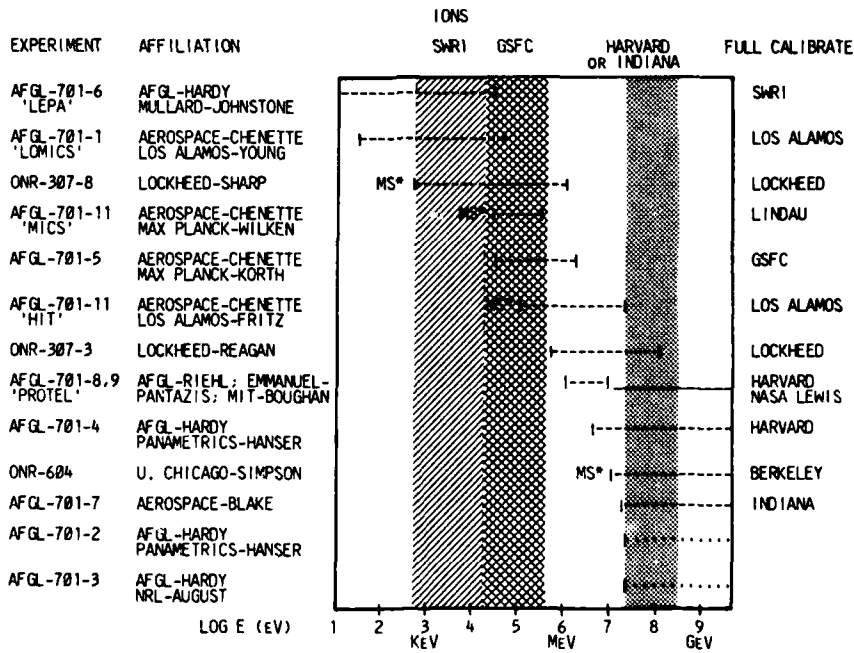


Figure 18. Individual Energy Ranges for Ion Experiments

Contents

1. Scientific Objectives	69
2. Application	70
3. Measuring Technique	71
4. Function Block Diagram	73
References	75

7. The Low Energy Plasma Analyzer (AFGL-701-6)

by

D.A. Hardy
Air Force Geophysics Laboratory
Space Physics Division
Hanscom AFB, MA 01731

A.D. Johnstone and M.F. Smith
Mullard Space Science Laboratory
University College London
Holmbury St. Mary, Dorking
Surrey, RH56NT, UK

P. Gough
School of Mathematical and Physical Sciences
University of Sussex
Brighton, BN190H, UK

A. Huber, J. Pantazis, and R. Burkhardt
Physics Research Division
Emmanuel College
Boston, MA 02115

1. SCIENTIFIC OBJECTIVES

The Low Energy Plasma Analyzer for CRRES is designed to measure the three dimensional distribution function of electrons and ions in the energy range from 10 eV to 30 keV and to determine where in the distribution function and at what frequency wave-particle interactions occur. Both the plasma sheet and the plasma

injected into the inner magnetosphere during substorms are primarily composed of particles in this energy range, an energy range considered low compared with radiation belt particles. The low energy plasma plays a major role in the dynamics of the inner magnetosphere. Because the particles serve as a source for the radiation belts, this plasma and its interaction with the ambient waves and fields must be understood for the development of a dynamic radiation belt model.

2. APPLICATION

Electrostatic analyzers of various geometries have been used for many years as the primary means of measuring both electrons and ions in the energy range from thermal energies to energies in the neighborhood of 50 keV. Many of these analyzers have been basically monodirectional, determining pitch angle effects by relying on the spin of the satellite or on a motor driven system.^{1, 2, 3, 4} Two difficulties exist with such systems. First, since they rely on a motor system or satellite spin to provide pitch angle variation, they, of necessity, convolve spatial, temporal, and pitch angle effects. Second, since they typically measure in a plane defined by the satellite spin vector, they can only define two dimensional distribution functions.

Recently, particle experiments have been designed to make increasingly sophisticated, simultaneous, multiangular measurements. This has been accomplished in two ways: first, by creating arrays of monodirectional detectors,^{5, 6} and second, by using spherical geometries to make multiangular measurements

-
1. Heikkila, W.J., Smith, J.B., Jarstrup, J., and Winningham, J.D. (1970) The soft particle spectrometer in the ISIS-I satellite, Rev. Sci. Instr. 41:1393.
 2. McIlwain, C. (1971) UCSD Experiments and Operations Manual for the Environmental Measurements Experiment on the Applications Technology Satellite Mission ATS-F, Westinghouse Defense and Space Center Document 710667, pp. 4-109.
 3. Hardy, D.A., Gussenhoven, M.S., and Huber, A. (1979) The Precipitating Electron Detectors (SSJ/3) for the Block 5D/Flights 2-5 DMSP Satellites: Calibration and Data Presentation, AFGL-TR-79-0210, AD A083136.
 4. Vampola, A.L., and Kuch, G.A. (1978) Induced precipitation of the inner zone electrons: 1. Observations, J. Geophys. Res. 83:2543.
 5. Winningham, J.D., Burch, J.L., Eakers, N., Blevins, V.A., and Hoffman, R.A. (1981) The low altitude plasma instrument (LAPI), Space Sci. Instrumentation 5:465.
 6. Burch, J.L., Winningham, J.D., Blevins, V.A., Eakers, N., Gibson, W.C., and Hoffman, R.A. (1981) High-altitude plasma instrument for Dynamics Explorer-A, Space Sci. Instrumentation 5:455.

through a single sensor.^{7,8} These detectors have been capable of making true measurements of the three dimensional distribution function. The Low Energy Plasma Analyzer is of the second type,⁹ where, by taking advantage of increased understanding of particle motion in a spherical analyzer, the three dimensional distribution will be specified to an accuracy in pitch angle of 1 degree.

3. MEASURING TECHNIQUE

The basic sensors of the experiment are two 260° spherical electrostatic analyzers. The geometry of the sensors is shown in Figure 19. Each analyzer consists of two concentric spherical plates. On one edge, the space between the plates is closed off except for the entrance aperture. Along the other edge, a microchannel plate is positioned. The entrance aperture limits particle access to an angular fan of approximately 5.6° by 128°. A symmetric potential is applied to the plates. The electric field produced is such that, for a fixed potential, only particles within a 3-percent energy band of the central energy defined by the potential have great circle trajectories within the space between the plates that will intersect the microchannel plate. The focussing of the system is such that within the 128° angle defined by the entrance aperture, the particles' pitch angles are imaged onto the microchannel plate to an accuracy of less than 1 degree.

Particles that impact the microchannel plate produce an electron cascade, resulting in a measurable pulse. A discrete anode system determines the position of such pulses along the microchannel plate. Particle positions are sorted into sixteen 8° zones spanning the 128° fan. In addition, any one 8° zone can be sorted into eight 1° zones to image the atmospheric loss or source cones. The preamplified pulses from each 8° zone are also fed out in parallel to a particle correlator board. The particle correlator records the arrival times of each electron or ion within each 8° zone with a high frequency clock. An on-board microprocessor then performs an autocorrelation to determine any high frequency bunching in the

-
7. Frank, L.A., Yeager, D.M., Owens, H.D., Ackerson, K.L., and English, M.R. (1978) Quadrangular LEPEDEAS for ISEE's 1 and 2 plasma experiments, IEEE Trans. Geosci. Electronics GE-16:221.
 8. Bame, S.J., Asbridge, J.R., Felthauer, H.E., Glare, J.P., Paschmann, T., Hemmerick, P., Lebmann, K., and Rosenbauer, H. (1978) ISEE-1 and ISEE-2 fast plasma experiments and the ISEE-3 solar wind experiment, IEEE Trans. Geosci. Electronics GE-16:216.
 9. Coates, A.J., Johnstone, A.D., Kellock, S.J., Smith, M.F., Booxes, T., and Winningham, S.D. (1984) A Space-Borne Plasma Analysis for Three-Dimensional Measurements of the Velocity Distribution. Submitted to IEEE 1984 Nucl. Sci. Sympos., Fla.

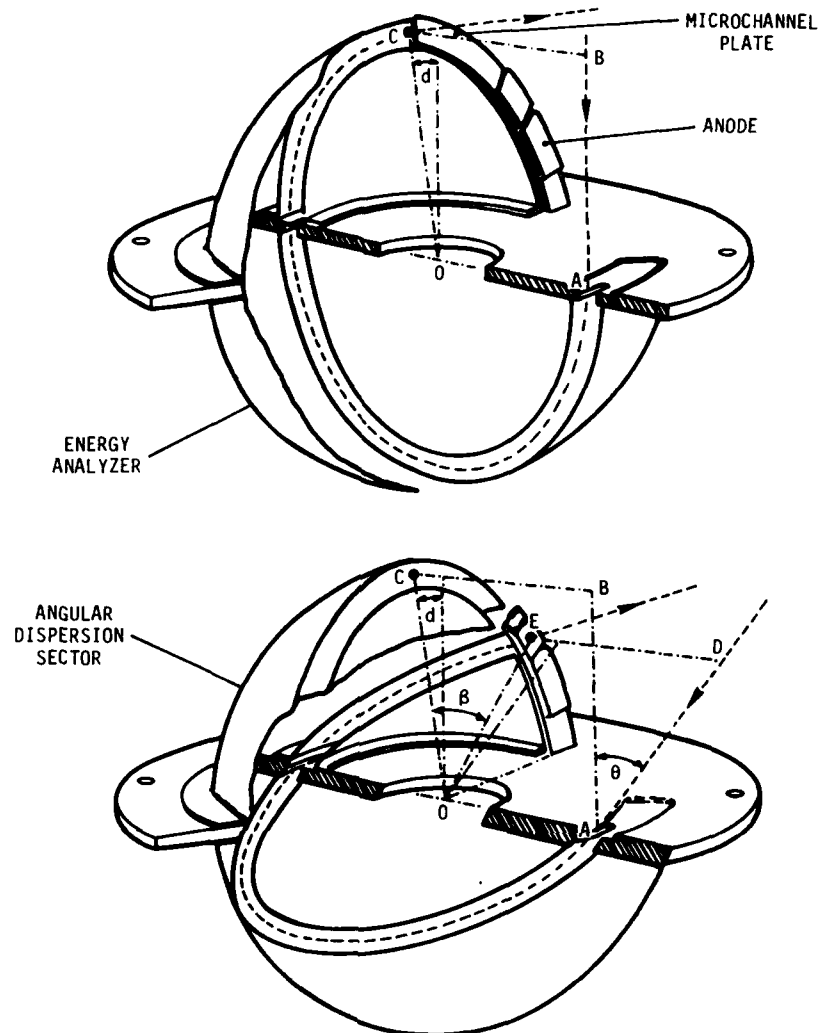


Figure 19. Schematic Diagram of the Low Energy Plasma Sensor Showing Trajectories Within the Detector for Particles Incident at Two Different Locations

particle arrival times produced by WPI. The correlator also receives as input the ac signal from the electric field antenna. The correlator determines the zero crossing times of this signal and then cross correlates this with the particle timing data as an additional technique to identify WPIs.

The number of voltage steps per sweep can be set between 1 and 128. The experiment will normally operate so that 30 point spectra will be taken twice a second, or a 120 point spectrum once every 2 seconds over the entire energy range

from 10 eV to 30 keV. With each measurement telemetered as an 8-bit logarithmically compressed word, approximately 15 kbits/sec would normally be needed to readout the experiment plus the telemetry needed to readout the correlator results. To fit the data within the ~ 2.6 kbit/sec telemetry rate, a microprocessor selects a portion of the data. Ten different preset modes have been established for the experiment, representing different mixes of electron, ion, and correlator data.

The experiment receives, as a direct input, information on the orientation of the angular fan being sampled relative to the in situ magnetic field. This information sets the measurement sequence for several of the modes. For example, the magnetometer data establish which two 8° zones within each satellite spin contain the atmospheric loss cone. Within these zones, 30-point spectra are recorded in eight 1° zones to image the loss cone. In addition to the preset modes stored in Read Only Memory in the experiment, the satellite can be programmed from the ground after satellite launch to set up any other measurement sequence desired. Each measurement sequence is repeated each half spin of the satellite.

4. FUNCTION BLOCK DIAGRAM

The function block diagram for the Low Energy Plasma Analyzer is shown in Figure 20. The experiment has two separate 260° sensors, one to measure electrons and one to measure ions. Each sensor has an independent programmable sweep voltage supply to set the plate voltages. The stepping and dwell times of the voltages are controlled through a sweep clock from the data processing unit (DPU). The bias voltages for the microchannel plates are provided by a second set of power supplies. The bias voltage can be set at any one of 14 levels spanning the normal operating range of the microchannel plate. This capability permits on-orbit compensation for any decrease in microchannel plate gain.

The discrete anode array divides the 128° azimuthal detection fan for each sensor into sixteen 8° zones. The outputs of each 8° zone are fed to one of 16 coarse zone preamplifiers. The number of amplified pulses occurring in an accumulation time is determined in a series of hybridized, addressable, quad, 8-bit counters. In addition, each 8° zone is subdivided into eight 1° segments. The counts in any set of eight 1° elements are measured by determining coincidence between the outputs of the eight fine zone amplifiers and the demultiplexed pulses from any one of the 16 coarse zone preamplifiers. As for the 8° zones, the numbers of coincidences occurring in an accumulation time are determined by hybridized, addressable, quad, 8 bit counters.

The 32 outputs of the coarse zone preamplifiers are provided in parallel to

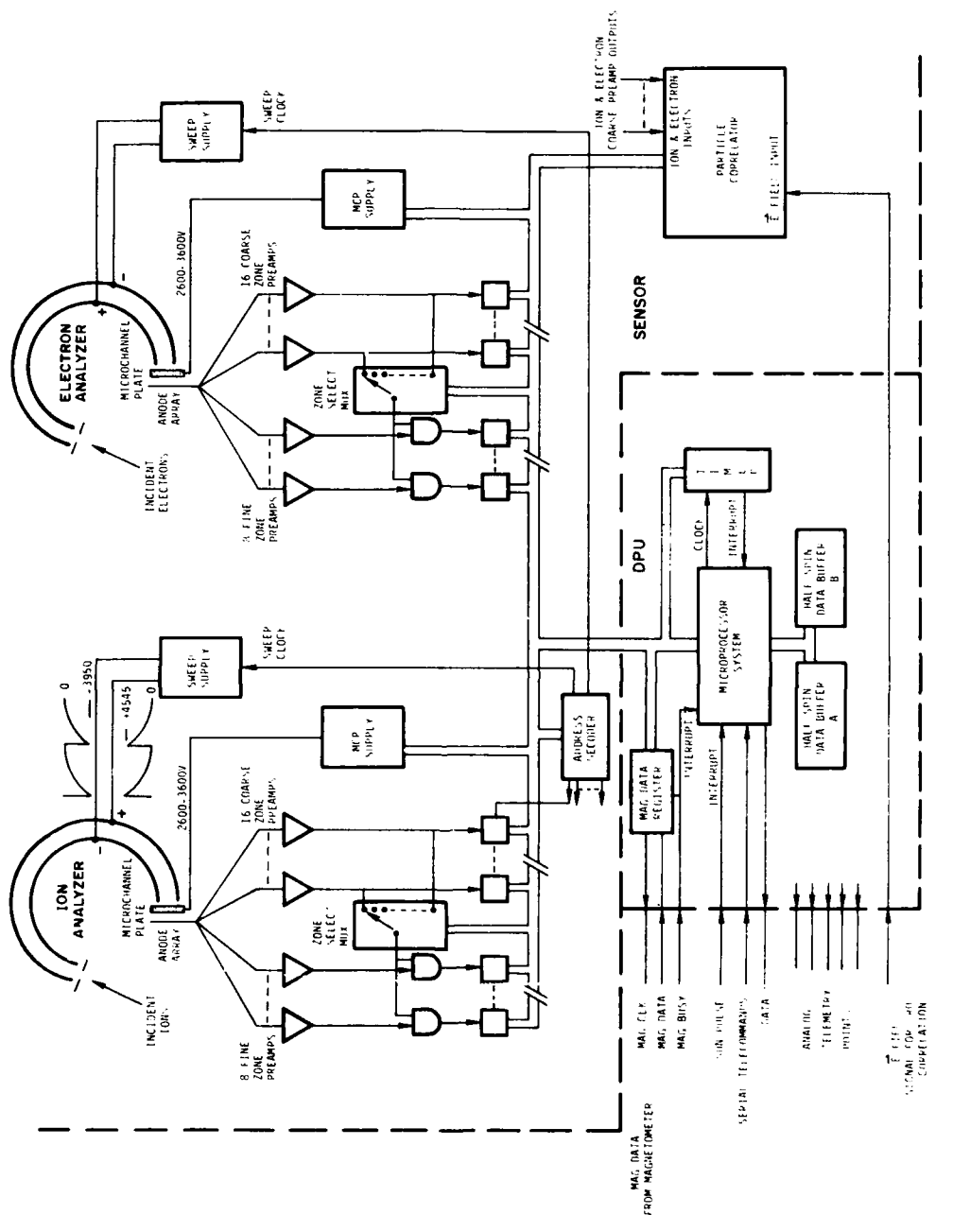


Figure 20. Function Block Diagram for Low Energy Plasma Analyzer

the particle correlator. The particle correlator uses a high frequency clock to time the arrival of each pulse and a SA3000 microprocessor to perform an auto-correlation on the pulse timing data. In addition, the ac signal from the electric field experiment is fed to the DPU and routed within LEPA to the correlator. The high frequency clock is used to time the zero crossings of the wave form. The microprocessor cross-correlates these data with pulse timing data.

The DPU reads out the data from the sensor unit and the particle correlator counters over an 8-bit parallel bus. The DPU uses an SA3000 microprocessor operating with interrupt-driven software. The five interrupts are: (1) The magnetometer interrupt, which determines when the atmospheric loss cone is within the detection fan of the analyzer, using magnetic field data provided directly from the on-board magnetometer; (2) The sun pulse interrupt, which initiates software to determine the satellite spin rate; (3) The timer interrupt, which initiates software controlling the stepping of the sweep voltage power supply and the reading of the data from the counter; (4) An interrupt provided over the serial telecommand line that causes the DPU to transfer data into the telemetry stream; and (5) A second interrupt provided over the serial telecommand line that indicates whether the DPU is to receive commands or new programming.

For each operating mode, the data for a half spin are stored in an 8 kbyte buffer in a fixed blocked pattern. Each buffer is filled, and the data are transferred into the telemetry stream approximately one half spin after accumulation.

References

1. Heikkila, W.J., Smith, J.B., Jarstrup, J., and Winningham, J.D. (1970) The soft particle spectrometer in the ISIS-I satellite, Rev. Sci. Instr. 41:1393.
2. McIlwain, C. (1971) UCSD Experiments and Operations Manual for the Environmental Measurements Experiment on the Applications Technology Satellite Mission ATS-F, Westinghouse Defense and Space Center Document 710667, pp. 4-109.
3. Hardy, D.A., Gussenhoven, M.S., and Huber, A. (1979) The Precipitating Electron Detectors (SSJ/3) for the Block 5D/Flights 2-5 DMSP Satellites: Calibration and Data Presentation, AFGL-TR-79-0210, AD A083136.
4. Vampola, A.L., and Kuch, G.A. (1978) Induced precipitation of the inner zone electrons: 1. Observations, J. Geophys. Res. 83:2543.
5. Winningham, J.D., Burch, J. ., Eakers, N., Blevins, V.A., and Hoffman, R.A. (1981) The low altitude plasma instrument (LAPI), Space Sci. Instrumentation 5:465.

6. Burch, J.L., Winningham, J.D., Blevins, V.A., Eakers, N., Gibson, W.C., and Hoffman, R.A. (1981) High-altitude plasma instrument for Dynamics Explorer-A, Space Sci. Instrumentation 5:455.
7. Frank, L.A., Yeager, D.M., Owens, H.D., Ackerson, K.L., and English, M.R. (1978) Quadrapspherical LEPEDEAS for ISEE's 1 and 2 plasma experiments, IEEE Trans. Geosci. Electronics GE-16:221.
8. Bame, S.J., Asbridge, J.R., Felthauser, H.E., Glare, J.P., Paschmann, T., Hemmerick, P., Lebmann, K., and Rosenbauer, H. (1978) ISEE-1 and ISEE-2 fast plasma experiments and the ISEE-3 solar wind experiment, IEEE Trans. Geosci. Electronics, GE-16:216.
9. Coates, A.J., Johnstone, A.D., Kellock, S.J., Smith, M.F., Bookes, T., and Winningham, S.D. (1984) A Space-Borne Plasma Analysis for Three-Dimensional Measurements of the Velocity Distribution. Submitted to IEEE 1984 Nucl. Sci. Sympos., Fla.

Contents

1. Scientific Objectives	77
2. Application	78
3. Measuring Techniques for Sensor B: Electron-Proton-Angle Spectrometer (EPAS)	79
4. Function Block Diagram for Sensor B	81
5. Measuring Techniques for Sensor A: Medium Electrons	83

8. The Medium Energy Electron and Proton Spectrometers (AFGL-701-5)

by

Axel Korth
Max Planck Institut fur Aeronomie
Kaltenburg, Lindau 3, West Germany

S. Ullaland
University of Bergen
Bergen, Norway

A. Vampola
Aerospace Corporation
Los Angeles, CA 90009

I. SCIENTIFIC OBJECTIVES

The Medium Energy Electron Spectrometer consists of two sensors: Sensor A (Medium Electrons) measures electrons with energies of order of magnitude 10^2 - 10^3 keV, and Sensor B (Electron-Proton-Angle-Spectrometer) measures electrons with energies of order of magnitude 10^1 - 10^2 keV, and protons of energies 10^1 - 10^3 keV. Because of its lower energy range, Sensor B will be described before Sensor A.

The Electron-Proton-Angle Spectrometer (EPAS), or Sensor B, measures protons and electrons with emphasis on wide pitch angle coverage with good pitch angle resolution. The viewing angles and apertures of the instrument achieve electron pitch angle coverage between 0° and 120° with respect to the spacecraft axis. Protons are measured in four directions (Figure 21). The combination of a

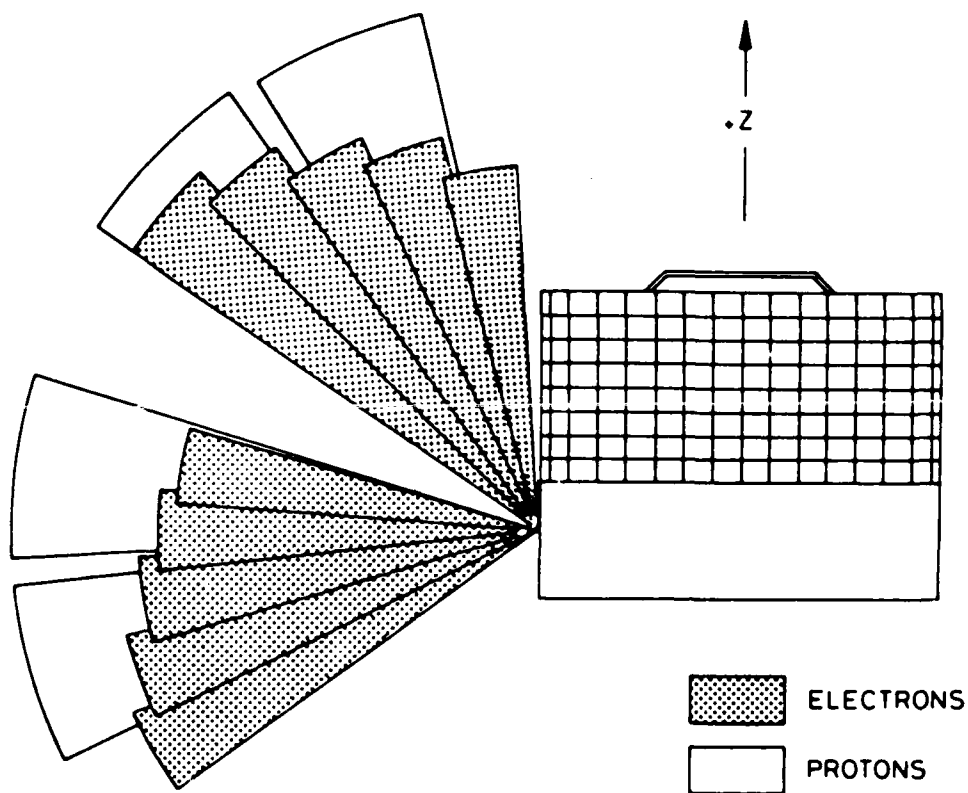


Figure 21. Schematic of Collimator and Magnetic Shielding Can for Electron-Proton-Angle Spectrometer

special magnetic deflection system and solid state particle detection technique makes possible simultaneous measurements for different pitch angles.

Protons are measured in the energy range 20 keV-2 MeV, and electrons, in the range 20 keV-300 keV. The lower energy thresholds will be made as low as is technically feasible for solid state detectors to ensure reasonable energy overlap with the Low Energy Plasma Analyzer (AFGL-701-6). The parameters to be determined by the EPAS instrument are temporal, spectral, and directional variations of the electron and proton fluxes.

2. APPLICATION

Since energetic particles gradient drift in the magnetosphere on fairly short time scales (~one-half hour), they can provide information on the general state

of the magnetosphere. For example, as the geomagnetic tail is stressed prior to a substorm, the pitch angle distributions of energetic electrons are modified, presumably by the drift shell-splitting effect. To investigate this kind of process, good three-dimensional particle distributions must be measured. Boundaries defined by spatial gradients can also be sensed remotely by such an instrument.

From magnetospheric observations of energy spectra and ionic composition, one can infer the sources of the plasma and energetic particles. Identification of the plasma source, whether solar or ionospheric, then suggests the mechanism of access to the magnetosphere. Particles of solar origin enter the magnetosphere at regions of weak B (that is, at the polar cleft and at the equatorial flanks of the tail), participate in the large-scale convective motions of the magnetosphere, and are soon found in the various tail and dayside boundary layers. Ultimately, they may be injected into the central magnetosphere by substorm-associated processes. During such disturbed intervals, we would attempt to identify those acceleration and transport processes that explain the adiabatic and nonadiabatic changes in the particles reaching the spacecraft.

Critical to the coupling of the magnetosphere with the ionosphere are the interactions of particles with waves. The waves are needed to scatter field-aligned ionospheric particles into trapped orbits. Conversely, waves also act to precipitate particles into the ionosphere. We will examine the effect of different plasma waves on particle precipitation. We will also study the effects of ion-cyclotron waves on protons and heavier ions.

3. MEASURING TECHNIQUES FOR SENSOR B: ELECTRON-PROTON-ANGLE SPECTROMETER (EPAS)

Basically, the EPAS instrument consists of a collimator and a magnetic shielding can that houses the magnet pole pieces, yoke, support structure, and the detectors (Figure 22). Particles entering the spectrometer encounter a homogeneous magnetic field of ~ 0.08 T, which separates protons and heavier ions from electrons. The magnetic field geometry was designed so that a parallel beam of electrons entering the instrument at a fixed angle with respect to the axis of the aperture is deflected by $\sim 180^\circ$ and focused to a single point irrespective of its energy. The focusing can be achieved for electron energies between 15 and 300 keV. The deflection system defines a focal curve where each point corresponds to a given angle of incidence to the spectrometer. Along this focal curve, five rectangular solid state detectors are mounted that define five angular intervals within the 60° aperture of the unit. The electron energy is determined from

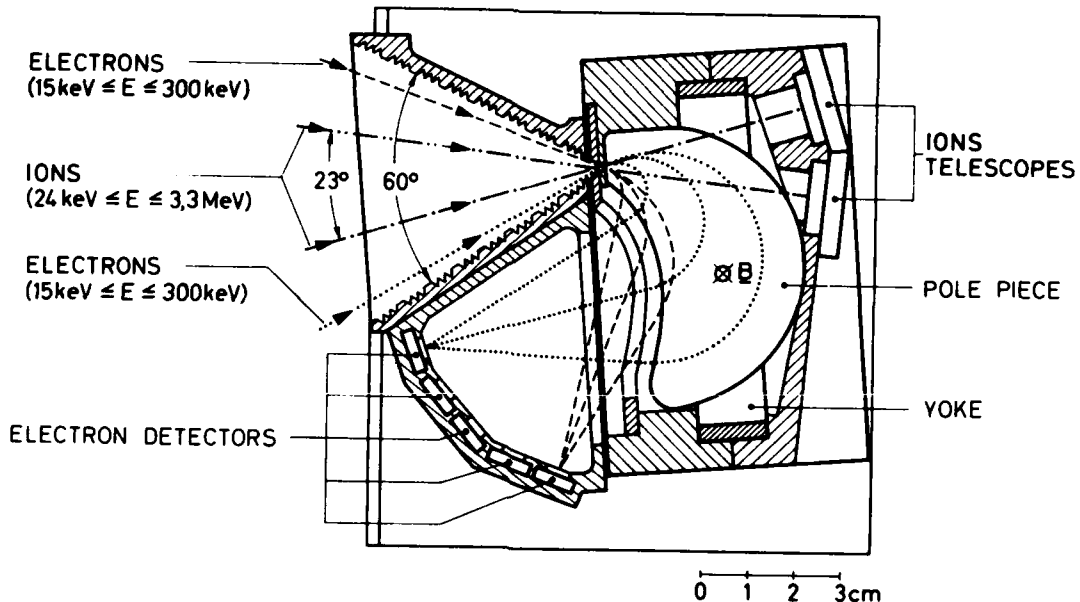


Figure 22. Schematic of the Magnetic Deflection System and Detectors in the Electron-Proton-Angle Spectrometer

pulse height analysis for each detector. The energy range of ~ 15 to 300 keV is divided into 15 approximately logarithmically spaced energy channels.

The deflection of protons and heavy ions with energies above 20 keV is small. They propagate on almost straight lines and are detected in two solid state detector telescopes. Figure 22 shows the arrangement of two telescopes behind the magnetic deflection system. Each telescope consists of a front and a back solid state detector. The front detector is used for energy analysis; the back detectors define the angular acceptance of the telescope and provide a veto signal to reject penetrating particles. The upper energy range of the telescope is determined by the thickness of the front detector, here 100μ thick, and thus covers the energy range up to 3300 keV for protons. The energy range of 20 to 3300 keV is divided into 12 approximately logarithmically spaced energy channels. However, no identification of the different ion species is possible. The front detector of the telescope is operated with the aluminum contact facing the environment. Although the aluminum contact is somewhat thicker than the gold one, giving a slightly higher penetration threshold, the detector lifetime against radiation damage is thereby increased by two or more orders of magnitude in total ion exposure.

The EPAS instrument contains two such sensor units with a resulting angular coverage of 120° for electrons and four different angular intervals for the ions

(see Figure 21). Table 11 presents a summary of the energy range, energy channels, look directions of the detectors, angular resolution, and geometric factors.

4. FUNCTION BLOCK DIAGRAM FOR SENSOR B

The function block diagram of the analog part of the EPAS instrument is shown in Figure 23. All particle detectors (ions: P 0 to P 3; electrons: E 0 to E 9) are followed by charge sensitive preamplifiers, pulse amplifiers, pulse formers, and discriminators.

The proton telescopes produce three different sets of data: the count rates of the front detectors (P 0 to P 3), the count rates of the back detectors (U 0 to U 3), and coincidence counts of the front and back detectors. The count rates of the front detectors go to a "Proton Selector" unit that selects one of the four for energy analysis in the proton pulse height analyzer (PHA). This analysis is only carried out if a coincidence between front and back detectors has not occurred. These data are called differential count rates.

Simultaneously, the count rates of the four front detectors are routed via discriminators to the data processing unit (DPU); these are called integral count rates.

The data lines from the 10 electron detectors (E 0 to E 9) pass the "Electron Selector," which determines the electron detector on which channel energy analysis is carried out in the "Electron PHA." The 10 data lines are also routed via discriminators as integral count rates directly to the DPU.

The proton and electron PHA sort the count rates from one selected proton and electron detector into 12 and 15 different energy intervals, respectively.

An in-flight test generator (IFC) supervises the instrument. Pulses with varying amplitudes are fed into the inputs of the charge-sensitive amplifiers and are counted not only at the outputs of the two PHAs, but also at the outputs of the discriminators. The in-flight calibrator is initiated via the IFC ON line and controlled by the frequency on the IFC clock.

The DPU will provide 16 scalers to monitor the integral counting rates from the 10 electron detectors, 4 proton front detectors, and coincidence and back detector counting rates of the proton detector selected for pulse height analysis. Two scalers in the DPU will be driven by two sets of 4-bit address and single strobe lines, one each for the proton and electron detector selected for pulse height analysis.

The DPU will contain power supplies to provide power with various voltages to the sensor.

Table 11. Electron-Proton-Angle Spectrometer Specifications

	Electrons			Ions	
Energy range	16 - 300 keV			20 - 3300 keV	
Energy channels integral	> 22			> 27	
differential	16 - 23			20 - 27	
"	23 - 30			27 - 35	
"	30 - 37			35 - 45	
"	37 - 44			45 - 59	
"	44 - 52			59 - 75	
"	52 - 60			75 - 98	
"	60 - 70			98 - 130	
"	70 - 83			130 - 169	
"	83 - 96			169 - 226	
"	96 - 114			226 - 301	
"	114 - 133			301 - 403	
"	133 - 154			403 - 3300	
"	154 - 180				
"	180 - 214				
"	214 - 300				
Look directions of detectors with respect to the spin axis	10°	20°	30°	23°	46°
	40°	50°	80°	83°	106°
	90°	100°	110°		
	120°				
Angular resolutions in elevation	±3°			±5°	
in azimuth	±2°			±2°	
Geometric factor	$5 \times 10^{-5} \text{ cm}^2 \text{ sr}$			$2 \times 10^{-4} \text{ cm}^2 \text{ sr}$	

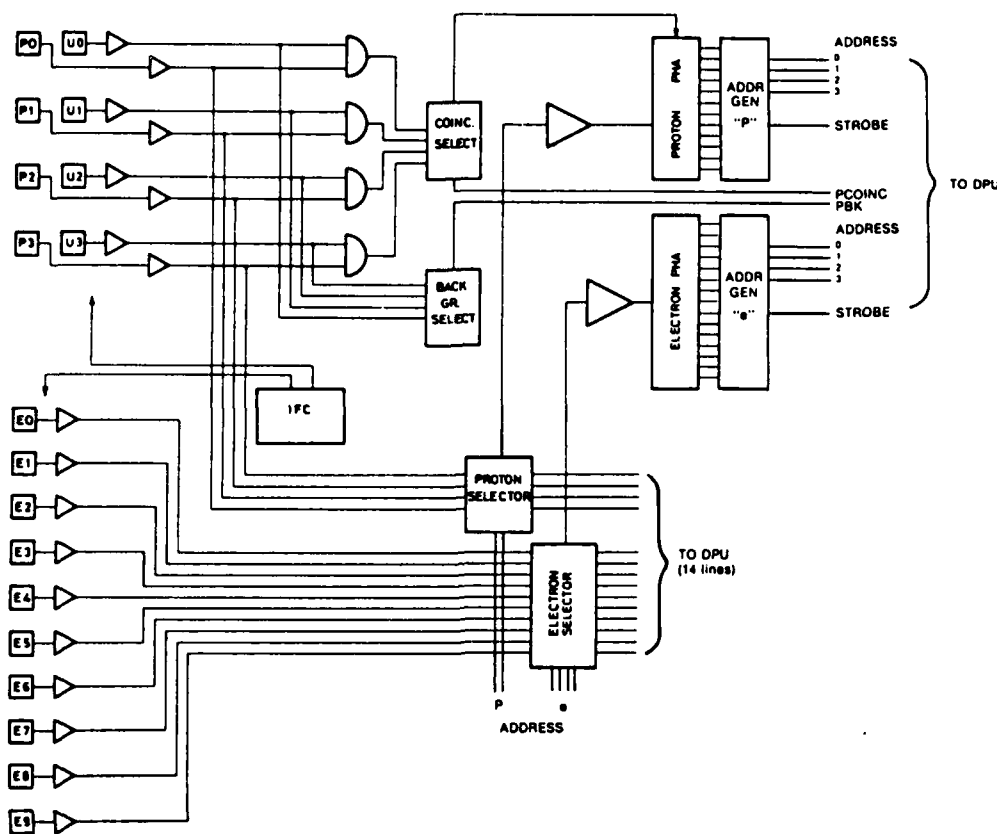


Figure 23. Function Block Diagram for the Electron-Proton-Angle Spectrometer

5. MEASURING TECHNIQUES FOR SENSOR A: MEDIUM ELECTRONS

Sensor A uses a uniform magnetic field of 850 G to momentum analyze electrons incident through an aperture. The electrons experience a $V \times B$ force that constrains them to circular, or helical, paths within the instrument. An array of lithium-drifted silicon detectors at the 180° primary focus detects them. (The 180° focusing principle, which relies on the fact that chords subtending angles near 180° do not differ much in length from a diameter of a circle, does not affect the motion parallel to the magnetic field; hence, the focusing is effective in only one plane.) Momentum analysis is achieved because the radius of the circle is proportional to the momentum of the charged particle. Electrons with similar momenta (or energies) that enter the aperture at various angles are focused into a vertical bar with the approximate width of the entrance aperture. At this focal plane, there are 18 detectors. One is covered and measures penetrating particles,

such as cosmic rays. The other 17 detectors separate the energy range of the instrument into 17 different energy channels. A schematic diagram, without the external collimator, is shown in Figure 24 to illustrate the analyzing chamber. Internal baffling acts as a disc-loaded collimator to reduce scattering within the instrument.

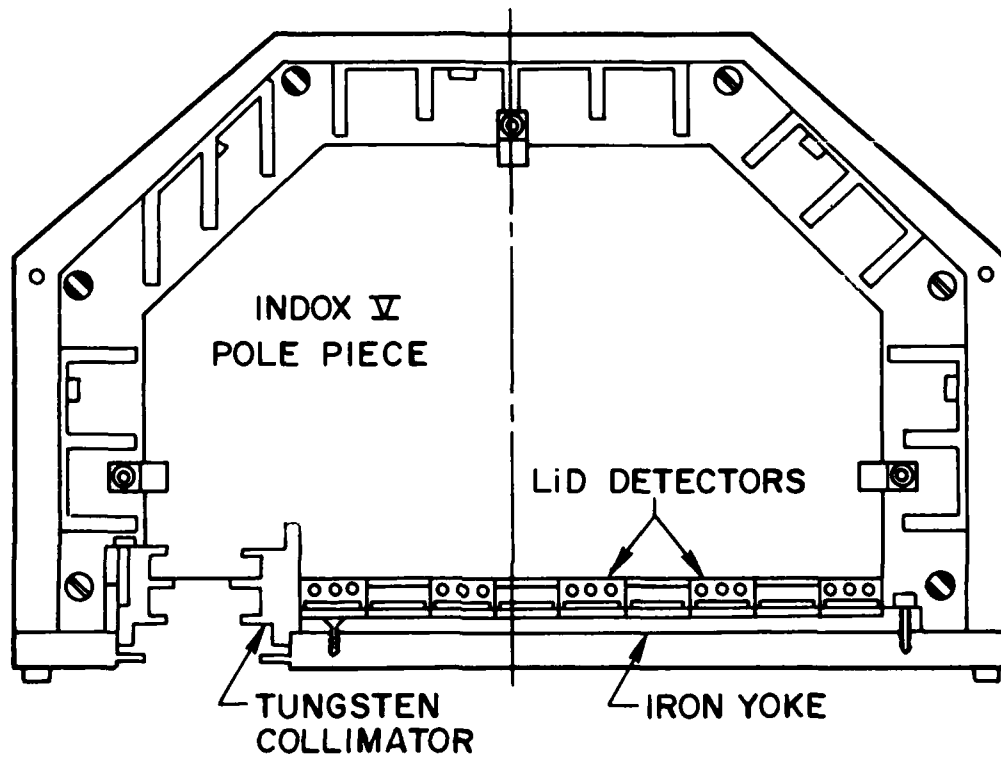


Figure 24. Schematic Diagram of the Analyzing Chamber of the Medium Electron Sensor

Since the momentum (and hence, the energy) of the electron incident on a detector is known from geometric considerations, the information available from the energy deposit in the detector can discriminate against various types of background effects, such as bremsstrahlung, cosmic rays, penetrating protons, etc. The result is a "clean" measurement of electron fluxes, even with backgrounds that negate the use of sensors that attempt to identify electrons only by their energy deposit and another parameter such as dE/dX .

Internal and external disc-loaded collimators limit the acceptance angle to $\pm 11^\circ$ in the horizontal direction and from $\pm 11^\circ$ to $\pm 3^\circ$ in the vertical direction.

The vertical angle is energy-dependent; it is smaller for higher energies. The look direction of the aperture is normal to the spin axis of the vehicle, with the horizontal axis of the collimator parallel to the spin axis.

Figure 25 shows the electronic logic utilized for each channel. The signal from the detector is amplified, using a charge-coupled preamplifier, and then

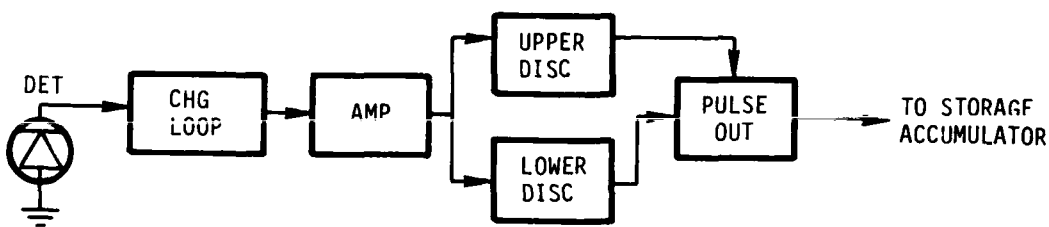


Figure 25. Electronic Logic for Each Channel in the Medium Electron Sensor

processed by a two-level discriminator. The lower level is set at 50 percent of the minimum energy electron that can be focused upon the detector after passing through the collimator. Energy deposits below this amount result from bremsstrahlung or electrons that have been scattered within the analyzing chamber (including scattering out of another detector). The 50-percent level permits the channel to count electrons that have an anomalously high loss of energy in the detector as escaping X rays and bremsstrahlung, or electrons that scatter back out of the detector without losing all of their energy.

The upper level discriminator is set at 110 percent of the maximum analyzed electron energy on the detector. (The extra 10 percent allows efficient counting of maximum energy electrons even if the detector becomes degraded in orbit.) Energy deposits above this upper level are usually caused by very energetic protons, or cosmic rays, that penetrate the walls of the chamber and pass through the detector. Minimum proton energy for penetration of the chamber is 120 MeV for the minimum path length. Most paths are much longer.

The energy range and geometric-energy factor for each of the channels are shown in Table 12.

The instrument is 27.5 cm by 7.5 cm high, weighs 7.5 kg, and uses 0.9 W of power at 28 V.

Table 12. Medium Energy Electron Spectrometer Energy Ranges and Geometric-Energy Factors

Channel	E_{\min} (keV)	E_{\max} (keV)	GEF(cm^2 -ster-keV)
1	46.8	107	4.74
2	120	199	5.50
3	216	308	5.67
4	326	427	5.56
5	446	552	5.32
6	573	682	5.01
7	703	816	4.54
8	838	952	4.10
9	974	1090	3.74
10	1110	1230	3.43
11	1250	1370	3.17
12	1390	1510	2.94
13	1530	1650	2.74
14	1680	1790	2.57
15	1820	1940	2.41
16	1960	2080	2.27
17	2100	2220	2.15

Contents

1. Scientific Objectives	87
2. Application	88
3. Measuring Techniques	89
4. Function Block Diagram	91
Acknowledgments	94
References	94

9. The Spectrometer for Electrons and Protons (ONR-307-3)

by

J.B. Reagan, E.E. Gaines, S.J. Battel,
D.A. Simpson, W.L. Imhof, and R.R. Vondrak
Lockheed Palo Alto Research Laboratory
Palo Alto, CA 94304

1. SCIENTIFIC OBJECTIVES

The ONR-307-3 Spectrometer for Electrons and Protons (SEP) measures with fine pitch-angle resolution the flux of energetic electrons in the energy range of 20-5000 keV and the flux of energetic protons in the energy range 500 keV-100 MeV. The ONR-307-3 SEP consists of three identical particle telescopes composed of surface-barrier silicon detectors with active anticoincidence shielding and narrow collimation (3° FWHM). The energy spectra are measured with fine energy resolution: 24 contiguous channels for the electrons, and 48 contiguous channels for protons. The three particle telescopes are mounted at optimum angles to the CRRES spin axis to provide nearly complete pitch-angle coverage on each spacecraft spin.

The SEP is one component of the ONR-307 Energetic Particles and Ion Composition (EPIC) Experiment. The other EPIC instruments are the ONR-307-8-1,

ONR-307-8-2 Low Energy Ion Mass Spectrometers that measure primarily the ion composition between 0.1 and 32 keV/q,¹ and the ONR-307-8-3 Medium Energy Ion Mass Spectrometer that measures the ion composition between 20 and 8000 keV-AMU/q.²

The overall objective of the ONR-307-3 experiment is to obtain necessary data to construct predictive models, suitable for engineering purposes, of the energetic particle and plasma environment in those regions of space of primary interest to the DOD satellite operations. The specific science objectives of this experiment are:

- (1) To measure the intensity, energy spectra, and pitch angle distribution of energetic electrons and protons continuously as a function of time. These measurements will characterize the dynamical behavior of the radiation belts.
- (2) To compute accurately the total omnidirectional flux at the satellite position.
- (3) To understand the physics of the sources, energization, transport, lifetimes, and losses of energetic particles in the Earth's radiation belts.
- (4) To understand the details of wave-particle interactions (WPI), both natural and manmade, that are a principal loss mechanism for radiation belt particles. These WPI produce particle precipitation into the ionosphere that can disrupt radio-wave communications of vital interest to the U.S. Navy.
- (5) To utilize this experimental data base to greatly improve the accuracy of the trapped radiation belt models and to characterize model particle precipitation.

2. APPLICATION

The ONR-307-3 SEP Experiment will measure continuously the complete energy and angular distribution of the energetic electrons and protons. This measurement of the complete distribution of the trapped energetic particle population with fine angular resolution is necessary to:

(a) "Remote sense" the omnidirectional flux far away from the satellite orbit plane by directly unfolding the measured in situ pitch angle distribution to derive the pitch angle distribution at all lower altitudes. A measurement of the complete pitch angle distribution at the CRRES satellite enables the experimenter, through adiabatic transformation of the particle bounce motion, to define the particle popu-

-
1. Quinn, J. M., Shelley, F.G., Battel, S.J., Hertzberg, F., Roselle, S., and Saunders, T.C. (1985) The Low Energy Ion Mass Spectrometer (ONR-307-8-1, ONR-307-8-2), AFGL-TR-85-0017 (this volume).
 2. Voss, H.D., Shelley, F.G., Ghielmetti, A.G., Hertzberg, F., Battel, S.J., Appert, K.L., and Vondrak, R.R. (1985) The Medium Energy Ion Mass Spectrometer (IMS-HI) (ONR-307-8-3), AFGL-TR-85-0017 (this volume).

lation on the field line below the satellite. Such measurements are absolutely essential to the mapping of the radiation belts to all altitudes.

(b) Investigate the narrow "source/loss cone" regions of the pitch angle distribution that are the primary sources and the major sinks of radiation belt particles. The pitch angle diffusion of particles into the atmospheric loss cone is one of the principal mechanisms for radiation belt depletion. Understanding the pitch angle diffusion rates into the loss cone caused by natural and manmade waves is central to modeling the dynamic behavior of the radiation belts.

The ONR-307-3 instrument can accomplish these objectives because it has comprehensive pitch angle measurements with fine angular resolution (3° FWHM). The arrangement of the three identical telescopes, combined with the spin of the spacecraft, will provide nearly complete measurement of the particle distribution function for all orientations of the spin axis to the magnetic field.

High temporal resolution measurements (0.25 sec) will enable the study of source/loss cone transient mechanisms, substorm injections, and L-shell splitting. A 12-channel energy spectrum is obtained every 0.25 sec. The pitch angle distribution from 0 to 90° over 12 energy channels is obtained every 7.5 sec at a spin rate of 2 rpm. Complete angular distribution functions over the entire energy range for both electrons (24 energy channels) and protons (48 energy channels) can be obtained in about 3 min.

3. MEASURING TECHNIQUES

The ONR-307-3 instrument is based heavily on the successful SC-3 spectrometer on the SCATHA mission and consists of a series of solid-state particle spectrometers, each with four detector elements. The SC-3 instrument was described in detail by Reagan et al.³ and by Stevens and Vampola.⁴ The configuration of each spectrometer is shown in Figure 26. Various logic combinations of the four detector elements in the spectrometer determine the particle types and energy ranges that are measured in several command-selectable, time-multiplexed modes of operation.

The D-detector, 200- μm thick intrinsic SI, measures both the rate of energy loss of the higher energy particles, and directly stops and measures the lower en-

-
3. Reagan, J.B., Nightingale, R.W., Gaines, E.E., Imhof, W.L., and Stassino-poulos, E.G. (1981) Outer zone energetic electron spectral measurements, *J. Spacecraft and Rockets* 18:83-88.
 4. Stevens, J.R., and Vampola, A.L. (1978) *Description of the Space Test Program P78-2 Spacecraft and Payloads*, Space and Missile Systems Organization, Air Force Systems Command, TR-78-24.

AD-A160 584 CRRES/SPACERAD (COMBINED RELEASE AND RADIATION EFFECTS 2/2
SATELLITE/SPACE RA (U) AIR FORCE GEOPHYSICS LAB
HANSOM AFB MA M S GUSSENHOVEN ET AL 24 JAN 85

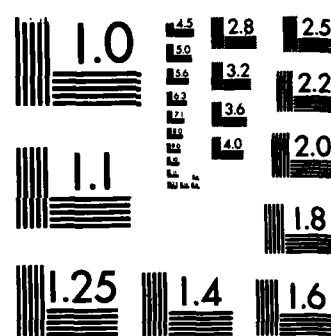
UNCLASSIFIED

AFGL-TR-85-0017

F/G 22/1

NL

END
THERES
DATA



MICROCOPY RESOLUTION TEST CHART
NATIONAL BUREAU OF STANDARDS-1963-A

ergy particles. The E-detector, a stack of five 2-mm-thick detectors in parallel, is located behind the D-detector to stop the higher energy particles and to measure their total energy loss. The E'-detector, 1000 μ m thick, is located behind the E-detector and is used as an active collimator. Behind the E'-detector is a tungsten absorber that sets the upper energy limit for analysis.

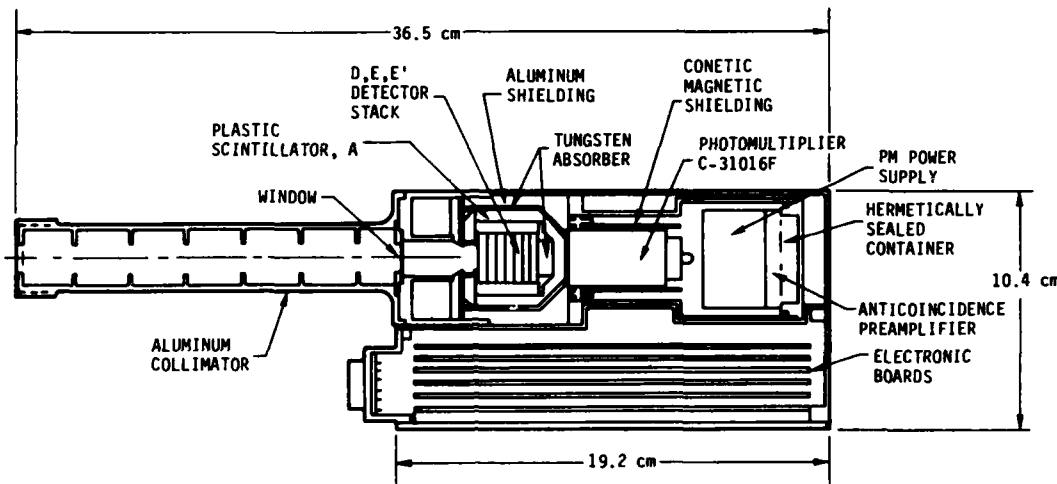


Figure 26. Cross-Section View of the SCATHA SC-3 Energetic Electron/Proton Spectrometer Showing the Various Sensor Elements and the Long Collimator

All of these detectors are fabricated of surface-barrier silicon and are stacked together in a telescope configuration. The entire stack is surrounded by the A-anticoincidence detector, a plastic scintillator viewed by a photomultiplier tube. The A-detector senses and rejects energetic particles and bremsstrahlung that penetrate either the outer shielding walls of aluminum and tungsten or the silicon detector stack and absorber. The detector stack is located behind a long, narrow collimator that defines the 3° angular field-of-view (FWHM). The instrument geometric factor is approximately $3 \times 10^{-3} \text{ cm}^2\text{-ster.}^3$.

Three spectrometers are oriented at angles of 80°, 60°, and 40° to the CRRES spin axis. These three spectrometers comprise the ONR-307-3-1 Sensor Package (SP) shown in Figure 27. The instrument analyzer electronics are mounted near the SP in the ONR-307-3-2 Analyzer Package (AP); both units are mounted on the

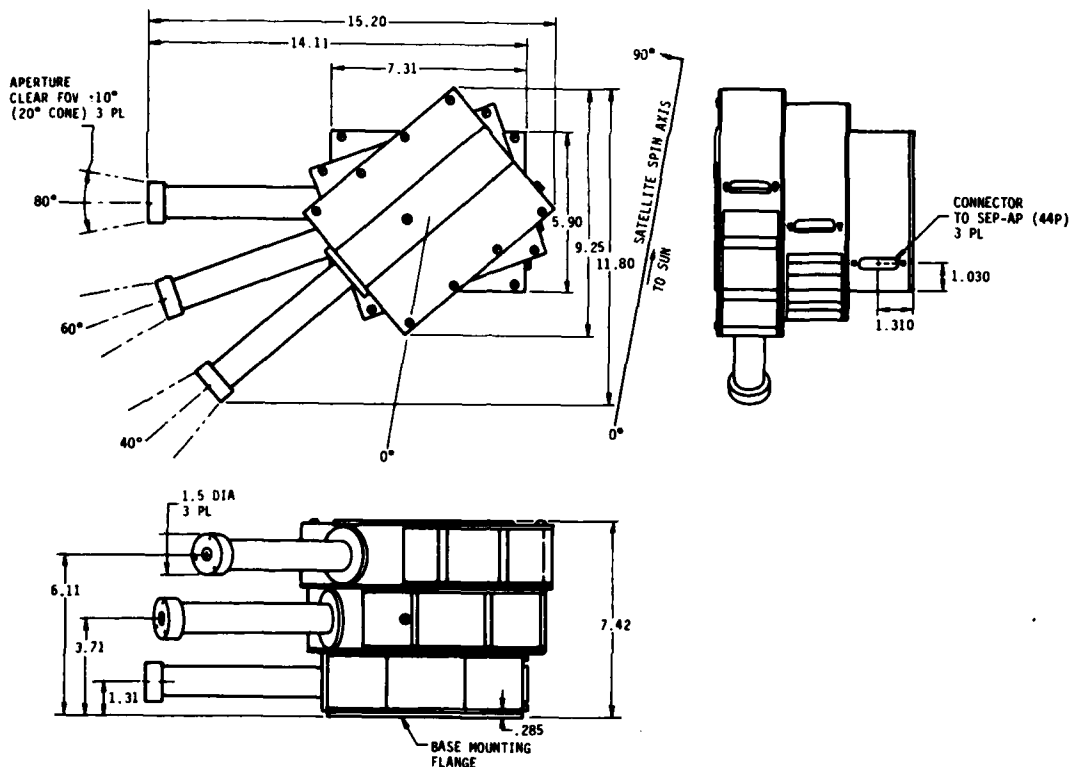


Figure 27. Mechanical Arrangement of the Three SEP Telescopes

bottom of the spacecraft. The AP and SP are separated to achieve a lower temperature in the silicon detectors for improved low-energy electron detection.^{5, 6}

4. FUNCTION BLOCK DIAGRAM

A function block diagram of the ONR-307-3 instrument is shown in Figure 28. The instrument operates from a CMOS memory of 768 8-bit words that are individually addressable and loadable via a 16-bit serial-digital command. Twelve of these words (32-bit control register for each of the three sensors) completely

5. Voss, H.D., Reagan, J.B., Imhof, W.L., Murray, D.O., Simpson, D.A., Cauffman, D.P., and Bakke, J.C. (1982a) Low temperature characteristics of solid state detectors for energetic X-ray, ion and electron spectrometers, IEEE Trans. Nucl. Sci. NS-29:164.
6. Voss, H.D., Bakke, J.C., and Roselle, S.N. (1982b) A spacecraft multichannel analyzer for a multidetector solid state detector array, IEEE Trans. Nucl. Sci. NS-29:173.

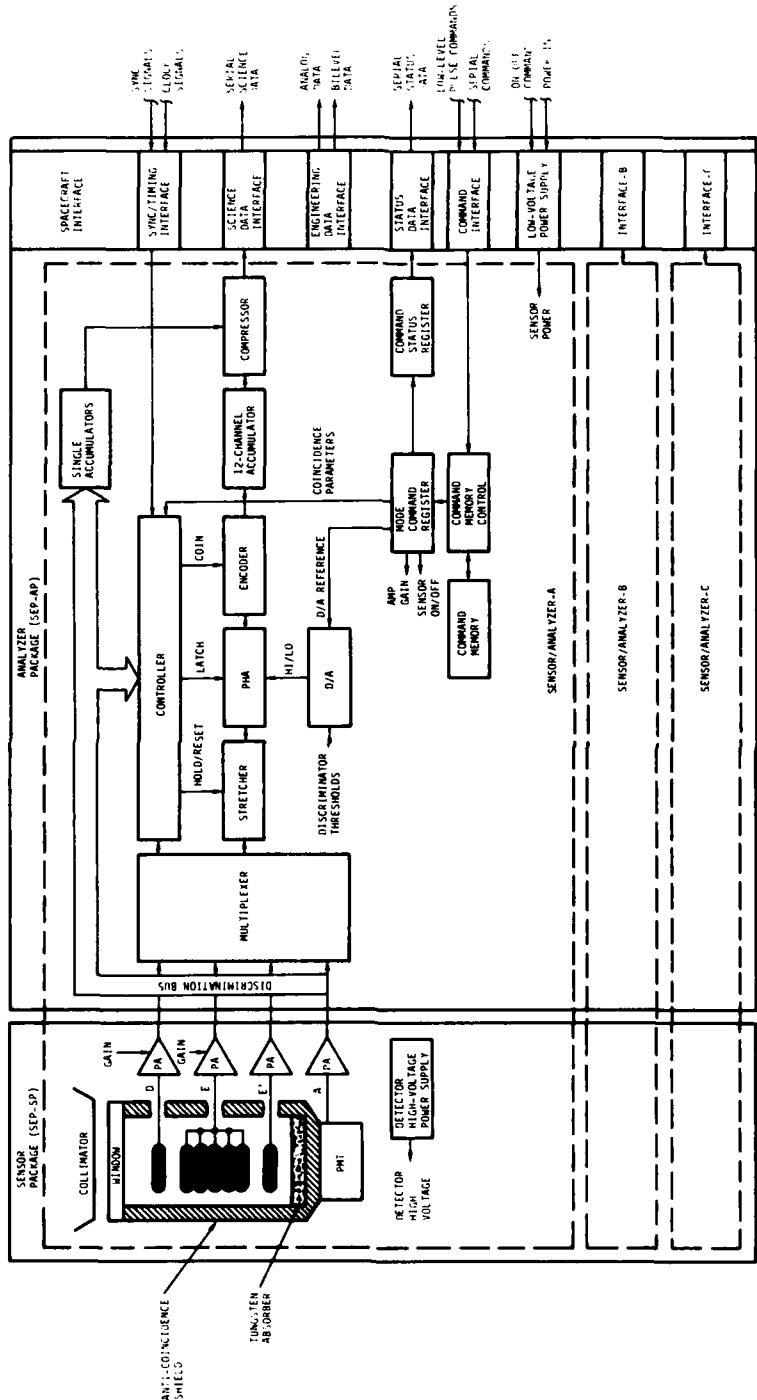


Figure 28. Function Block Diagram of the ONR-307-3 SEP Instrument

define one operating MODE of the instrument. A MODE is defined by specifying the logic conditions (coincidence/anticoincidence), gain, and energy thresholds required between the four detector elements (D, E, E', A) to uniquely establish a particle type and energy range for analysis. A choice of two amplifier gain settings for the D- and E-detectors is available. The lower and upper energy thresholds selected for analysis by the 12-channel pulse-height analyzer (PHA) are determined to 8- and 6-bit resolution, respectively. Either the D- or E-detector is selectable at any time for analysis by the PHA through the multiplexer. The energy threshold of the sensor not selected for analysis can be set to 8-bit resolution.

The operating modes can be structured to emphasize one particle type, such as electrons, or all particle types; to concentrate on special events, such as solar particle events; or to dwell on a narrow energy region of interest with any particle type. The commandable options are extensive, but an optimum operating configuration will be loaded initially and adjusted as conditions dictate. A hard-wired backup MODE can be selected if a major failure occurs in the memory operation. The hard-wired backup MODE measures the higher energy electrons (300-5100 keV) and is independent of the memory. The instrument operates in this condition automatically whenever the memory is being loaded or disabled.

The operating modes will be selected as required to optimize data collection in the inner and outer radiation belts. The basic programmable mode parameters are the energy range and energy channel widths for the electrons and for the protons. Typical modes that may be used during the CRRES mission are shown in Table 13.

Table 13. Spectrometer for Electrons and Protons: Typical Operating Modes

Species	Mode	Energy Range	Channel Width
Electrons	ELEC1	20-300 keV	20 keV
	ELEC2	300-5000 keV	400 keV
Protons	PROT1	0.5-4.5 MeV	330 keV
	PROT2	4.5-20 MeV	1.25 MeV
	PROT3	20-45 MeV	2.0 MeV
	PROT4	45-100 MeV	4.2 MeV

Acknowledgments

The authors wish to thank J.C. Bakke, L.A. Hooker, and V.F. Waltz for their efforts in the design, development, and fabrication of this instrument. We also deeply appreciate the assistance of our co-investigator, H.D. Voss.

This work was supported by the Office of Naval Research under contract N00014-83-C-0476 and by the Lockheed Independent Research Program.

References

1. Quinn, J.M., Shelley, E.G., Battel, S.J., Hertzberg, E., Roselle, S., and Saunders, T.C. (1984) The Low Energy Ion Mass Spectrometer (ONR-307-8-1, ONR-307-8-2), AFGL-TR-85-0017 (this volume).
2. Voss, H.D., Shelley, E.G., Ghielmetti, A.G., Hertzberg, E., Battel, S.J., Appert, K.L., and Vondrak, R.R. (1984) The Medium Energy Ion Mass Spectrometer (IMS-HI) (ONR-307-8-3), AFGL-TR-85-0017 (this volume).
3. Reagan, J.B., Nightingale, R.W., Gaines, E.E., Imhof, W.L., and Stassino-poulos, E.G. (1981) Outer zone energetic electron spectral measurements, J. Spacecraft and Rockets 18:83-88.
4. Stevens, J.R., and Vampola, A.L. (1978) Description of the Space Test Program P78-2 Spacecraft and Payloads, Space and Missile Systems Organization, Air Force Systems Command, TR-78-24.

5. Voss, H.D., Reagan, J.B., Imhof, W.L., Murray, D.O., Simpson, D.A., Cauffman, D.P., and Bakke, J.C. (1982a) Low temperature characteristics of solid state detectors for energetic X-ray, ion and electron spectrometers. IEEE Trans. Nucl. Sci. NS-29:164.
6. Voss, H.D., Bakke, J.C., and Roselle, S.N. (1982b) A spacecraft multichannel analyzer for a multidetector solid state detector array. IEEE Trans. Nucl. Sci. NS-29:173.

Contents

1. Scientific Objectives	97
2. Application	97
3. Measuring Techniques	99
4. Function Block Diagram	105
References	108

10. The Proton Telescope (AFGL-701-8, AFGL-701-9)

by

Kevin Riehl and D.A. Hardy
Air Force Geophysics Laboratory
Hanscom AFB, MA 01731

Ed Boughan
Center for Space Research
Massachusetts Institute of Technology
Cambridge, MA 02139

1. SCIENTIFIC OBJECTIVES

The objective of the Proton Telescope (PROTEL) is to make well calibrated, high resolution measurements of 1-100 MeV protons. PROTEL consists of two sensor head assemblies and a data processing unit (DPU). The low energy sensor head measures 1-9 MeV protons in eight contiguous energy channels. The high energy sensor head measures 6-100 MeV protons in 16 contiguous energy channels. The entire 24 point spectrum is returned once per second. PROTEL will monitor the major energy contributors to the radiation belts for both static and dynamic radiation belt models.

2. APPLICATION

In the past ten years, very few proton measurements have been made in the

energy range of PROTEL (1-100 MeV) through the heart of the radiation belts. The present radiation belt models¹ are based largely on instruments flown in the 1960s. Many were poorly calibrated or flown only in a limited L-shell range, so there were gaps or questionable data points in the models.

More recently, high energy proton instruments have been flown at very low or very high altitudes. The DIAL satellite,² STP71-2,³ and STP72-1⁴ were polar orbiting satellites that entered the lower boundary of the proton inner radiation belt only over the South Atlantic Anomaly. The 1976-059A satellite^{5,6} was placed in geosynchronous orbit ($L = 6.6$). The S3-2 and S3-3 satellites were elliptical polar orbiting satellites,^{7,8} but the proton instruments experienced high background problems.

PROTEL is similar to instruments built by Lockheed,³ Los Alamos,⁶ TRW,⁹ and Panametrics.¹⁰ In PROTEL, we have attempted to incorporate the strengths

-
1. Vette, J.L., Teague, M.J., Sawyer, D.M., and Chan, K.W. (1979) Modeling of the earth's radiation belts, in Solar-Terrestrial Predictions Proceedings (Vol. 2), R.F. Donnelly, Ed., U.S. Dept. of Commerce, Washington, D.C.
 2. Fischer, H.M., Auschrat, V.W., Wibberenz, G. (1977) Angular distribution and energy spectra of protons of energy $5 < E < 50$ MeV at the lower edge of the radiation belt in equatorial latitudes, J. Geophys. Res. 82:537.
 3. Reagan, J.B., Bakke, J.C., Kilner, J.R., Matthews, J.D., and Imhof, W.L. (1972) A high-resolution multiple-particle spectrometer for the measurements of solar particle events, IEEE Trans. Nucl. Sci. NS-19:554.
 4. Filz, R.C., Katz, L., Sellers, B., Hanser, F.A., and Holeman, E. (1974) Observations of 5-45 MeV protons at $L \leq 3$ and $L \geq 7$, Space Res. 15:321-326.
 5. Belian, R.D., Baker, D.N., Higbie, P.R., and Hones, E.W., Jr. (1978) High-resolution energetic particle measurements at 6.6 RE. 2. High-energy proton drift echoes, J. Geophys. Res. 83:4857.
 6. Baker, D.N., Belian, R.D., Higbie, P.R., and Hones, E.W., Jr. (1979) High-energy magnetospheric protons and their dependence on geomagnetic and interplanetary conditions, J. Geophys. Res. 84:7138.
 7. Parsignault, D.R., Holeman, E., and Filz, R.C. (1981a) Solar cycle induced modulation of the 55-MeV proton fluxes at low altitudes, J. Geophys. Res. 86:11493.
 8. Parsignault, D.R., Holeman, E., and Filz, R.C. (1981b) Long-term intensity decrease in the 8- to 25-MeV proton fluxes at low L values, J. Geophys. Res. 86:11447.
 9. Baum, J.J., Harman, R.W., Maronde, R.G., and Hornbuckle, T.A. (1972) Design of the particles experiment subsystem of the Apollo Luna Subsatellite, IEEE Trans. Nucl. Sci. NS-19:673.
 10. Morel, P.R., Hanser, F.A., and Sellers, B. (1974) A Satellite Telescope for Protons and Alphas, Panametrics, Inc., Waltham, Mass., Final Report AFCRL-TR-74-0531, AD A003727.

of past instrumentation techniques. The fundamental detecting elements are solid state detectors. (For more information, see Brown et al.¹¹ and Knoll.¹²)

3. MEASURING TECHNIQUES

The two sensor heads are designed on basically the same principle (Figures 29a and 29b). Each has a collimator, a sweeping magnet, an entrance and exit aperture, a detector stack, and passive shielding. (There is also active shielding for the high energy head, HE, only.)

The collimator eliminates proton and electron fluxes outside of the acceptance cone. The half-angle opening of the collimator for the low energy sensor head is 9.6° (HE, 16.8°). Points of minimum thickness correspond to the range of orthogonally impinging 37 MeV (HE, 42 MeV) protons. When oblique trajectories are considered, however, this range energy increases dramatically; that is, few protons should make it to the detector stack penetrating through the collimator walls. The collimator is made of aluminum. The inside surface has a saw-toothed pattern to reduce the forward scattering of particles into the entrance aperture. This surface is also painted with conductive matte black paint to minimize light scattering toward the detectors.

The sweeping magnet sweeps away electron fluxes that would create a background to the proton data. The maximum field strength is approximately 5 kG which would sweep off 4 MeV (HE, 8 MeV) electrons in the sensor heads.

The entrance and exit apertures define the acceptance angle of 9.53° of the low energy sensor, and 16.70° of the HE (FWHM). The effective area of each aperture is 2.22 cm^2 (HE, 1.77 cm^2). Given their separation, the geometric factor of the low energy sensor head is $0.0121 \text{ cm}^2\text{-ster}$ (HE, $0.12 \text{ cm}^2\text{-ster}$). The entrance aperture is made of 0.744 cm (HE, 0.744 cm) aluminum, and 0.254 cm (HE, 0.687 cm) tungsten alloy.

At the heart of PROTEL are the detecting elements, the solid state detectors. Two types are used: surface barrier and silicon-lithium drifted. A summary of the detector stacks is shown in Table 14.

The low energy sensor uses five surface barrier detectors. The first four are used to determine the energy of the incoming protons. The fifth detector is

-
11. Brown, W.L., Higgenbotham, W.A., Miller, G.L., and Chase, R.L. (1969) Semiconductor Nuclear-Particle Detectors and Circuits, National Academy of Sciences, Publication 1594, Washington, D.C.
 12. Knoll, Glenn (1979) Radiation Detection and Measurement, John Wiley and Sons, New York, N.Y.

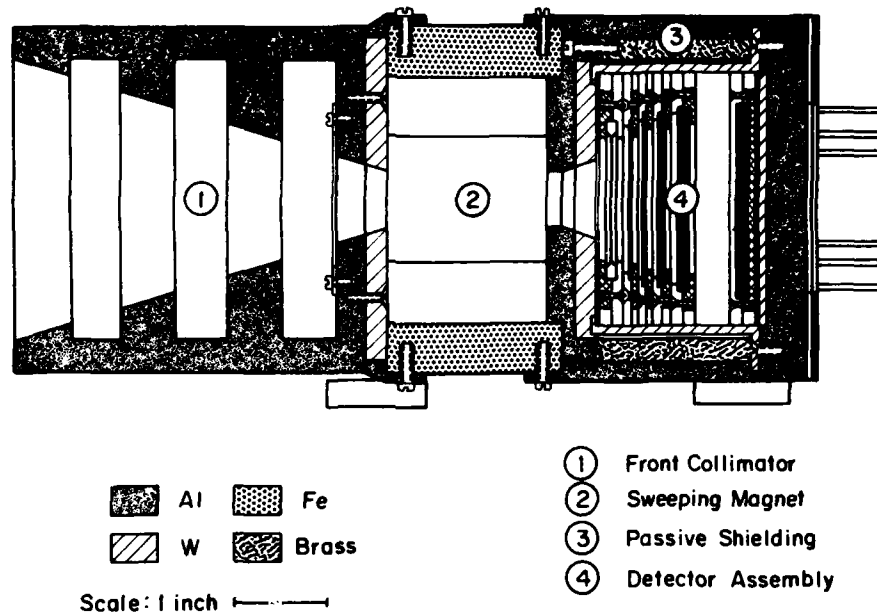


Figure 29a. Schematic of the Proton Telescope High Energy Sensor Head

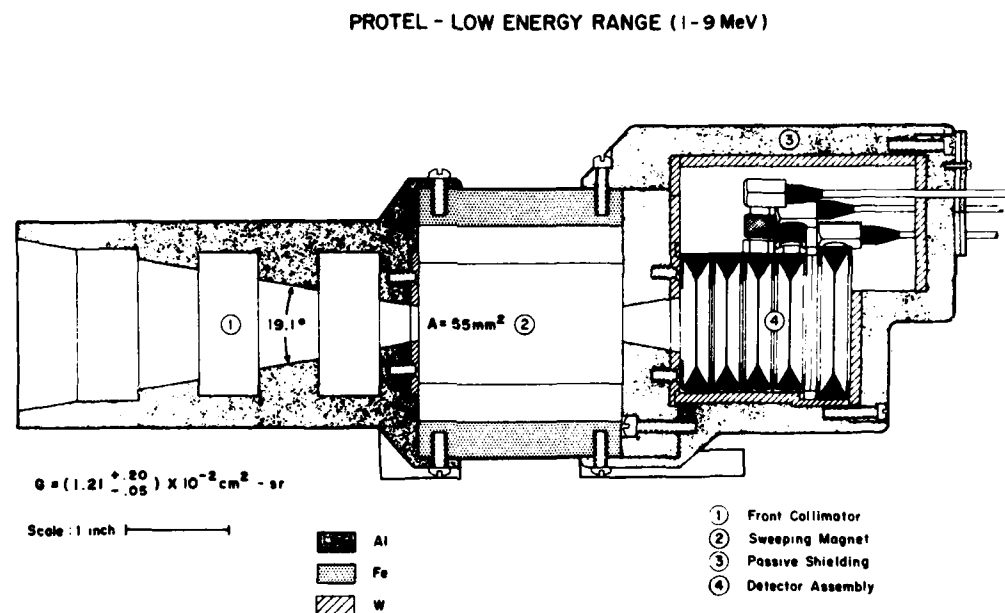


Figure 29b. Schematic of the Proton Telescope Low Energy Sensor Head

Table 14. (Prototype) Proton Telescope Detector Stacks

<u>SENSOR</u>	<u>DETECTOR</u>	<u>THICKNESS</u> (μ m)	<u>AREA</u> (mm 2)	<u>C</u> (pf)	<u>OVER BIAS</u> (V)
LE	1	23.6	200	920	+14
	2	31.1	300	990	+25
	3	73.5	400	600	+30
	4	248	450	189	+90
	5	308	600	210	+70
HE	1	325	437	140	+100
	1 (Ring)		341	109	
	2	448	638	155	+150
	2 (Ring)		392	95	
	3	902	760	90	+200
	3 (Ring)		447	53	
	4	1638	909	63	+250
	4 (Ring)		295	20	
	5	2984	1116	37	+400
	5 (Ring)		310	11	
	6	2996	1817	67	+400

separated from the rest by an aluminum absorber and is operated in anticoincidence to the other detectors to define the upper threshold of 9 MeV.

The high energy sensor uses six detectors, the first a surface barrier detector, and the remaining five, silicon-lithium drifted detectors. The first five determine the incoming proton energy. The sixth is separated by a brass absorber and is operated in anticoincidence to the other detectors in the stack to define the upper threshold of 100 MeV. In addition, pulse height analysis is performed on pulses from the first detector in the low energy head to provide broad integral energy information on higher mass particles present in the radiation belts.

One of the most serious considerations for any instrument is elimination of unwanted background. To eliminate penetrating protons and electrons and reduce bremsstrahlung as much as is feasible, we use 0.876 cm (HE, 0.770 cm) aluminum, (HE, 0.602 cm brass), and 0.254 cm (HE, 0.254 cm) tungsten alloy to encase the detector stacks for the detectors. This shielding corresponds to the range of 70 MeV (HE, 100 MeV) orthogonally impinging protons and 14 MeV electrons.

The silicon-lithium drifted detectors in the high energy sensor also have active shielding in the form of an anticoincidence "ring." The ring is part of the same silicon wafer as the detecting element, but is electrically isolated. This effectively creates a second "detector" that is outside the acceptance angle defined by the entrance and exit apertures. Pulses in the detector stack coincident with pulses in the ring will be rejected as arising from penetrating particles. (Detector 6 does not have the ring configuration.)

The range-energy relationship in silicon^{13, 14} determines the energy lost in each detector for a given incoming particle energy. Figures 30a, 30b, and 30c show the energy deposition curves for high mass particles in the first detector, and for protons in each of the detectors of the low and high energy sensor heads. The dashed lines show the boundaries of the energy channels for the three sets of measurements. Using charge sensitive preamps, the lost energy (ΔE) is converted from a charge to a voltage in a linear relationship. Two or three detectors (double or triple coincidence) are analyzed with pulse height analysis techniques to ascertain the proton energy. The required coincidences are listed in Table 15 as outputs.

-
13. Bichsel, H., and Tschalaer, C. (1967) A range-energy table for heavy particles in silicon, Nucl. Data, Section A 3:343.
 14. Skyrme, D.J. (1967) The passage of charged particles through silicon, Nucl. Instr. and Methods 57:61.

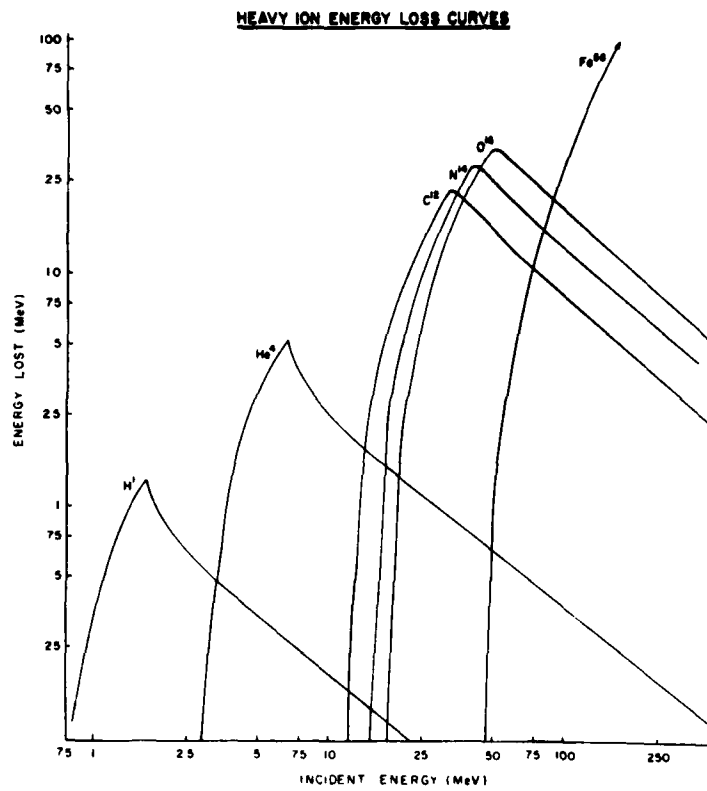


Figure 30a. Energy Deposition as a Function of Energy for High Mass Particles in the PROTEL Detector

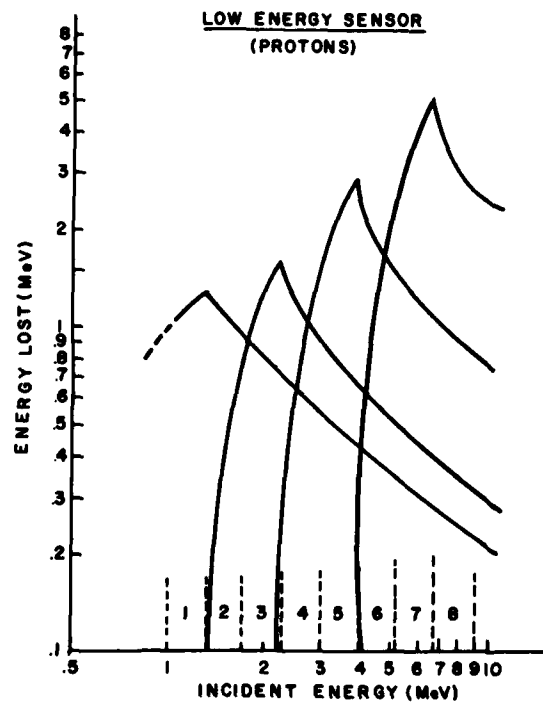


Figure 30b. Energy Deposition as a Function of Energy for Protons in the PROTEL Low Energy Sensor

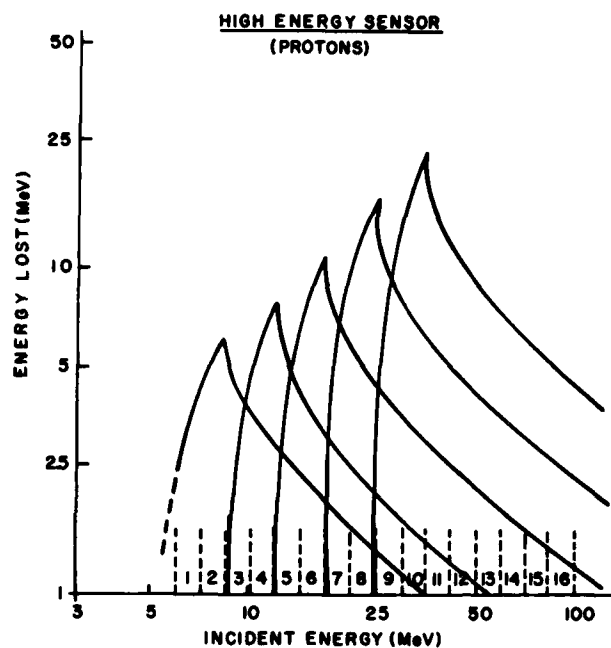


Figure 30c. Energy Deposition as a Function of Energy for Protons in the PROTEL High Energy Sensor

Table 15. Proton Telescope Coincidence Scheme (High Energy)

E_i (MeV)	DET 1	DET 2	DET 3	DET 4	DET 5
6.00	a_1				
7.15	a_2				
8.53	a_3	b_3			
10.17	a_4	b_4			
12.12	a_5	b_5	c_5		
14.45	a_6	b_6	c_6		
17.23			c_7	d_7	
20.54	a_7		c_8	d_8	
24.49				d_9	e_9
29.20				d_{10}	e_{10}
34.82				d_{11}	e_{11}
41.31				d_{12}	e_{12}
49.49	a_8			d_{13}	e_{13}
59.00				d_{14}	e_{14}
70.35				d_{15}	e_{15}
83.87				d_{16}	e_{16}
100.00					

4. FUNCTION BLOCK DIAGRAM

The basic objective of the electronics processing system is to analyze the output signals from the silicon detectors to determine the energy and flux of the incident protons that enter the sensor heads through their respective acceptance apertures, and to format that data for transmittal to the spacecraft telemetry system. The block diagram of the system in Figure 31 shows the basic components and their fundamental interconnections for the high energy sensor. The low energy electronics is identical in principle. The principal components of the system are the front end preamplifiers and buffer amplifiers, a coincidence and anticoincidence logic system, the pulse height analyzers and associated decoding logic, accumulator latches, data formatting μ -processor system, a command system, and a power supply system.

(a) The preamplifiers are commercial, low-power, hybrid integrated circuits configured as a charge amplifier followed by a single pole shaping amplifier with an approximate gain of 10. The charge amplifiers are located on the back of the detector housing in close proximity to the silicon detectors, reducing the cable and stray capacitance at the inputs and reducing the sensitivity to radiated EMI from the instrument and spacecraft systems.

(b) Buffer amplifiers are located in the data processing unit (DPU). These buffer amplifiers permit the gain adjustments for the different energy ranges of each detector. In addition, the buffers establish a low source impedance for the input to the logic and pulse height analysis circuitry.

(c) Pulse height threshold, detector coincidences, and active background rejection are the principal functions of the coincidence logic circuitry. Fast (~ 30 ns) level comparators are adjusted to detect the lowest energy level pulse for each detector. A coincidence window of $0.5 \mu\text{sec}$ is then established. Background rejection is performed logically using the outputs from the sixth detector of the high energy head, the fifth detector of the low energy head, and the ring detectors incorporated into the lithium drifted detectors.

(d) Each of the principal detectors has an associated pulse height analyzer (PHA); there are nine PHAs in all, five for the high energy head and four for the low energy head. These PHAs are of the stacked comparator type. The ΔE for each detector is established via the threshold settings of each comparator. The outputs of all PHAs are then logically compared to establish whether a unique amount of energy has been detected by each detector, thus establishing a valid proton event within a preset energy range. (A list of energies for each detector assembly is shown in Table 16.)

(e) Once a valid proton event has been established, it is then accumulated in a ripple counter and stored in a microprocessor memory system. The micropro-

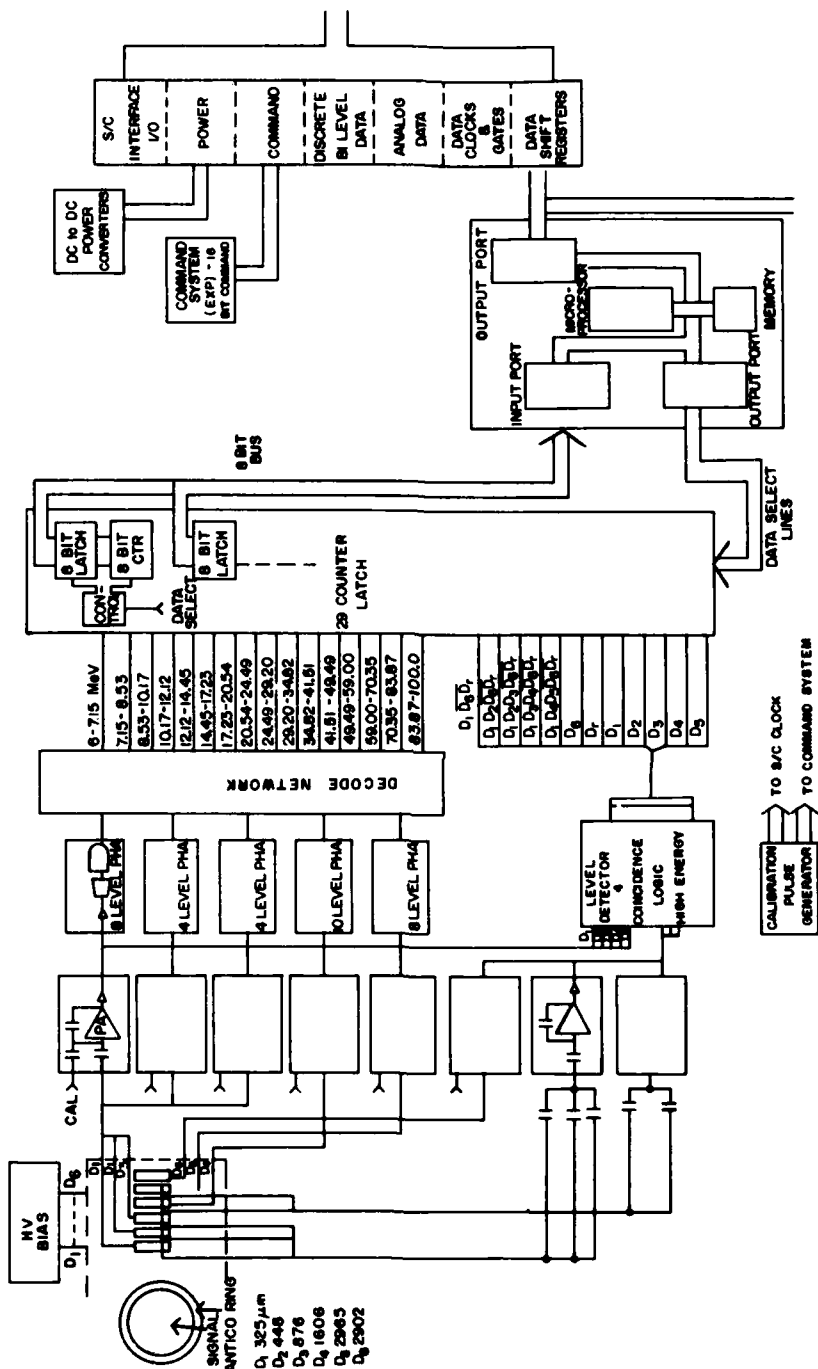


Figure 31. Function Block Diagram for the PROTEL High Energy Sensor

Table 16. Proton Telescope Detector Assembly Energies in MeV

<u>HIGH ENERGY</u>	<u>LOW ENERGY</u>
6.00	
7.15	
8.53	
10.17	1.00
12.12	1.32
14.45	1.73
17.23	2.28
20.54	3.00
24.49	3.95
29.20	5.20
34.82	6.84
41.51	9.00
49.49	
59.00	
70.35	
83.87	
100.00	

cessor system also formats the stored data and establishes the interface required to transmit the data to the spacecraft telemetry system.

The instrument is controlled by an experiment command system. A 16-bit command word supplied by the spacecraft is decoded into a four by eight matrix of static on-off command elements, with each commandable function controlled by one or more command elements. The more critical functions use several redundant elements.

References

1. Vette, J.L., Teague, M.J., Sawyer, D.M., and Chan, K.W. (1979) Modeling of the earth's radiation belts, in Solar-Terrestrial Predictions Proceedings (Vol. 2), R.F. Donnelly, Ed., U.S. Dept. of Commerce, Washington, D.C.
2. Fischer, H.M., Auschrat, V.W., Wibberenz, G. (1977) Angular distribution and energy spectra of protons of energy $5 \leq E \leq 50$ MeV at the lower edge of the radiation belt in equatorial latitudes, J. Geophys. Res. 82:537.
3. Reagan, J.B., Bakke, J.C., Kilner, J.R., Matthews, J.D., and Imhof, W.L. (1972) A high-resolution multiple-particle spectrometer for the measurements of solar particle events, IEEE Trans. Nucl. Sci. NS-19:554.
4. Filz, R.C., Katz, L., Sellers, B., Hanser, F.A., and Holeman, E. (1974) Observations of 5-45 MeV protons at $L \leq 3$ and $L \geq 7$, Space Res. 15:321-326.
5. Belian, R.D., Baker, D.N., Higbie, P.R., and Hones, E.W., Jr. (1978) High-resolution energetic particle measurements at 6.6 RE. 2. High-energy proton drift echoes, J. Geophys. Res. 83:4857.
6. Baker, D.N., Belian, R.D., Higbie, P.R., and Hones, E.W., Jr. (1979) High-energy magnetospheric protons and their dependence on geomagnetic and interplanetary conditions, J. Geophys. Res. 84:7138.
7. Parsignault, D.R., Holeman, E., and Filz, R.C. (1981a) Solar cycle induced modulation of the 55-MeV proton fluxes at low altitudes, J. Geophys. Res. 86:11493.
8. Parsignault, D.R., Holeman, E., and Filz, R.C. (1981b) Long-term intensity decrease in the 8- to 25-MeV proton fluxes at low L values, J. Geophys. Res. 86:11447.
9. Baum, J.J., Harman, R.W., Maronde, R.G., and Hornbuckle, T.A. (1972) Design of the particles experiment subsystem of the Apollo Luna Subsatellite, IEEE Trans. Nucl. Sci. NS-19:673.

10. Morel, P.R., Hanser, F.A., and Sellers, B. (1974) A Satellite Telescope for Protons and Alphas, Panametrics, Inc., Waltham, Mass., Final Rpt. AFCRL-TR-74-0531, AD A003727.
11. Brown, W.L., Higgenbotham, W.A., Miller, G.L., and Chase, R.L. (1969) Semiconductor Nuclear-Particle Detectors and Circuits, National Academy of Sciences, Publication 1594, Washington, D.C.
12. Knoll, Glenn (1979) Radiation Detection and Measurement, John Wiley and Sons, New York, N.Y.
13. Bichsel, H., and Tschalaer, C. (1967) A range-energy table for heavy particles in silicon, Nucl. Data, Section A 3:343.
14. Skyrme, D.J. (1967) The passage of charged particles through silicon, Nucl. Instr. and Methods 57:61.

Contents

1. Scientific Objectives	111
2. Application	111
3. Measuring Techniques	113
4. Function Block Diagram	115
References	119

11. The High Energy Electron Fluxmeter (AFGL-701-4)

by

D.A. Hardy
Air Force Geophysics Laboratory
Space Physics Division
Hanscom AFB, MA 01731

F. Hanser and B. Sellers
Panametrics, Inc.
Waltham, MA 02154

1. SCIENTIFIC OBJECTIVES

The High Energy Electron Fluxmeter (HEEF) is a solid state spectrometer telescope designed to measure the differential energy spectrum of electrons in the energy range of 1-10 MeV. Electrons in this energy range are the source of a significant portion of the total radiation dose received by microelectronic components in space systems operating in the Earth's radiation belts. Determining the average value and dynamic behavior of these electrons is critical to the CRRES program.

2. APPLICATION

Historically, measurements of electrons from 1-10 MeV have been strongly

affected by backgrounds produced by electron bremsstrahlung and penetrating energetic protons. This has restricted measurements to a maximum energy of 4 to 5 MeV, with by far the largest body of reported measurements below 3 MeV. Three types of detectors have been flown to make measurements in this energy range: (1) omnidirectional detectors, where the energy thresholds for each channel are set by a metal shield; (2) solid state detector telescopes, where the electron energy is determined by measuring the coincident energy deposition by the high energy electron within a stack of detectors; and (3) magnetic analyzers, where the energy separation is based on the energy dependence of the electron gyro-radius in the presence of a strong magnetic field.

Omnidirectional detectors were flown in the early sixties, as part of the diagnostics for the atmospheric nuclear tests,^{1, 2} and in the 1970s, when the data were incorporated into the AE1-7LO radiation belt model.³ These detectors are particularly prone to high backgrounds for bremsstrahlung produced in the metal shield that sets the energy thresholds. In addition, they generally measure the integral flux of electrons at energies above these thresholds so that differential measurements are possible only by differencing consecutive channels. With high backgrounds and a steeply falling spectrum, such differencing makes the measurements uncertain. The combination of these effects has limited useful data to measurements in the energy range of < 4 MeV.

^{4, 5, 6, 7, 8} Many groups have developed telescopes with stacks of solid state

-
1. Mozer, F.S., Elliott, D.D., Mihalov, J.D., Paulikas, G.A., Vampola, A.L., and Freden, S.C. (1963) Preliminary analysis of the fluxes and spectrum of trapped particles after the nuclear test of July 9, 1962, J. Geophys. Res. 68:641.
 2. Beall, D.S., Bostrom, C.O., and Williams, D.J. (1967) Structure and decay of the Starfish Radiation Belt, October, 1963, to December, 1965, J. Geophys. Res. 72:3403.
 3. Kirsch, E., Munch, J.W., and Scholer, M. (1975) Double structure in the outer electron radiation belt during geomagnetic activity, Planet. Space Sci. 23:913.
 4. Mihalov, J.D., and White, R.S. (1966) Energetic electron spectra in the radiation belts, J. Geophys. Res. 71:2217.
 5. Vernov, S.N., Gorchakov, E.V., Kuznetsov, S.N., Lagachev, Yu. I., Sosnovets, E.N., and Stalpovsky, V.C. (1969) Particle fluxes in the outer geomagnetic field, Rev. Geophys. 7:257.
 6. Williams, D.J., Keppler, E., Fritz, T.A., Wilken, B., and Wibberenz, G. (1978) The ISEE 1 and 2 medium energy particle experiment, IEEE Trans. Geosci. Electronics GE-16:270.
 7. Stevens, J.R., and Vampola, A.L. (1978) Description of the Space Test Program P78-2 Spacecraft and Payloads, SAMSO TR-78-24.
 8. Sagalyn, R.C., Spjeldvik, W.N., and Burke, W.J. (1981) Proceedings of the Air Force Geophysics Laboratory Workshop on the Earth's Radiation Belts: January 26-27, 1981, AFGL-TR-81-0311, AD A113959.

detectors and solid state detectors with scintillating crystals. Such experiments can provide differential spectra. However, they are limited at energies above ~ 5 MeV by bremsstrahlung and penetrating protons, which produce energy depositions within the detector stack that either are detected falsely as an electron, or that invalidate the coincidence scheme for the detection of a true, high-energy electron.

Several different groups^{9, 10, 11} have developed magnetic analyzers. All of these experiments have a series of solid state spectrometers in the "focal" plane of a strong magnet so that electrons of different energies will follow trajectories of different gyro-radii and impact different solid state detectors. Such instruments provide a differential energy spectrum but are prone to the same effects as the telescope systems, and are therefore limited, for good measurements, to an energy range below 4 to 5 MeV.

3. MEASURING TECHNIQUES

The High Energy Electron Fluxmeter is a telescope-type instrument that uses a single BGO scintillating crystal to detect and measure the electrons with energies between 1 and 10 MeV. To overcome the background problems encountered in the past by similar instruments, an electron, to be counted, must produce a triple coincidence of pulses, one in the BGO crystal and one in each of two solid state detectors; also, it must have a single anticoincidence with a plastic scintillator surrounding the BGO crystal.

The sensor head configuration is shown in Figure 32. The system eliminates background as follows: Protons incidence within the aperture with energies ≤ 100 MeV are rejected because of their large energy losses in the two solid state detectors. Similarly, for all energies above 30 MeV, protons are rejected because of their large energy loss in the BGO crystal. Thus, at all energies, in-aperture protons are rejected, and, in the energy range from 30 to 100 MeV, they are rejected by two different mechanisms. For out-of-aperture particles, the omnidirectional shielding is effective up to 140 MeV for protons and to > 20 MeV for electrons. Particles with sufficient energy to penetrate the shielding are rejected by

-
9. Pfitzer, K.A., and Winckler, J.R. (1968) Experimental observations of a large addition to the electron inner radiation belt after a solar flare event, *J. Geophys. Res.* 73:5792.
 10. West, H.I., Jr., Buck, R.M., and Walton, J.R. (1973) Electron pitch angle distributions throughout the magnetosphere as observed on Ogo 5, *J. Geophys. Res.* 78:1064.
 11. Vampola, A.L., and Kuch, G.A. (1978) Induced precipitation of inner zone electrons, I. Observations, *J. Geophys. Res.* 83:2543.

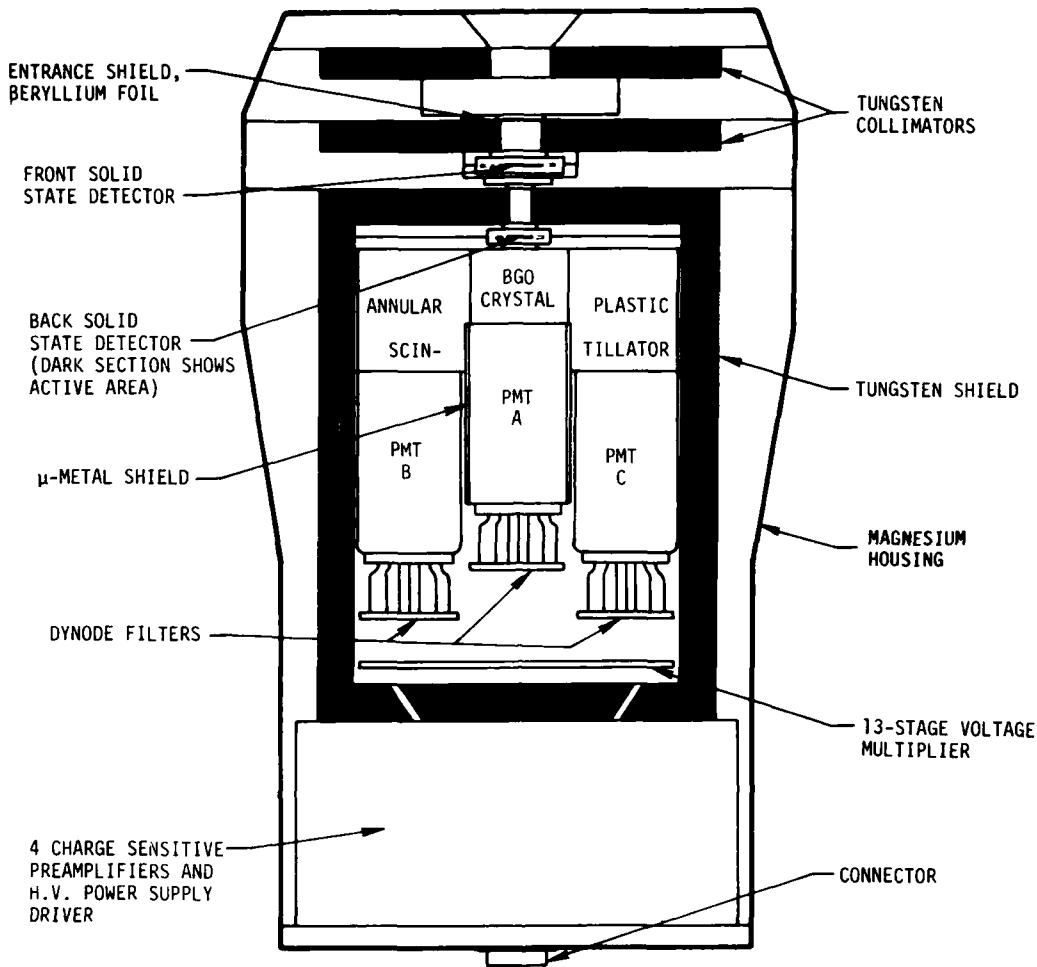


Figure 32. Schematic of the High Energy Electron Fluxmeter Sensor Head

the anticoincidence shield. A tungsten shield and tungsten collimators reduce bremsstrahlung effects. Magnesium shielding, which stops electrons below 10 MeV, is used near the crystal assembly to minimize bremsstrahlung generation. The tungsten collimator defines sharp transmission edges on the solid state spectrometers to minimize abnormally low energy losses produced by protons passing through the outer thin depletion region of the detector.

A beryllium shield 0.006-in thick stops in-aperture electrons below about 0.14 MeV. The solid state semiconductor detectors are 700 μm thick, having 100- and 50-mm² areas, respectively. This choice of detector thickness represents a compromise between 1000- μm detectors, which would not permit passage

of 1 MeV electrons into the BGO crystal, and 500- μ m detectors which may have noise problems because the energy loss by 10 MeV electrons is not large enough.

A BGO crystal is specially fabricated for this unit. The high density of BGO, about twice that of NaI(Tl), is of particular value in the present applications. Thus, 10 MeV electrons can be stopped in <1 cm, considerably minimizing the overall size of the assembly.

The BGO pulses are analyzed into 10 energy bins. We believe 10 bins will provide the spectral resolution to separate the AEI-7 HI and LO radiation belt models. In Table 17, we have listed the characteristics of the HEEF energy channels. From left to right, the columns give the threshold designation for the solid state detectors, the BGO crystal, and the plastic shield scintillator; the energy loss in each detector for each channel; the geometric factor for in-aperture particles; the geometric factor for omnidirectional detection; the electron and proton energy ranges in each channel; and the energy range for omnidirectional detected protons.

4. FUNCTION BLOCK DIAGRAM

The HEEF function block diagram is shown in Figure 33. In-aperture electrons in the range 1-10 MeV deposit sufficient energy in each of the three detectors (front and back solid state detectors and BGO crystal), configured in a properly defined telescope arrangement, so that the signals derived from them will satisfy a triple coincidence requirement. This requirement guarantees a high level of rejection of accidental coincidence and provides needed protection against "corner-cutting" protons. The output signal of a fourth detector (plastic scintillator surrounding the BGO crystal) negates the triple coincidence and is an additional guard against accidental coincidences caused by corner-cutters and omnidirectional protons.

A detailed description of how the system works is as follows:

Each electron of proper energy (1-10 MeV) that enters the aperture will create photons in the scintillation crystal and a charge pulse in each solid state (semiconductor) detector (SSD). The photons produced in the crystal are optically coupled to the photocathode of photomultiplier A(PMT-A). The resulting charge pulses at the anode are processed by the Charge Sensitive Preamplifiers (CSPA)-shaping amplifier-voltage amplifier chain, and passed along to the BGO Pulse Height Analyzer (PHA) via the zero crossing detector/single channel analyzer (ZCD/SCA). The ZCD/SCA produces a very fast output pulse (BGO COINC) for any electron of incident energy >1 MeV.

Two identical CSPAs and associated PHAs process the charge pulses from the front and back SSD, respectively. This processing results in a rough energy

Table 17. High Energy Electron Fluxmeter: Channel Geometric Factors and Particle Detection Ranges

Channel Designation	Energy Loss (MeV)	Geometric Factors		Telescope Energy Ranges (MeV)		Omnidirectional Energy Ranges (MeV)	
		Telescope	Omni	Electrons	Protons	Protons	Protons
Solid State Detectors							
>S2, Front	>0. 80	0. 167	6. 06	-	4. 2-130	116-265	
>S1, Front	>0. 50	0. 167	6. 06	-	4. 1-269	116-588	
W1, Front	0. 13-0. 50	0. 167	6. 06	>0. 20	3. 97-4. 12/269-∞	115. 51-115. 65/558-∞	
W2, Front	0. 13-0. 80	0. 167	6. 06	>0. 20	3. 97-4. 24/130-∞	115. 51-115. 76/265-∞	
>S2, Back	>0. 80	0. 0120	3. 11	-	11. 2-130	116-265	
>S1, Back	>0. 50	0. 0120	3. 11	-	11. 1-270	116-588	
W1, Back	0. 13-0. 50	0. 0120	3. 11	>0. 52	11. 00-11. 13/270-∞	115. 51-115. 65/588-∞	
W2, Back	0. 13-0. 80	0. 0120	3. 11	>0. 52	11. 00-11. 23/130-∞	115. 51-115. 76/265-∞	

Table 17 (Contd). High Energy Electron Fluxmeter: Channel Geometric Factors and Particle Detection Ranges

Channel Designation <u>BG0 Crystal</u>	Energy Loss (MeV)	Geometric Factors			Telescope Energy Ranges (MeV)		Omnidirectional Energy Ranges (MeV)	
		<u>Telescope</u>	<u>Omni</u>	<u>Electrons</u>	<u>Protons</u>	<u>Protons</u>	<u>Protons</u>	<u>Protons</u>
>L10s	> 9.40	0.0120	78. 6	>10	19. 3- ∞		117- ∞	
>L10c	> 9.40	0.0120	78. 6	>10	19. 3- ∞ / (270- ∞)*		117- ∞	
L9 - L10	7. 41-9. 40	0. 0120	78. 6	8 - 10	18. 5-19. 3		116. 29-116. 51	
L8 - L9	5. 42-7. 41	0. 0120	78. 6	6 - 8	17. 7-18. 5		116. 07-116. 29	
L7 - L8	4. 43-5. 42	0. 0120	78. 6	5 - 6	17. 3-17. 7		115. 96-116. 07	
L6 - L7	3. 44-4. 43	0. 0120	78. 6	4 - 5	16. 9-17. 3		115. 84-115. 96	
L5 - L6	2. 95-3. 44	0. 0120	78. 6	3. 5 - 4	16. 7-16. 9		115. 79-115. 84	
L4 - L5	2. 45-2. 95	0. 0120	78. 6	3 - 3. 5	16. 5-16. 7		115. 73-115. 79	
L3 - L4	1. 96-2. 45	0. 0120	78. 6	2. 5 - 3	16. 3-16. 5		115. 68-115. 73	
L2 - L3	1. 46-1. 96	0. 0120	78. 6	2 - 2. 5	16. 1-16. 3		115. 62-115. 68	
L1 - L2	0. 96-1. 46	0. 0120	78. 6	1. 5 - 2	15. 9-16. 1		115. 57-115. 62	
LL - L1	0. 44-0. 96	0. 0120	78. 6	1 - 1. 5	15. 7-15. 9		115. 51-115. 57	
Any BG0 (>LLL)	> 0. 44	0. 0120	78. 6	>1	15. 7- ∞		116- ∞	
<u>Plastic Shield Scintillator</u>								
Ls	>1	-	-	525	-		98- ∞	

* For coincidence operation

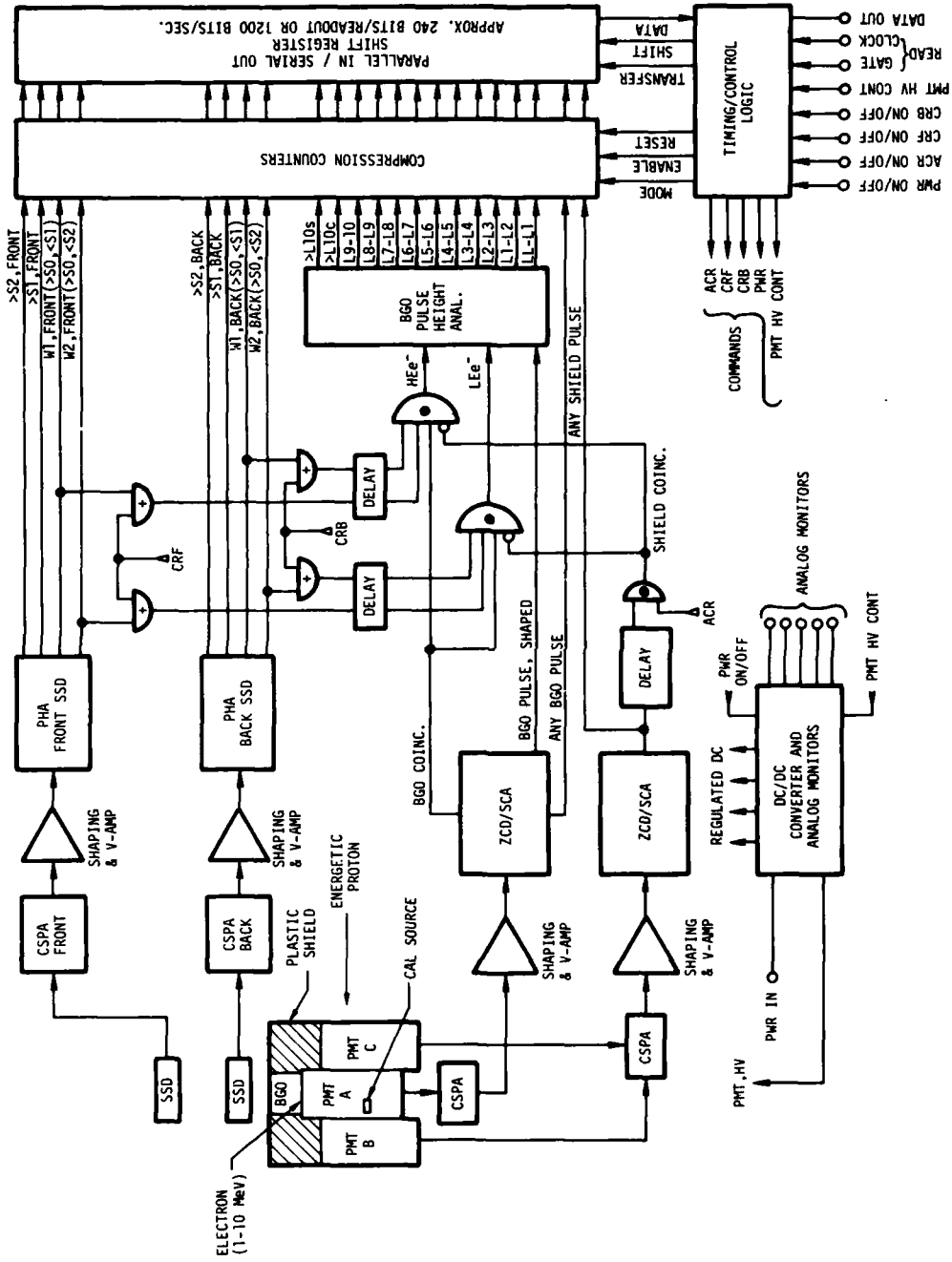


Figure 33. Function Block Diagram for the High Energy Electron Fluxmeter

distribution determined by two windows and by two thresholds set for the solid state detectors. In addition, the two windows set in each PHA are put into fast coincidence with the BGO COINC signal to identify positively that an electron entering from the front of the detectors is to be analyzed. Analysis of the BGO PULSE, SHAPED, is then carried out in the BGO PHA for 10 differential energy ranges and 2 threshold ranges. Energetic protons that create photons in the anticoincidence shield are detected by PMT-B and PMT-C, whose anode pulses are summed and processed by a CSPA-shaping amplifier-voltage amplifier chain. Again, a ZCD/SCA produces a very fast timing pulse (SHIELD COINC) which vetos triple coincidence as described above. The uniform output pulses from the SSD and BGO PHAs plus one additional output from each ZCD/SCA labeled ANY BGO PULSE and ANY SHIELD PULSE, are accumulated in an array of 22 compression counters. The contents of these counters are parallel-transferred to shift registers, where they are serially read out by the spacecraft data processing system every 0.5 seconds.

The fast timing pulses from the output of the SSDs and the SHIELD COINC are delayed to accommodate the slower decay time of the BGO crystal. Thus, a fast triple coincidence or veto is assured by the four input AND gates (coincidence gates). The coincidence requirement of the front (CRF) and back (CRB) SSDs as well as the anticoincidence requirement (ACR) of the plastic shield are enabled or disabled individually on ground command. Thus, the calibration source and changes in the channel count rates from the ambient fluxes can verify proper operation of individual detectors and their electronics.

All signals to and from the spacecraft are interfaced with the instrument through the Timing/Control Logic. Low-voltage power and PMT high voltage are derived from the 28 V spacecraft bus via a DC/DC converter, which also supplies all analog monitors. the PMT HV is adjustable by ground command.

References

1. Mozer, F.S., Elliott, D.D., Mihalov, J.D., Paulikas, G.A., Vampola, A.L., and Freden, S.C. (1963) Preliminary analysis of the fluxes and spectrum of trapped particles after the nuclear test of July 9, 1962, J. Geophys. Res. 68:641.
2. Beall, D.S., Bostrom, C.O., and Williams, D.J. (1967) Structure and decay of the Starfish Radiation Belt, October, 1963, to December, 1965, J. Geophys. Res. 72:3403.
3. Kirsch, E., Munch, J.W., and Scholer, M. (1975) Double structure in the outer electron radiation belt during geomagnetic activity, Planet. Space Sci. 23:913.

4. Mihalov, J.D., and White, R.S. (1966) Energetic electron spectra in the radiation belts, J. Geophys. Res. 71:2217.
5. Vernov, S.N., Gorchakov, E.V., Kuznetsov, S.H., Lagachev, Yu. I., Sosnovets, E.N., and Stalpovsky, V.C. (1969) Particle fluxes in the outer geomagnetic field, Rev. Geophys. 7:257.
6. Williams, D.J., Keppler, E., Fritz, T.A., Wilken, B., and Wibberenz, G. (1978) The ISEE 1 and 2 medium energy particle experiment, IEEE Trans. Geosci. Electronics GE-16:270.
7. Stevens, J.R., and Vampola, A.L. (1978) Description of the Space Test Program P78-2 Spacecraft and Payloads, SAMSO TR-78-24.
8. Sagalyn, R.C., Spjeldvik, W.N., and Burke, W.J. (1981) Proceedings of the Air Force Geophysics Laboratory Workshop on the Earth's Radiation Belts: January 26-27, 1981, AFGL-TR-81-0311, AD A113959.
9. Pfitzer, K.A., and Winckler, J.R. (1968) Experimental observations of a large addition to the electron inner radiation belt after a solar flare event, J. Geophys. Res. 73:5792.
10. West, H.I., Jr., Buck, R.M., and Walton, J.R. (1973) Electron pitch angle distributions throughout the magnetosphere as observed on Ogo 5, J. Geophys. Res. 78:1064.
11. Vampola, A.L., and Kuch, G.A. (1978) Induced precipitation of inner zone electrons, 1. Observations, J. Geophys. Res. 83:2543.

Contents

1. Scientific Objectives	121
2. Application	122
3. Measuring Techniques	122
References	124

12. The Relativistic Proton Detector (AFGL-701-7A)

by

R.W. Fillius
University of California, San Diego
La Jolla, CA 92093

J.B. Blake, D. Chenette, and A. Kolasinski
Aerospace Corporation
P.O. Box 92957
Los Angeles, CA 90009

1. SCIENTIFIC OBJECTIVES

As the name of the experiment implies, the immediate objective of the Relativistic Proton Detector is to measure the energy spectra and pitch angle distributions of relativistic protons trapped in the inner Van Allen belt. Extensive reviews of the physics of radiation belt protons have been given by Schulz¹ and by Schulz and Lanzerotti.² On the experimental side, the most up-to-date model of the trapped-proton environment is the AP-8 Model of Sawyer and Vette.³ The most

-
1. Schulz, M. (1975) Geomagnetically trapped radiation, Space Sci. Rev. 17:481.
 2. Schulz, M., and Lanzerotti, L.J. (1974) Particle Diffusion in the Radiation Belts, Springer, Heidelberg.
 3. Sawyer, D.M., and Vette, J.R. (1976) AP-8 Trapped Proton Environment and Solar Minimum, NSSDC/WDC-A-R&S 76-06, Goddard Space Flight Center, Greenbelt, MD 20771.

recent inner zone proton data above 100 MeV are those published by Croley et al⁴ and Kolasinski and Chenette.⁵

2. APPLICATION

A complete data base on the trapped proton flux at energies above 200 MeV and L-values ranging between 1.1 and 1.7 does not exist. Data of these kinds will be useful in answering several outstanding theoretical questions. One question is, What is the maximum energy of the trapped flux at various L-values? Others are, Should high energy data be used to validate assumptions concerning the secular variation of the Earth's magnetic field? and What is the effect of this variation on the trapped, energetic proton population?

3. MEASURING TECHNIQUES

The Relativistic Proton Detector design is based on a sensor flown aboard the Pioneer 10 and 11 spacecraft to Jupiter.⁶ The primary sensor is a Cerenkov radiator viewed by a photomultiplier tube. Two copies of this sensor with different radiators extend the energy range response over the Pioneer detectors. One of the radiators is an alcohol-water mixture as flown aboard the Pioneer 10/11 spacecraft. The other radiator is fused silica. The alcohol-water radiator has an index of refraction of 4/3 and responds to protons with energies above 440 MeV. The fused-silica radiator has an index of 3/2 and responds to protons above 320 MeV.

In addition to the Cerenkov radiators, the AFGL-701-7A sensor will include another detector system from the Pioneer 10/11 experiment which is to measure electrons. This system consists of two detectors: an electron scatter detector (E) for electrons with energies above 200 keV, and a heavily shielded minimum-ionizing detector (M) for penetrating electrons (>35 MeV) and protons (>80 MeV).

Finally, we have also included in this package a photometer system to view the GTO chemical releases. The photometer will measure narrow-band emissions

-
4. Croley, D.R., Jr., Shulz, Michael, and Blake, J.B. (1976) Radial diffusion of inner-zone protons: Observations and variational analysis, J. Geophys. Res. 81:585.
 5. Kolasinski, A., and Chenette, D. (1982) The inner zone trapped proton flux, 50-600 MeV: Measurements compared to the AP-8 model, Trans. Am. Geophys. Union (EOS) 163:1077.
 6. Fillius, R.W., and McIlwain, C.E. (1974) Measurements of the Jovian radiation belts, J. Geophys. Res. 79:3589.

from lithium, barium, and europium in four wavelength regions simultaneously using a split-anode microchannel plate photomultiplier tube. (See Figure 34.)

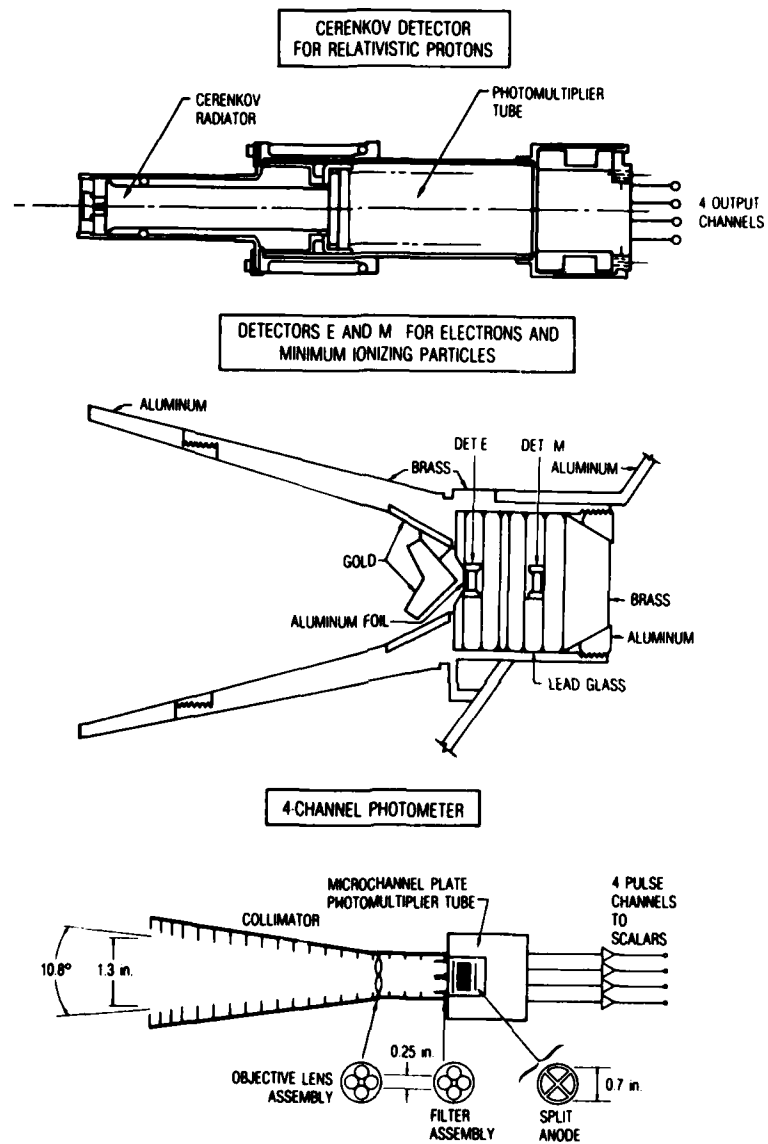


Figure 34. Schematic Diagram of Sensors in the AFGL-701-7A Package:
(a) Cerenkov Counters; (b) Electron Detector; (c) Photometer

References

1. Schulz, M. (1975) Geomagnetically trapped radiation, Space Sci. Rev. 17:481.
2. Schulz, M., and Lanzerotti, L.J. (1974) Particle Diffusion in the Radiation Belts, Springer, Heidelberg.
3. Sawyer, D.M., and Vette, J.R. (1976) AP-8 Trapped Proton Environment and Solar Minimum, NSSDC/WDC-A-R&S 76-06, Goddard Space Flight Center, Greenbelt, MD 20771.
4. Croley, D.R., Jr., Schulz, Michael, and Blake, J.B. (1976) Radial diffusion of inner-zone protons: Observations and variational analysis, J. Geophys. Res. 81:585.
5. Kolasinski, A., and Chenette, D. (1982) The inner zone trapped proton flux, 50-600 MeV: Measurements compared to the AP-8 model, Trans. Am. Geophys. Union (FOS) 163:1077.
6. Fillius, R.W., and McIlwain, C.E. (1974) Measurements of the Jovian radiation belts, J. Geophys. Res. 79:3589.

13. The Proton Switch (AFGL-701-7B)

by
J.B. Blake
Aerospace Corporation
Los Angeles, CA 90009

The proton switch consists of two single detector units in an omnidirectional configuration (Figure 35). These units measure the fluxes of protons in the energy ranges from 20 MeV to 80 MeV. The purpose of the proton switch is to signal the data processing unit (DPU) when energetic protons are present so that the DPU can modify the telemetry allocation among the various Aerospace sensors.

The two omnidirectional sensors use small, cubical, lithium-drifted silicon detectors centered under a hemispherical aluminum bubble (Figure 36). The lower proton energy threshold of each of the sensors is determined primarily by the thicknesses of the hemispherical bubbles. Protons are separated unambiguously from electrons by setting the discriminator level well above the maximum energy an electron can deposit in the small semiconductor detector. (Energy loss per unit path length, dE/dx , is much greater for protons than for electrons in the energy range of geophysical interest.) The absence of electron contamination in the proton channels is verified by electron irradiation of the sensors.

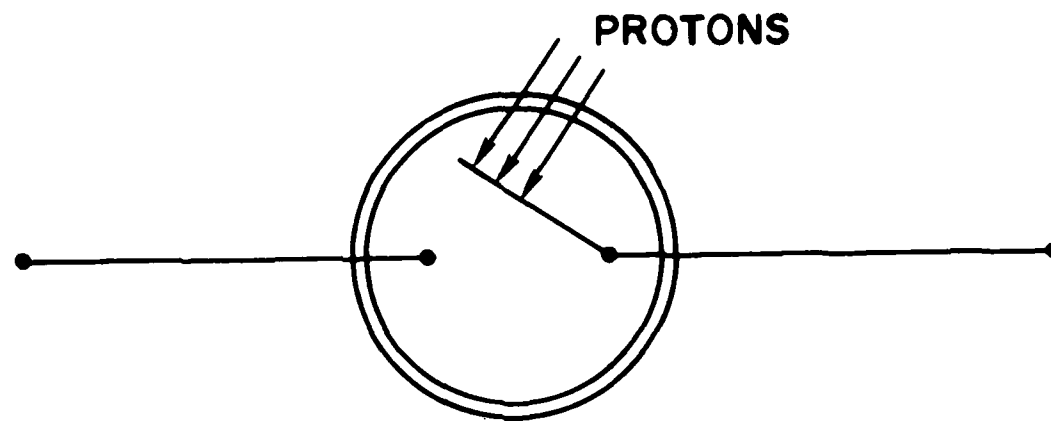


Figure 35. Schematic Diagram of the Proton Switch

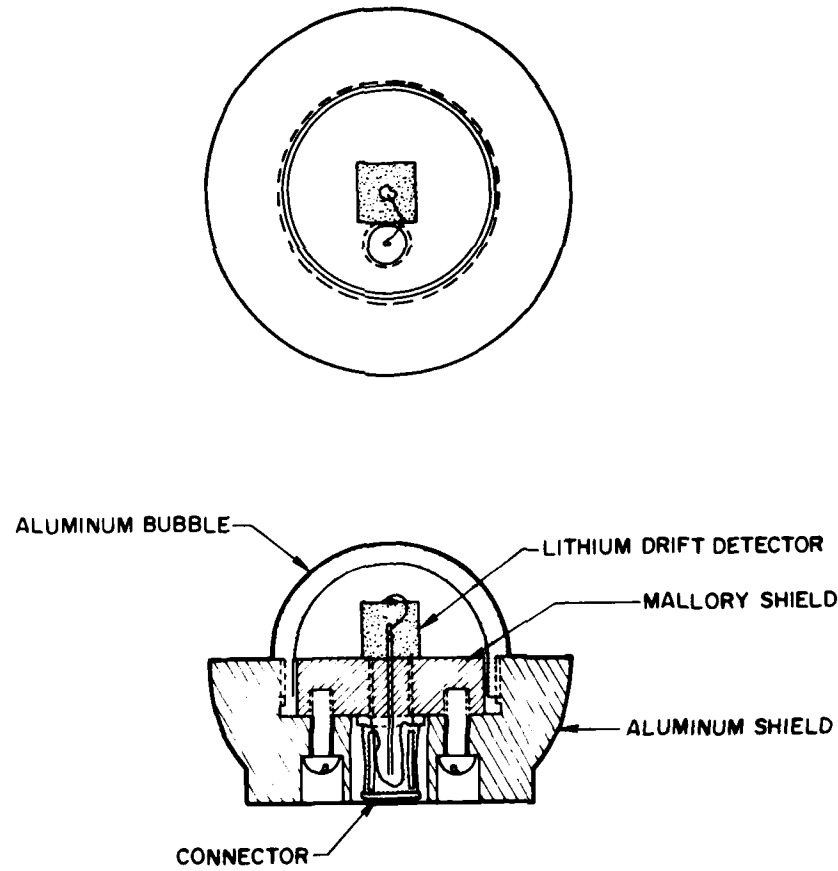


Figure 36. Schematic of the Proton Switch Sensor

Contents

1. Scientific Objectives	127
2. Applications	128
3. Measuring Techniques and Function Block Diagrams	128

14. The Mass Composition Instruments (AFGL-701-11)

by

T.A. Fritz, D.T. Young, W.C. Feldman,
S.J. Bame, J.R. Cessna, and D.N. Baker
Los Alamos National Laboratory
Los Alamos, NM 87545

B. Wilken, W. Studeman, and P. Winterhoff
Max Planck Institut fur Aeronomie
Kaltenburg, Lindau 3, West Germany

D.A. Bryant and D.S. Hall
Rutherford-Appleton Laboratory
Chilton, Didcot, Oxfordshire, UK

J.F. Fennell, D. Chenette, N. Katz,
S.I. Imamoto, and R. Koga
Aerospace Corporation
Los Angeles, CA 90009

F. Soeraas
University of Bergen
Bergen, Norway

I. SCIENTIFIC OBJECTIVES

The objective of the SPACERAD Mass Composition Instruments is the unambiguous determination of the composition of the plasma and energetic particle populations of the Earth's Van Allen radiation belts over the range of 40 eV/Q to 15 MeV per ion to identify mechanisms that energize charged particles and transport them from their parent source populations to the magnetosphere.

2. APPLICATIONS

The two main sources of particles in the magnetosphere are the solar wind and the ionosphere. The principal tracers of plasma origin will be measurements of the following ion flux ratios: $^2\text{H}/^1\text{H}$, $^3\text{He}/^4\text{He}$, $^{12}\text{C}/^{16}\text{O}$, $^{14}\text{N}/^{16}\text{O}$, $^4\text{He}/^{20}\text{Ne}$, $^{20}\text{Ne}/^{36}\text{Ar}$, and $^{24}\text{Mg}/^{16}\text{O}$; and the following charge state density ratios: $\text{He}^{++}/\text{H}^+$, He^+/H^+ , O^+/H^+ , and O^{++}/O^+ . These measurements will be made at different locations and over a wide energy range. The energy dependence of the flux ratios will indicate the relative strength of the sources throughout the radiation belts and the as yet undetermined coupling between the magnetosphere and the two source regions. The excellent energy coverage of the Mass Composition Instruments will permit elemental and isotopic abundance determination of energetic ions known to be produced, energized, transported, and lost during substorms and main phase magnetic storms, and of energetic solar particles from flares and solar cosmic rays. These instruments will also permit studies of ion composition dependent boundary-layer processes, identification of radiation belt regions by their dominant composition, and differentiation of mass and mass-per-charge dependent transport mechanisms. This information is critical input to any dynamic model of the Earth's radiation belts. These instruments will also monitor the radiation belt energetic mass composition to properly interpret the mass-dependent effects of the Earth's radiation environment on the Microelectronics Experiment (AFGL-701-1A).

3. MEASURING TECHNIQUES AND FUNCTION BLOCK DIAGRAMS

The Mass Composition Instruments incorporate three types of sensor systems: the Low Energy Magnetospheric Ion Composition Sensor (LOMICS), the Magnetospheric Ion Composition Sensor (MICS), and the Heavy Ion Telescope (HIT). Each of these performs a multiple-parameter measurement of the composition of magnetospherically trapped and transient ion populations over a combined energy range from 40 eV/Q to 15 MeV per ion (a range of over five and one-half orders of magnitude) and for elements from hydrogen through iron. A summary of the three instrument parameters is given in Table 18.

3.1 Low Energy Magnetospheric Ion Composition Sensor (LOMICS)

LOMICS consists of a 90° spherical section analyzer, a post-acceleration voltage of 10 kV, followed by multiple time-of-flight (TOF) analyzers. The TOF mass analysis technique is usually restricted to high energy particles that undergo relatively little scattering and energy loss in generating start and stop signals.

Table 18. Mass Composition Instrument Parameters

	<u>LOMICS</u>	<u>MICCS</u>	<u>HIT</u>
SPECTRAL RANGE	40 eV/Q - 40 keV/Q	30 keV/Q - 400 keV/Q	100 keV/ion - 15 MeV/ion
FIELD OF VIEW / SPATIAL RESOLUTION	±6° x 90° with three 30° FOV's centered at 60°, 90°, 120° to \hat{S}	±1° conical at 90° to \hat{S}	±6° conical at 90° to \hat{S}
TEMPORAL RESOLUTION	4.096 s	65.4 s	
ENERGY RESOLUTION $\Delta(E/Q)$	7.5%	10%	< ~10% (NOMINAL)
GEOMETRIC FACTOR	$3.8 \times 10^{-4} \text{ cm}^2 \text{ ster}$	(0.6-1.0) • $10^{-2} \text{ cm}^2 \text{ ster}$	$2 \times 10^{-2} \text{ cm}^2 \text{ ster } \Delta E/E$
SENSITIVITY	SINGLE EVENTS TO $> 5 \times 10^7$ particles/cm ² ster sec		
\hat{S} = Spin Axis			

However, TOF analysis on low energy (\sim eV) ions can be performed if energy/-charge analyzed ions are post-accelerated through a -10.0 kV potential and very thin foils (\sim 1 $\mu\text{g cm}^{-2}$) are used. At the lowest ion energies covered by LOMICS (\sim 40 eV), a mass resolution of $M/\Delta M \sim 2$ can be achieved, sufficient for E/Q and M/Q analysis of the major magnetospheric ion species. Mass resolution should improve with increasing ion energy, which is one advantage of TOF over more conventional magnetic mass spectrometry in this energy range. A second advantage, also exploited on LOMICS, is that large polar angles of acceptance are possible because of the compactness and low weight of the TOF design.

Figure 37 is a schematic diagram of the LOMICS sensor. The 90° spherical section analyzer selects ions with an energy resolution of 7.5 percent. This resolution is somewhat higher than usual to reduce the spread of ion speeds within the TOF section and hence improve mass resolution. Ions exiting the spherical

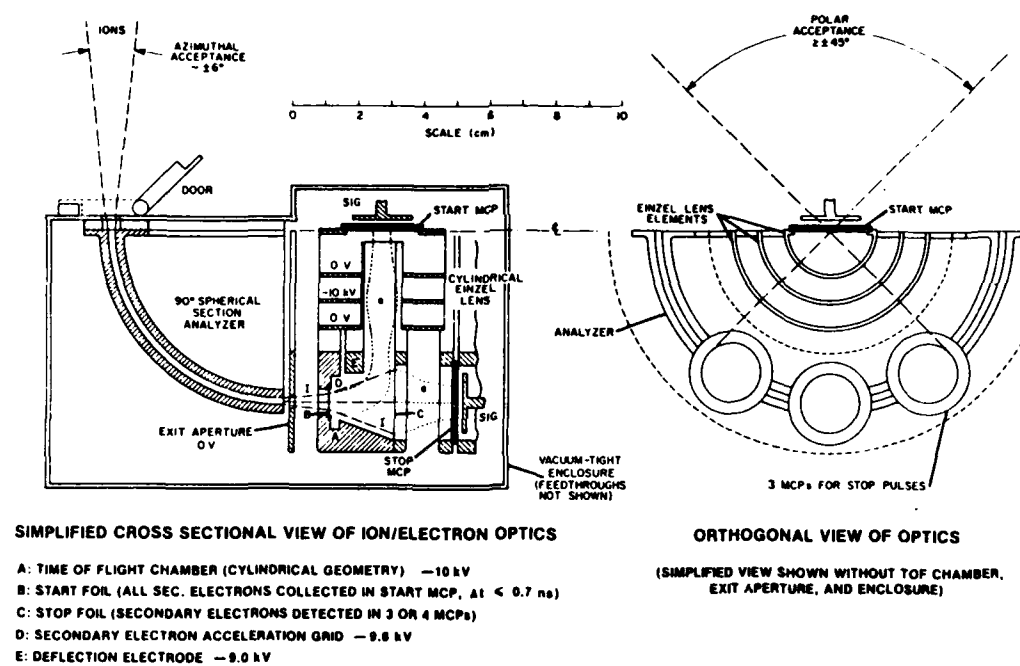


Figure 37. Schematic of the Low Energy Magnetospheric Ion Composition Sensor (LOMICS)

section analyzer are accelerated by -10.0 kV applied to the TOF unit so that they strike the front foil of the TOF analyzer with $(E_0 + 10.0)Q$ keV, where E_0 is the incident ion energy, and Q is its charge. Ions pass through the extremely thin ($1 \mu\text{g}/\text{cm}^2$ or about 100\AA) carbon foil and cause secondary electrons to be emitted from the back of the foil. These secondaries are accelerated, deflected, and focused onto an 18-mm-diameter microchannel plate (MCP) which then emits a START pulse that triggers the LOMICS timing logic. The ion proceeds along a 2.5-cm flight path to a second thin foil through which it passes, emitting another burst of secondary electrons that give rise to a STOP timing pulse in the appropriate MCP. Depending on the ion's polar angle at entrance, it will excite one of three of the STOP MCP's, thus giving polar angle resolution of 30° .

The electronics within the HMSB box are time-shared with the HIT sensor. During the LOMICS cycle, the ESA voltage is swept from the maximum value of 4.5 kV to near zero in 4.096 seconds. (This voltage can also be stepped under control of the data processing unit (DPU).)

As described above, ions with the appropriate E/Q will produce START and STOP signals by a secondary electron technique. These signals are fed into a Time-to-Amplitude Converter (TAC) associated with LOMICS, and a pulse, proportional to the ion TOF, is converted by the same ADC as used in the HIT mode to 10 bits. Simultaneously with the recognition of a LOMICS valid event, the ESA plate voltage is sampled and digitized to 5 bits. A 2 bit ID code is also developed that indicates which of the three polar look angle directions contained the incident ion. These digitized values (E/Q , ID, TOF) are clocked out to the DPU for processing. Every START and STOP pulse (three polar angles) plus two other parameters are accumulated continuously, independent of the experiment mode, by six accumulators within the HMSB box, and are clocked out to the DPU at the time resolution of 0.128 seconds. The two parameters noted above correspond to ions whose TOF is between 5 and 20 nsec (H-channel) and between 20 and 100 nsec (O-channel). In this manner, a rough measurement of the light ions, nominally hydrogen, will be sampled continuously by the H-channel, and intermediate ions, nominally oxygen, will be sampled continuously by the O-channel.

The data handling is discussed in Section 3.4.

3.2 Magnetospheric Ion Composition Sensor (MICS)

The MICS sensor uses a conically shaped electrostatic analyzer, a secondary-electron generation/detection system, and a solid state detector to measure the energy, TOF, and the energy per charge of the incident ion flux. These three parameters permit a unique determination of the ion charge state, mass, and incident energy over the energy range from $\sim 30 \text{ keV}/Q$ to $400 \text{ keV}/Q$.

A schematic of the sensor is presented in Figure 38. The variable voltage

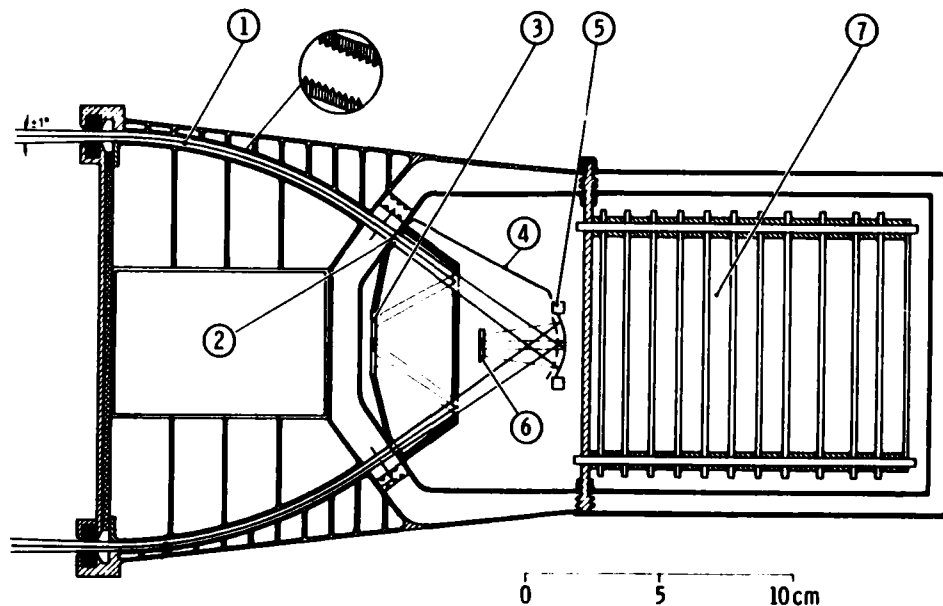


Figure 38. Schematic Diagram of the Magnetospheric Ion Composition Sensor (MICS)

power supply (VVPS) biases the E/Q analyzer plates from 0 V to 11 kV (1 in Figure 38). The ions exiting from the E/Q analyzer pass through a carbon foil (2), cross a drift region of 7-10 cm in length (4) to a solid state detector (SSD) where their energy, E, is measured (5). Secondary electron emission from the foil generates a START signal (3), and electron emission from the SSD generates a STOP signal (6). These are fed into a TAC. The output, which represents the TOF of the ion through the drift region, is digitized to 10 bits if the event is acceptable. The E signal is compared to the TOF signal in the E-channel electronics. The decision to analyze the event is based on coincidence constraints. The analysis proceeds by controlling the TRIGGER LOGIC. When enabled, this logic allows the digitization of the E and TOF signals to occur. The digitized TOF and E values for each analyzed event are clocked out to the DPU using a sensor generated clock.

Figure 39 presents a function block diagram of the MICS sensor. It shows the significant sections of the electronics at near-board level.

For every STOP, START, TOF, and E signal generated, the appropriate Sensor Event Counter is incremented. Some particle identifications, primarily for protons and alpha particles, are made from the pulse analog data and their number accumulated in other counters. Internal operating voltages, detector biases, temperatures, and sensor modes are generated as digital housekeeping

HMSA BLOCK DIAGRAM AFGL-701-11A ON CRRES

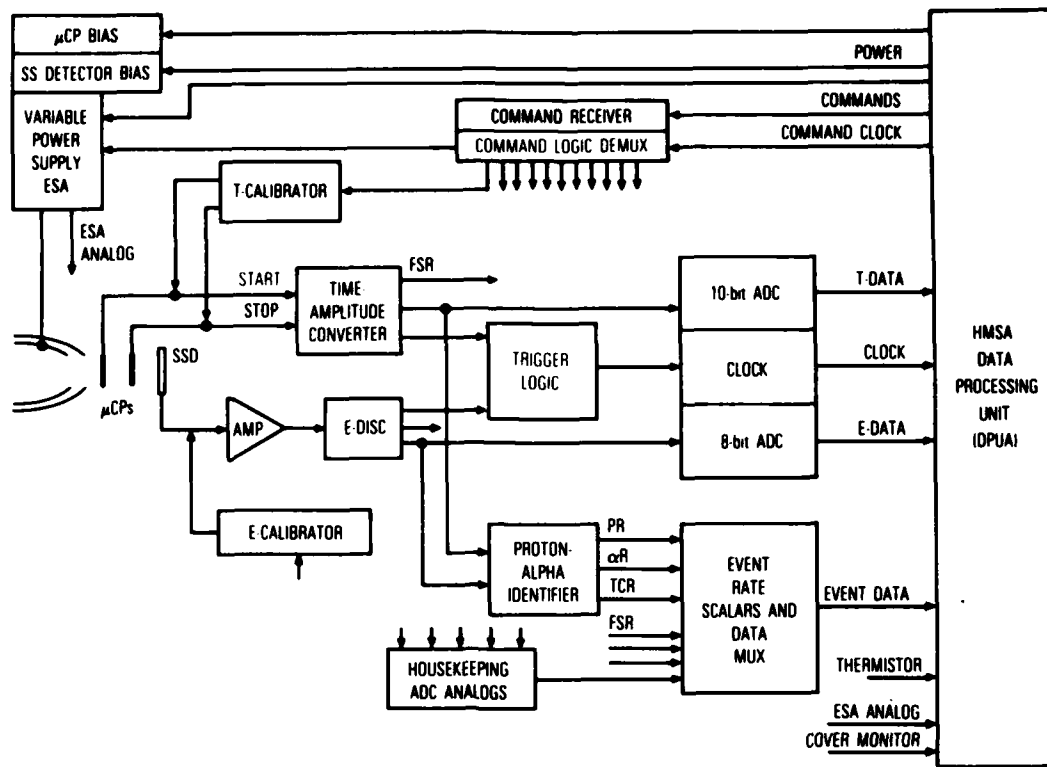


Figure 39. Function Block Diagram of the Magnetospheric Ion Composition Sensor (MICS)

(HK) data using an ADC. These HK and counter values are clocked out to the DPU in response to DPU commands.

Test E and TOF signals can be generated, in response to DPU commands, to verify the calibration of the sensor electronics and provide a data stream for ground tests. The ADC parameters and TRIGGER LOGIC can be changed by command.

The DPU supplies to the sensor the required regulated +28 VDC power, the E/Q step codes for controlling the VVPS, the mode commands, and a clock. The DPU itself is discussed in Section 3.4.

3.3 Heavy Ion Telescope (HIT)

The HIT sensor uses a three-element solid state detector telescope to measure the rate of energy loss, the ion incident energy, and its TOF. These three

parameters permit a unique determination of the ion mass, elemental identification, and incident energy over the energy range from 100 keV per ion to 15,000 keV per ion. The sensor is shown schematically in Figure 40; the HIT/LOMICS sensor function block diagram is shown in Figure 41.

We consider the HIT sensor first. Four primary data are produced in this sensor. Ions entering the sensor pass through detector A producing a ΔE signal and secondary electrons which generate a START signal. The ions drift across a 7.5-cm region and stop in detector B where their energy, E, is measured, and the secondary electrons produced there generate a STOP signal. The START and STOP signals produced by the respective microchannel plates are fed into a TAC. The SSD signals A, B, and the anticoincidence signal from SSD-C are amplified and run into EVENT LOGIC to select those events to be analyzed in detail. For the detailed analysis, the SSDA output, ΔE , is converted by a log ADC to 5 bits, the SSD-B output, E, is converted to 8 bits, and the TAC output is converted to 10 bits representing TOF. These digitized values (ΔE , E, TOF) are clocked out to the DPU for processing. Every START, SSD-A, SSD-B, SSD-C, and valid event indicator output is accumulated in HMSB scalers and sampled by the DPU every 0.5 seconds. The ΔE and E outputs above various levels are also accumulated in a manner identical to Explorer 45, ATS-6, and VIKING. The DPU is

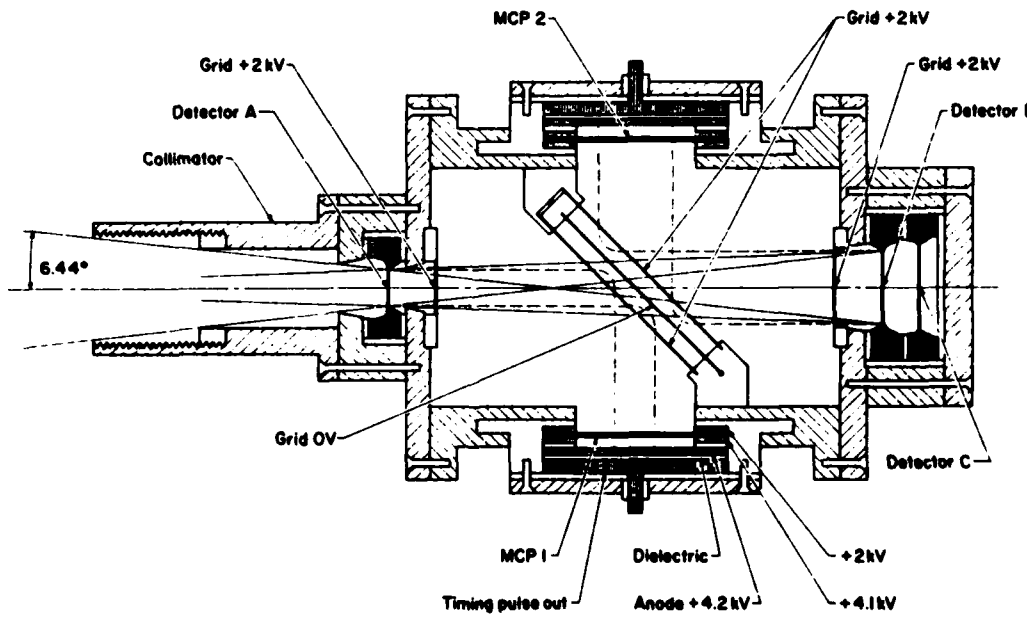


Figure 40. Schematic Diagram of the Heavy Ion Telescope (HIT)

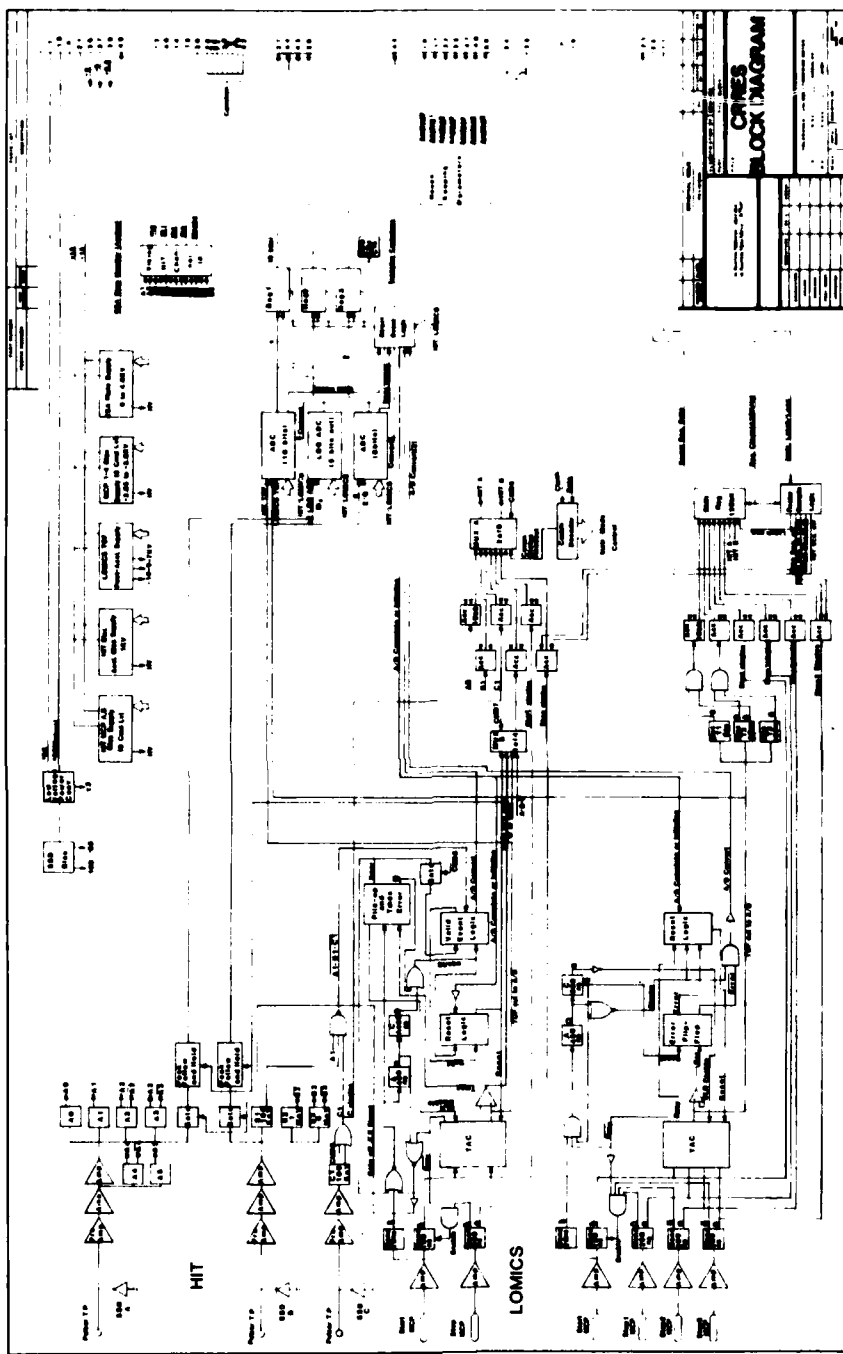


Figure 41. Function Block Diagram for the Low Energy Magnetospheric Ion Composition (LOMICS) and the Heavy Ion Telescope (HIT) Experiments

time shared between the HIT and LOMICS sensors as well as the resident electronics within the HMSB box on a 65.4-sec cycle.

The DPU sends commands to change the HIT / LOMICS modes. It collects the HK data (temperature, voltages, modes, etc.) and inserts them into the telemetry stream.

3.4 Data Processing Unit (DPU) Block Diagram

Two distinct microprocessor-based DPUs support the Mass Composition Instruments. One supports the MICS sensor, DPUA, and the other, the HIT/LOMICS sensors, DPUB. Both are very similar in design, with many of the sensor differences accommodated by software changes only.

The basic MICS DPU (DPUA) function diagram is shown in Figure 42. The interface with the sensor consists of two main sections, a command and control

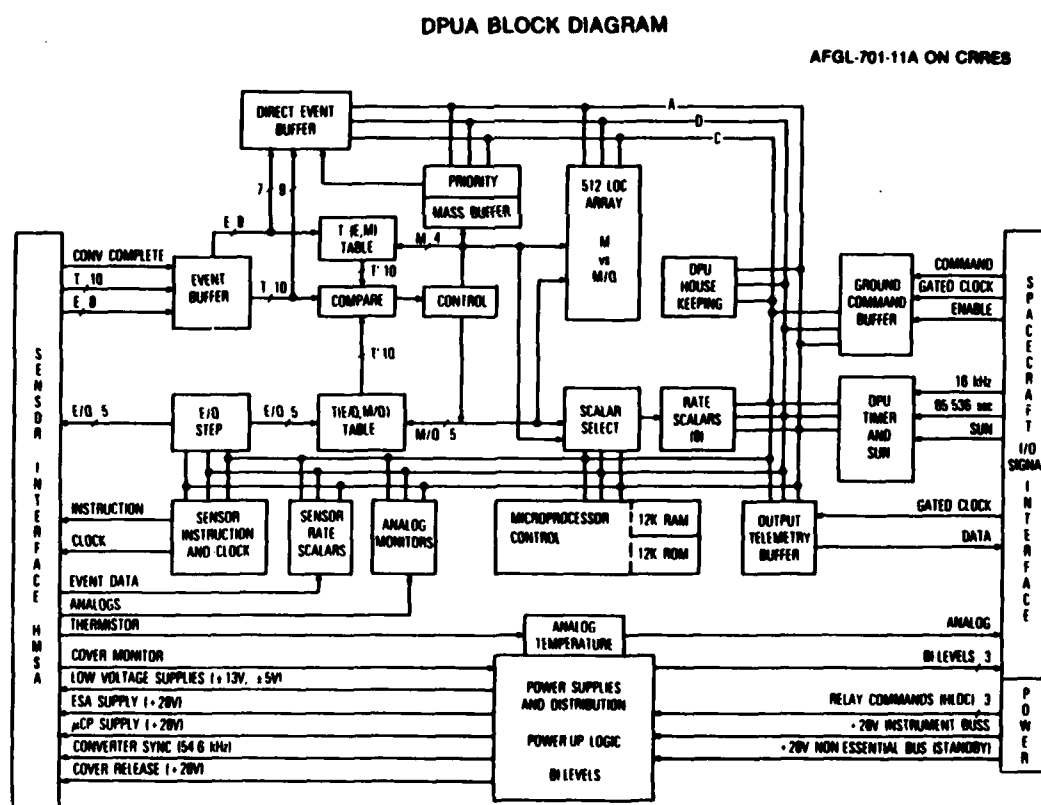


Figure 42. Function Block Diagram for the Data Processing Unit (DPUA) for the Magnetospheric Ion Composition (MICS) Experiment

section and the TOF and E data processing sections. The command and control section generates the E/Q step signals for the MICS, synchronizes the E/Q stepping and sensor mode changes with the DPUA clocks, reads out the MICS HK and event counters, and controls the calibration test sequences.

The TOF and E processing section is the heart of the DPUA from the sensor point of view. The TOF, E, and E/Q digital words are first buffered and TOF and E are compressed. The compressed TOF and E words are presented to a successive approximation look-up table to obtain a mass, M, decision. This decision identifies the ion associated with the TOF and E as corresponding to 1 of 16 mass groups (4-bit value). Similarly, the TOF and E/Q words are presented to a look-up table that identifies the ion as being in 1 of 32 mass per charge, M/Q, groups (5-bit value). The M and M/Q values are used as addresses to storage positions in a RAM which are incremented. The address at the position in the M versus M/Q Scaler RAM (Figure 42) is incremented. The M and M/Q values are presented to look-up tables that determine which, if any, of the 8 RATE SCALERS and 8 FIXED SCALERS are incremented. The M values determine which MASS SCALER is incremented and whether the raw TOF and E data will be selected for transmission as a DIRECT EVENT. This latter choice is based on a priority scheme where the highest priority mass in a time slice is selected. One of eight different priority and scaler selection tables can be chosen by ground command.

The look-up tables for M and M/Q selection are calculated upon command from a set of third order polynomials stored in ROM. These coefficients can be changed by modifying the contents of the appropriate RAM space (using memory load command) that the microprocessor works from (the microprocessor does NOT work out of ROM). Standby power is required to maintain the RAMs once they have been loaded. On the development unit (VIKING satellite unit), one 16 bit digital command word is used for all DPUA commands. These are presently accepted at a 1/sec rate and are reflected in the telemetry stream. The command word is used for all experiment mode configuration, TM format, and internal function control.

The DPUA interface with the spacecraft consists of power lines, clocks, a command line, and data line or lines. The DPUA is synchronized to the satellite TM frame rate. The main power supply for the MICS sensor is in the DPU. All power conversion and regulation, except for the High Voltage Power, is done there.

The HIT/LOMICS, DPUB, function block diagram is shown in Figures 43 and 44. Many of the functions are identical to those in the DPUA. The HIT and LOMICS sensors present nearly identical data formats to the DPUB.

In the HIT mode (Figure 43), the DPUB receives TOF, ΔE , and E from the HMSC box. TOF and E are used to obtain mass, M, as described above for the

**DPUB BLOCK DIAGRAM
HIT MODE**

AFGL-701-11B ON CRRES

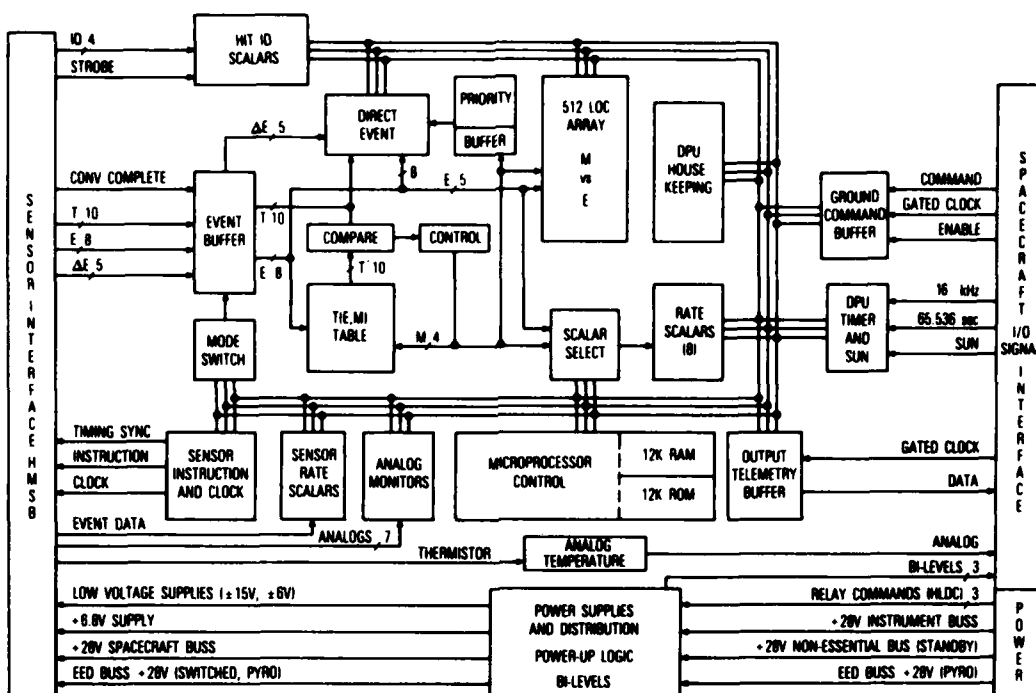


Figure 43. Function Block Diagram for the Data Processing Unit (DPUB) for the Heavy Ion Telescope (HIT)

DPUA. The E is also rescaled to 5 bits, E(5), to act as an address. E and ΔE are used to look up mass also, but as a range. Two values are obtained, M(max) and M(min), which are compared to the M value. If M does not fall into the M(min)-M(max) range, the event is rejected. When an event is accepted, M is used to address a MASS SCALER, and M and E(5) are used to increment an M versus E scaler and select the appropriate RATE and FIXED SCALERS. M is also used to decide if the raw DIRECT EVENT data are to be transmitted, as discussed above for the DPUA.

In the LOMICS mode (Figure 44), the DPUB receives TOF, E/Q, and ID from the HMSCB box. The TOF and E/Q values are presented to a look-up table that identifies the ion as being in 1 of 32 mass per charge, M/Q, groups (5-bit value). Only the first 4 levels of the 16-level M identification are used by the LOMICS mode, and these 4 levels correspond to the 2-bit ID. The ID versus M/Q values are used as addresses to storage positions in RAM (similar to the DPUA), which are incremented. The ID versus M/Q values are presented to look-up tables to

DPUB BLOCK DIAGRAM
LOMICS MODE

AFGL-701-11B ON CRRES

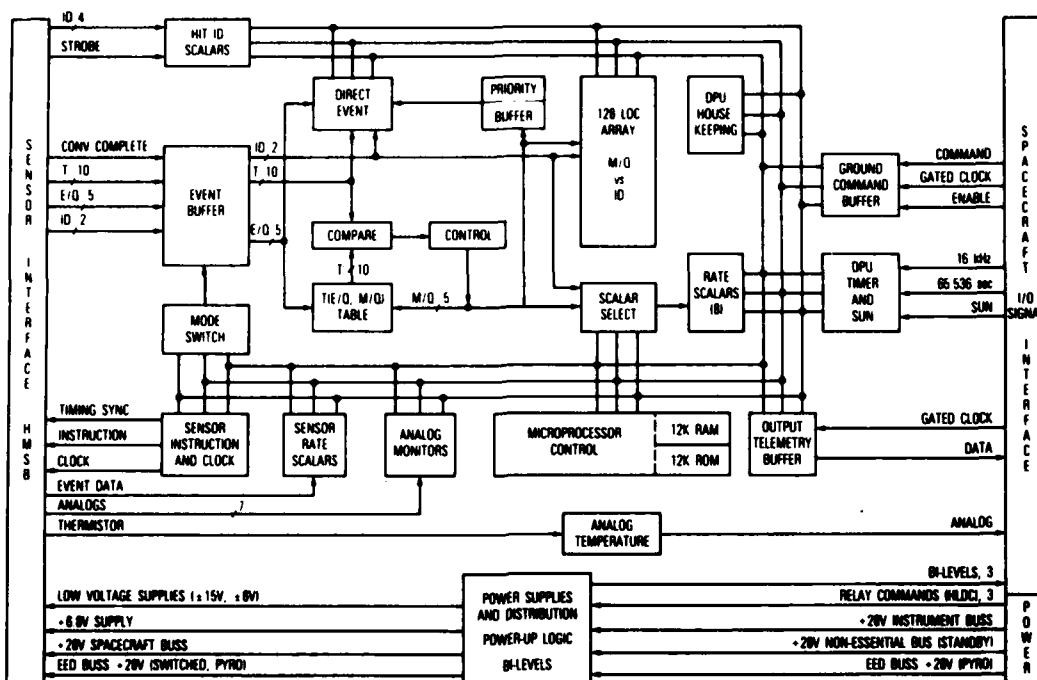


Figure 44. Function Block Diagram for the Data Processing Unit (DPUB) for the Low Energy Magnetospheric Ion Composition (LOMICS) Experiment

determine which, if any, of 6 RATE scalers are incremented. The LOMICS mode will be split into two separate output telemetry formats. LOMICS format 2 will contain LOMICS DIRECT EVENTS and the selection of which event of TOF(10), E/Q(5), ID(2) to place in the TM will be made either on a first-in/first-out basis or with a predetermined priority selection criteria.

The DPUB sends mode commands to the sensor and reads out the HK data as discussed above. It also provides some discrete scalers to support outputs from the HIT sensor analog logic.

Contents

1. Scientific Objectives	141
2. Applications	142
3. Measuring Techniques	143
4. Function Block Diagram	149
Acknowledgments	149
References	151

15. The Low Energy Ion Mass Spectrometer (ONR-307-8-1, 307-8-2)

by

**J.M. Quinn, E.G. Shelley, S.J. Battel,
E. Hertzberg, S. Roselle, and T.C. Sanders**
Lockheed Palo Alto Research Laboratory
Palo Alto, CA 94304

1. SCIENTIFIC OBJECTIVES

The Low Energy Ion Mass Spectrometer (IMS-LO) is designed to measure plasmas that are the sources of radiation belt particles, and to provide data on the origin and acceleration processes of these plasmas. To achieve these objectives, the IMS-LO measures energy and mass spectra covering the ranges of $E/q = 0.1 - 32 \text{ keV/e}$ and M/q from <1 to $>32 \text{ AMU/e}$ with good coverage of pitch angles throughout the orbit.

These data will be used to investigate plasma interaction processes including: (1) the plasma and field conditions that produce ionospheric acceleration, precipitation of energetic particles from the trapped populations, and very-low frequency (vlf) wave generation and amplification; (2) the local time and invariant latitude distributions of ionospheric ion source regions; and (3) the large-scale and small-scale transport and energization processes for the hot plasmas.

2. APPLICATIONS

A series of spacecraft instrumented to measure plasma composition has yielded important results from a wide variety of magnetospheric locations. One of these was the S3-3 satellite, launched in July 1976, that led to the discovery of intense upflowing ionospheric ions at altitudes near $1 R_E$ and the determination of the morphology of these flows. Increase in the ionospheric component of trapped keV ring current ions with storm activity was also established with these data. The S3-3 results are reviewed by Sharp et al.¹

Following S3-3, plasma composition measurements were made on GEOS-1, launched in April 1977 into an eccentric equatorial orbit;² ISEE-1, launched in October 1977;^{3,4} GEOS-2, launched into geosynchronous orbit in July 1978;² PROGNOZ-7, launched into a highly eccentric orbit with 65° inclination in October 1978;⁵ SCATHA, launched into a near-geosynchronous orbit in January 1979;^{4,6} DE-1, launched into a polar eccentric orbit with apogee of $4.6 R_E$ in August 1981;⁷

-
1. Sharp, R.D., Ghielmetti, A.G., Johnson, R.G., and Shelley, E.G. (1983a) Hot plasma composition results from the S3-3 spacecraft, in Energetic Ion Composition in the Earth's Magnetosphere, R.G. Johnson, Ed., TERRAPUB, Tokyo.
 2. Balsiger, H., Geiss, J., and Young, D.T. (1983) The composition of thermal and hot ions observed by the GEOS-1 and -2 spacecraft, in Energetic Ion Composition in the Earth's Magnetosphere, R.G. Johnson, Ed., TERRAPUB, Tokyo.
 3. Sharp, R.D., Johnson, R.G., Lennartsson, W., Peterson, W.K., and Shelley, E.G. (1983b) Hot plasma composition results from the ISEE-1 spacecraft, in Energetic Ion Composition in the Earth's Magnetosphere, R.G. Johnson, Ed., TERRAPUB, Tokyo.
 4. Horowitz, J.L., Chappell, C.R., Reasoner, D.L., Craven, P.D., Green, J.L., and Baugher, C.R. (1983) Observations of low-energy plasma composition from the ISEE-1 and SCATHA satellites, in Energetic Ion Composition in the Earth's Magnetosphere, R.G. Johnson, Ed., TERRAPUB, Tokyo.
 5. Lundin, R., Hultqvist, B., Pissarenko, N., and Zachorov, A. (1983) Composition of hot magnetospheric plasma as observed with the PROGNOZ-7 satellite, in Energetic Ion Composition in the Earth's Magnetosphere, R.G. Johnson, Ed., TERRAPUB, Tokyo.
 6. Johnson, R.G., Strangeway, R.J., Shelley, E.G., Quinn, J.M., and Kaye, S.M. (1983) Hot plasma composition results from the SCATHA spacecraft, in Energetic Ion Composition in the Earth's Magnetosphere, R.G. Johnson, Ed., TERRAPUB, Tokyo.
 7. Shelley, E.G., Balsiger, H., Eberhardt, P., Geiss, J., Ghielmetti, A., Johnson, R.G., Peterson, W.K., Sharp, R.D., Whalen, B.A., and Young, D.T. (1983) Initial hot plasma composition results from the Dynamics Explorer, in Energetic Ion Composition in the Earth's Magnetosphere, R.G. Johnson, Ed., TERRAPUB, Tokyo.

and AMPTE/CCE, launched into an eccentric low latitude ($\sim 5^\circ$) orbit with apogee of $8.8 R_E$ in August 1984.⁸

The contributions of these instruments are too numerous to list here; however, the plasma composition of a large number of magnetospheric regions has now been examined. The data show intricate dependences on local time, radial distance, pitch angle, energy, magnetic storm and substorm activity, and solar cycle. Sufficient information about the plasma morphology and dynamics have been obtained to make an excellent starting point for the modeling goals of CRRES.

Determining the behavior of different ion species in the energy range covered by the IMS-LO instruments is critical to the development of detailed ring current models. A thorough understanding of ring current dynamics will require detailed knowledge of the particle source contributions, transport phenomena, energization processes, and, finally, scattering and loss mechanisms. Although initial attempts to model ring current dynamics cannot await such a comprehensive understanding, the basic components of source, transport, and loss must be represented as accurately as possible. Ion composition data are essential for determining total ion energy density (ring current) and they provide a necessary link in modeling the life of ring current ions.

3. MEASURING TECHNIQUES

The IMS-LO-1 and IMS-LO-2 instruments rely upon the same design that was successfully implemented with previous Lockheed instruments on SCATHA (launched January 1979) and S3-3 (launched July 1976). Each version of the instrument has had improved range of coverage, resolution and operating flexibility.

IMS-LO-1 and IMS-LO-2 are identical instruments mounted at 45° and 75° to the spacecraft spin axis to maximize coverage of fluxes near the magnetic field line direction. Each instrument performs ion composition measurements in the energy per charge range 0.1-32 keV/e and the mass per charge range <1 to >32 AMU/e. The energy range is broken into three contiguous parts, each consisting of 15 energy steps, a coverage of 45 energy steps in all. The three portions of the energy coverage are sampled in parallel by three separate analyzer and sensor heads. After each 15-step sequence, the background counting rate is measured for each sensor head. The mass range (<1 to >32 AMU/e) is covered by 32 steps. Alternatively, the spectrometer can be commanded to sample the high mass range above 16 AMU/e. In addition to ion measurements, each of the two

8. Shelley, E.G., Ghielmetti, A., Hertzberg, E., Battel, S.J., Altwegg-Von Burg, K., and Balsiger, H. (1984) AMPTE/CCE hot plasma composition experiment (HPCE), submitted to IEEE Trans. Remote Sensing.

instruments monitors the background electron flux at four fixed energies. The electron channels are described in Section 3.1.

3.1 Ion Optics

Each of the IMS-LO instruments consists of three parallel analyzer units (or heads) which measure ions in a different portion of the E/q range from 0.1-32 keV/e. One of the analyzer heads is illustrated in Figure 45. Collimated ions enter a crossed electric and magnetic field velocity filter (Wein Filter), pass through an angle-focusing, hemispherical sector, electrostatic analyzer, and are detected by a channel electron multiplier. Details of the optics system follow.

Ions enter the instrument through a collimator with an acceptance cone of approximately 5° full width. Following collimation, the ions enter the crossed electric and magnetic field velocity filter, which, in conjunction with the electrostatic energy analysis, acts as the mass analyzer (MA). The MA consists of a fixed magnetic field and a crossed electric field that is varied according to the value of E/q and M/q being sampled. The fields are oriented so that the electric and magnetic forces on an ion are in opposition, and the electric field is chosen so that there is no net force on an ion of the desired mass and energy, allowing it to pass through the MA in a straight trajectory. The MA magnetic field values in the three heads are nominally fixed at 445, 1211, and 3304 G. The electric field plates of the MA are driven symmetrically and the voltages for a given mass selection scale as the square root of the ion energy as determined by the voltage applied to the electrostatic analyzer (EA) discussed later in this section. The maximum MA plate potentials in the three heads, corresponding to the minimum value of M/q and the maximum value of E/q sampled within each head, are nominally ± 35 , ± 253 , and ± 1850 V for the normal mass range and a factor of four lower for the heavy ion mode. The three heads are driven by a common high voltage power supply and voltage divider network that provides the different ranges required.

Following the velocity filter, ions are bent 180° in a spherical sector EA that is angle focusing and energy dispersive. As with the MA, the EA plates in the three heads are driven by a common power supply and voltage divider network. The ratio between consecutive values of the logarithmically spaced energy steps is approximately 1.14, and there are 15 energy steps within each head. Thus, the values of E/q simultaneously sampled by the three heads are spaced by a factor of approximately seven, with the first head covering from 0.1 - 0.6 keV/e, the second from 0.7 - 4.5 keV/e, and the third from 5 - 32 keV/e. The EA plate separation in the high energy head is reduced from that of the other two heads to achieve the desired energy range without excessively high voltages. After exiting the EA, ions are post-accelerated and enter the channel electron multiplier.

WEIN FILTER ION MASS SPECTROMETER

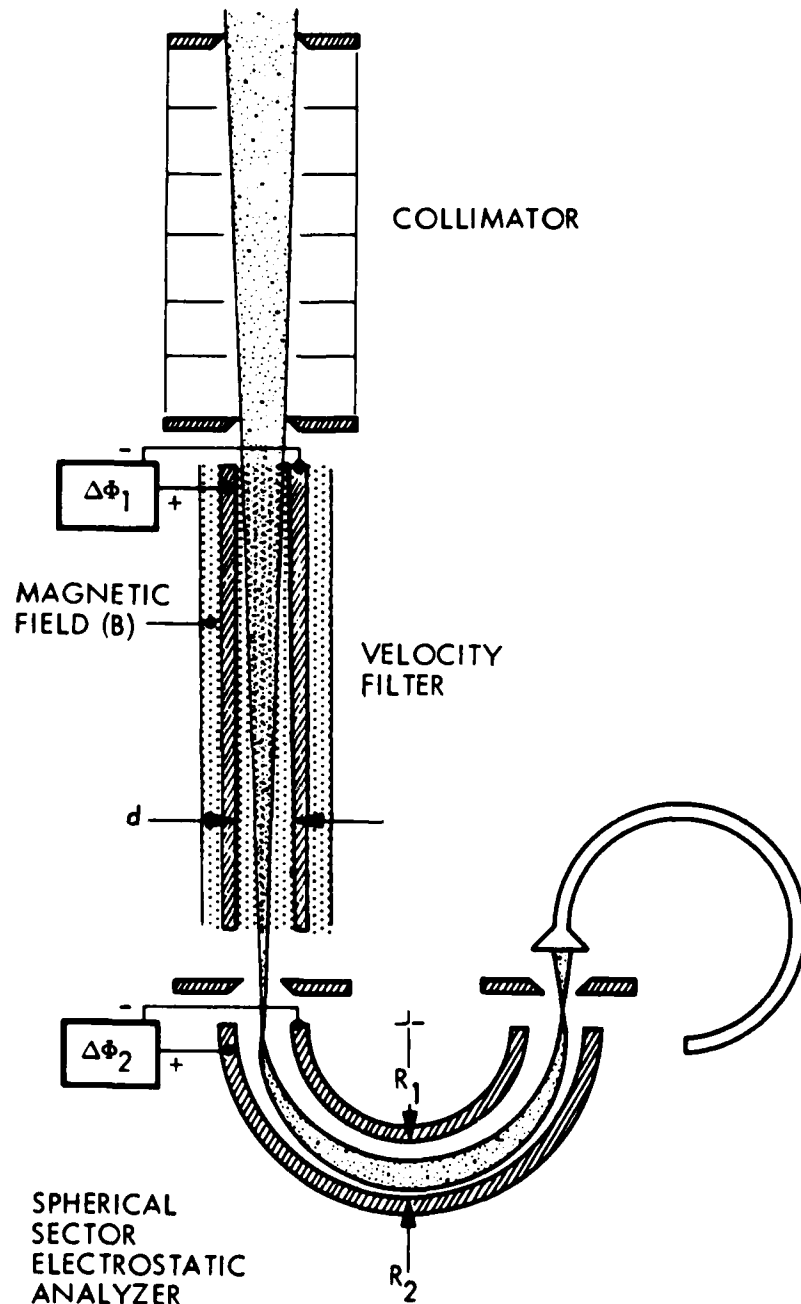


Figure 45. Schematic Illustration of Ion Mass and Energy Analysis Optics for the Low Energy Ion Mass Spectrometer (IMS-LO)

Figure 46 shows peak shapes obtained from the Lockheed mass spectrometer on S3-3. The open circles with error bars are on-orbit data; the dashed line represents inferred peak shapes. Separation of the species is quite good.

The coordinated stepping of the EA and MA is done under digital control in a number of modes as described in Section 3.2. Each sample of a particular mass-energy value requires 64 ms. A 12-ms deadtime at the beginning of each sampling period ensures complete settling of the analyzer power supplies.

Each of the three heads measures background counts in "Energy Step 0," an additional step to the 15 energy steps described above. The background measurement is performed by disabling the MA power supply and setting the EA power supply to step 4. As the MA power supply decays toward zero, the analyzers pass continually higher masses. Following the 12-ms deadtime, the background channel is sampling M/q values well above the ambient ion mass peaks and measures

WEIN FILTER MASS RESOLUTION AT E/Q = 650 V

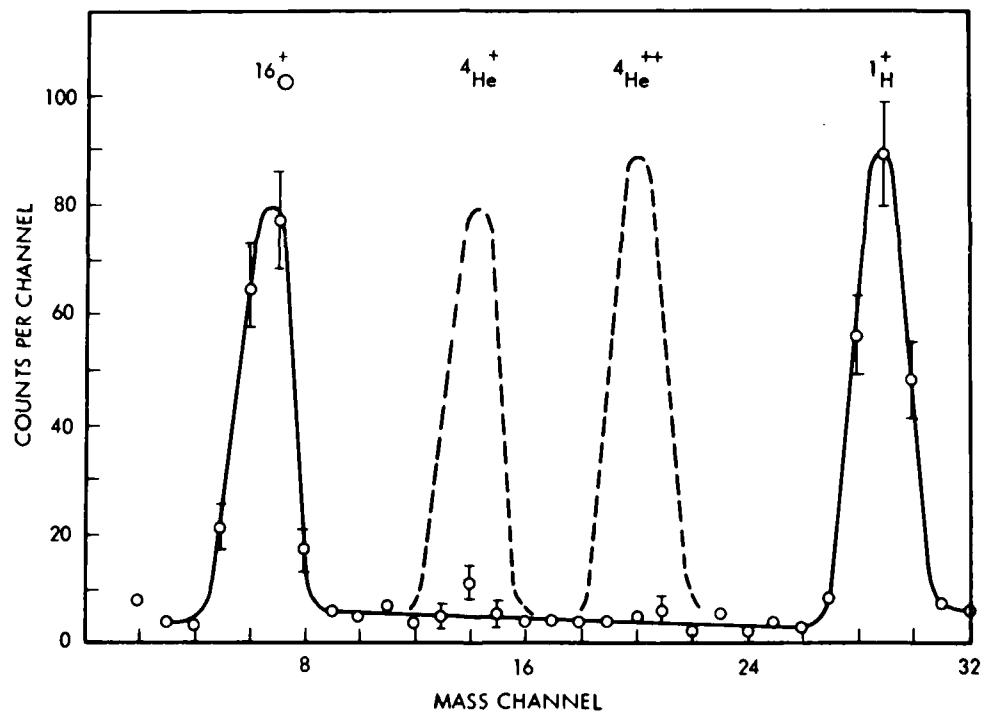


Figure 46. Mass Peak Shapes for the Wein Filter Spectrometer

the instrument background response only. The instrument geometric factors are approximately $4 \times 10^{-4} \text{ cm}^2\text{-ster}$ for the two low energy heads and about one-half this value for the high energy head. $\Delta E/E$ is approximately 10 percent.

3.2 Operating Modes

The two basic submodes of operation are SWEEP and LOCK. In LOCK mode, the instrument locks onto a particular M/q value while stepping in energy. Each of the 15 energy values and background are sampled for 64 ms in each of the three heads, giving a 45-point energy spectrum for a particular species in 1.024 seconds (approximately 12° of spacecraft rotation). The LOCK submode obtains 32 consecutive energy spectra at a fixed mass value (approximately one spacecraft rotation) before moving into the next submode.

In SWEEP submode, the instrument sequentially "sweeps" through the 32-step mass range at each of the 15 energy steps and background. A mass sweep at one energy step requires 2.084 seconds. The entire 32.768-second SWEEP submode obtains a complete sampling of the 32 by 48 mass-energy array (32 by 16 in each of the three heads). As in the LOCK submode, 3 of the 48 energy points are actually background measurements (1 in each head).

The duration of each of the submodes is 32.768 seconds, approximately one spacecraft spin. The submodes may be combined to form the three basic modes of operation: LOCK-ONLY, SWEEP-ONLY, and SWEEP-LOCK. As the names imply, LOCK-ONLY consists only of LOCK submodes, SWEEP-ONLY of SWEEP submodes, and SWEEP-LOCK alternates between SWEEP and LOCK. In either the LOCK-ONLY or SWEEP-LOCK modes, the mass channels used for the LOCK submode are sequentially executed from four values commanded into the instrument memory. These values may select any 4 of the 32 M/q steps corresponding to any four ion species, for instance, H^+ , He^+ , He^{++} , O^+ , or H^+ , O^+ , H^+ , O^+ ; or O^+ , O^+ , O^+ , O^+ . IMS-LO-1 and IMS-LO-2 are commanded independently so that the two instruments can operate in different modes simultaneously.

In addition to the normal range of mass coverage, the instrument can be commanded into a Heavy Ion Mode. In this mode, the MA voltages are reduced by a factor of 4, scaling the M/q coverage upward by a factor of 16.

3.3 Electron Detectors

Each of the IMS-LO instruments contains a set of four broadband, fixed-energy electron detectors that monitor electron fluxes between 50 eV and 25 keV. The $\Delta E/E$ for each detector is 50 percent and the central energies of the four electron channels on IMS-LO-1 and IMS-LO-2 are interleaved, providing a total of eight

channels with central energies from 0.067 to 20 keV. The electron detectors accumulate for 512 ms, providing samples approximately every 6° of spacecraft spin.

Figure 47 schematically illustrates the electron optics for one of the eight detectors. Entering electrons are collimated to a 5° acceptance cone and pass through an aperture that sets the geometric factor. The electrons are then bent

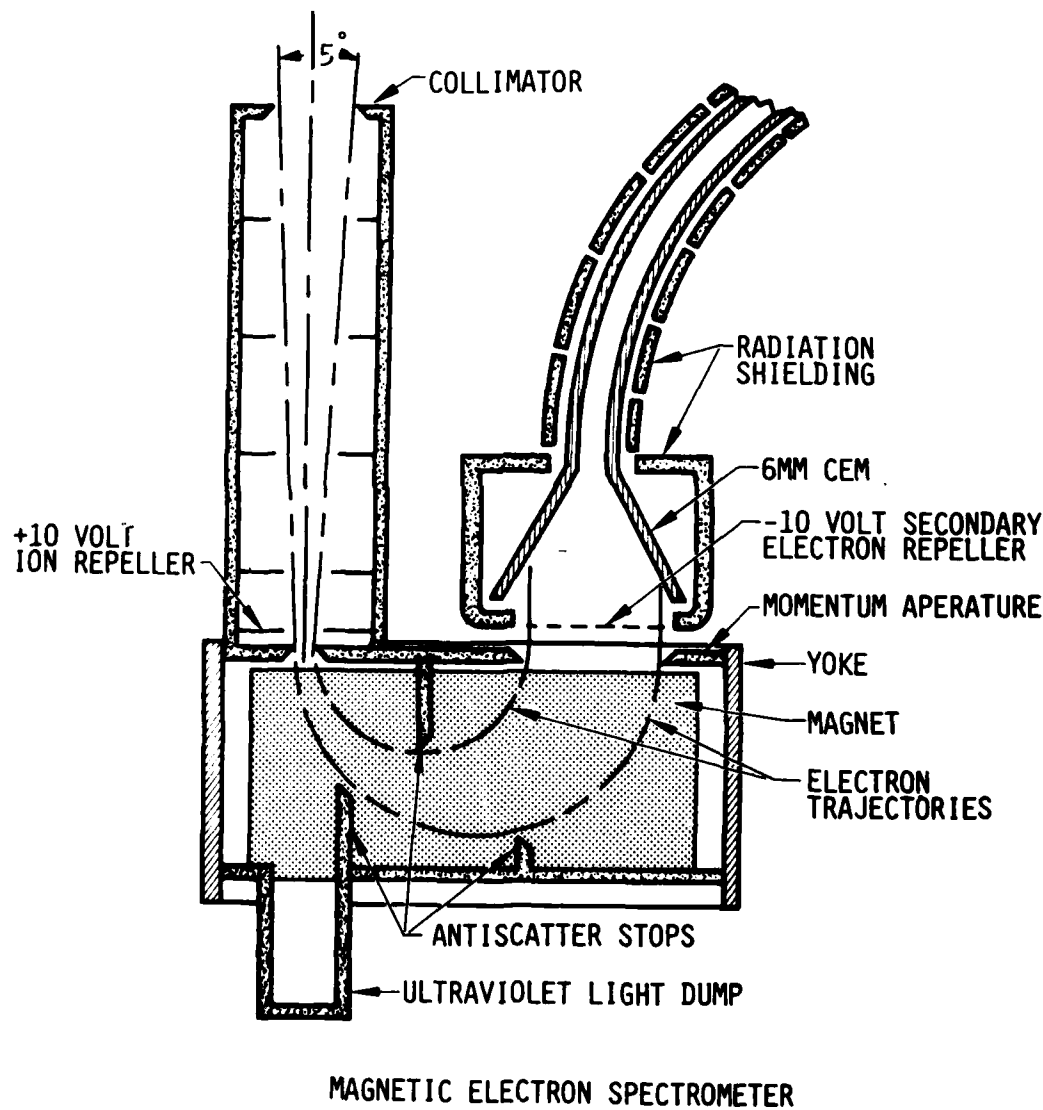


Figure 47. Schematic Illustration of the Electron Detector for the Low Energy Ion Mass Spectrometer (IMS-LO)

180° in a magnetic analyzer and pass through an exit aperture that sets $\Delta E/E$ before entering the channeltron sensor.

4. FUNCTION BLOCK DIAGRAM

The block diagram shown in Figure 48 illustrates the flow of data through the instrument. Counts from the preamp/discriminators increment 16-bit accumulators. Data from the accumulators are read into buffers every 64 ms for ions and every 512 ms for electrons. These data are then log compressed into 8 bits and are sequentially fed into the data stream.

The discriminator threshold for each sensor is set by command to one of four values. A special calibration cycle may be commanded that sequentially steps through the four thresholds while remaining locked on a selected mass step. In addition, the calibration command may optionally enable a pulser that checks each preamp/discriminator and accumulator by injecting pulses at a fixed rate.

The channel electron multiplier bias is command selectable to one of four values to compensate for possible channel multiplier gain degradation. The gain of each channel electron multiplier is periodically determined via the calibration cycle described above.

Acknowledgments

The authors wish to express their appreciation to J.C. Bakke, L.A. Hooker, and V.F. Waltz for their efforts in the design, development, and fabrication of this instrument. We are also deeply indebted to our co-investigators, R.G. Johnson, R.D. Sharp, and R.R. Vondrak for making this instrument (and its predecessors) possible.

This effort was supported by the Office of Naval Research under contract N00014-83-C-0476 and by the Lockheed Independent Research Program.

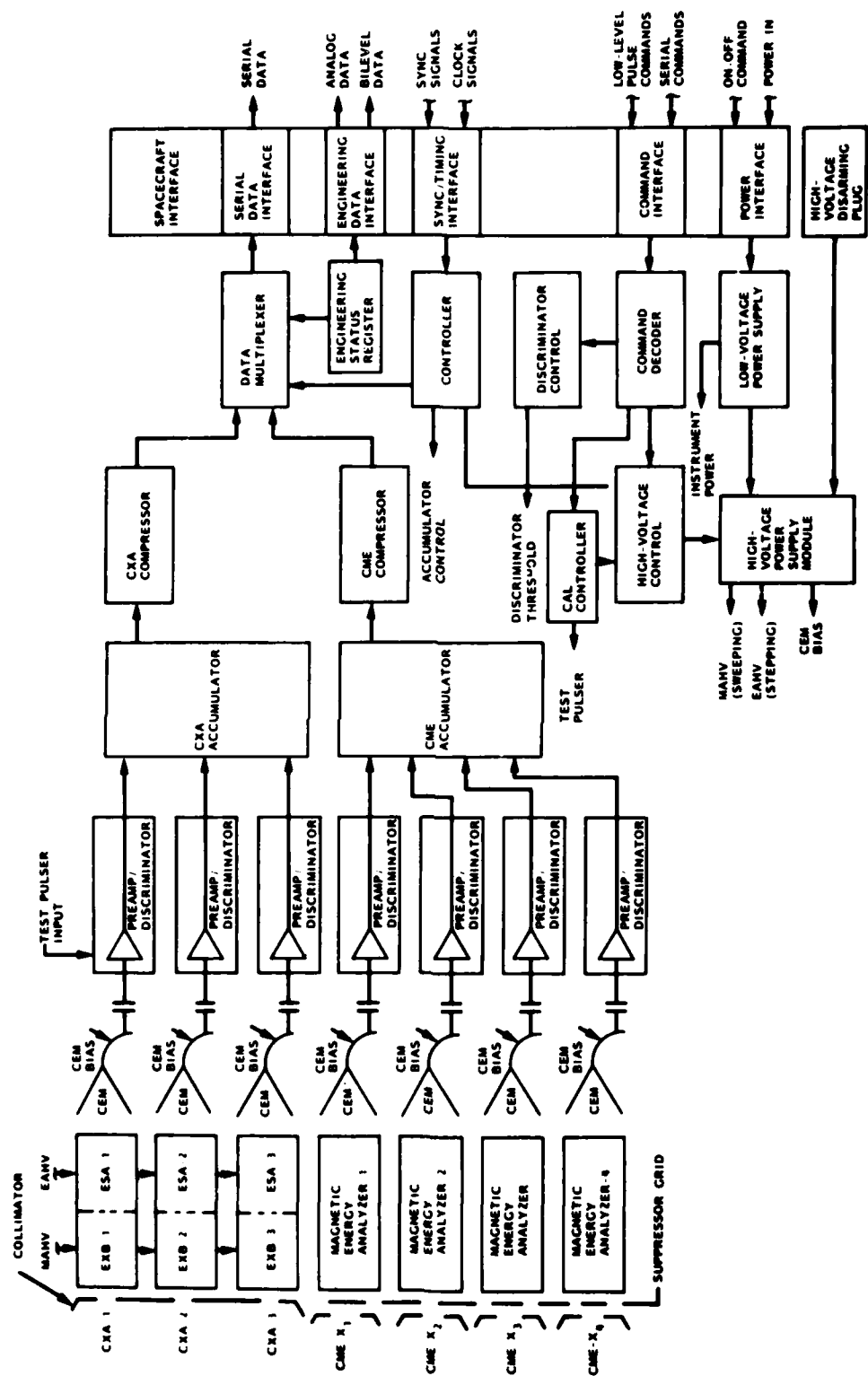


Figure 48. Function Block Diagram for One of the Two Identical Low Energy Ion Mass Spectrometers (IMS-LO)

References

1. Sharp, R.D., Ghielmetti, A.G., Johnson, R.G., and Shelley, E.G. (1983a) Hot plasma composition results from the S3-3 spacecraft, in Energetic Ion Composition in the Earth's Magnetosphere, R.G. Johnson, Ed., TERRAPUB, Tokyo.
2. Balsiger, H., Geiss, J., and Young, D.T. (1983) The composition of thermal and hot ions observed by the GEOS-1 and -2 spacecraft, in Energetic Ion Composition in the Earth's Magnetosphere, R.G. Johnson, Ed., TERRAPUB, Tokyo.
3. Sharp, R.D., Johnson, R.G., Lennartsson, W., Peterson, W.K., and Shelley, E.G. (1983b) Hot plasma composition results from the ISEE-1 spacecraft, in Energetic Ion Composition in the Earth's Magnetosphere, R.G. Johnson, Ed., TERRAPUB, Tokyo.
4. Horowitz, J.L., Chappell, C.R., Reasoner, D.L., Craven, P.D., Green, J.L., and Baugher, C.R. (1983) Observations of low-energy plasma composition from the ISEE-1 and SCATHA satellites, in Energetic Ion Composition in the Earth's Magnetosphere, R.G. Johnson, Ed., TERRAPUB, Tokyo.
5. Lundin, R., Hultqvist, B., Pissarenko, N., and Zachorov, A. (1983) Composition of hot magnetospheric plasma as observed with the PROGNOZ-7 satellite, in Energetic Ion Composition in the Earth's Magnetosphere, R.G. Johnson, Ed., TERRAPUB, Tokyo.
6. Johnson, R.G., Strangeway, R.J., Shelley, E.G., Quinn, J.M., and Kaye, S.M. (1983) Hot plasma composition results from the SCATHA spacecraft, in Energetic Ion Composition in the Earth's Magnetosphere, R.G. Johnson, Ed., TERRAPUB, Tokyo.
7. Shelley, E.G., Balsiger, H., Eberhardt, P., Geiss, J., Ghielmetti, A., Johnson, R.G., Peterson, W.K., Sharp, R.D., Whalen, B.A., and Young, D.T. (1983) Initial hot plasma composition results from the Dynamics Explorer, in Energetic Ion Composition in the Earth's Magnetosphere, R.G. Johnson, Ed., TERRAPUB, Tokyo.
8. Shelley, E.G., Ghielmetti, A., Hertzberg, E., Battel, S.J., Altweegg-Von Burg, K., and Balsiger, H. (1984) AMPTE/CCE hot plasma composition experiment (HPCE), submitted to IEEE Trans. Remote Sensing.

Contents

1. Scientific Objectives	153
2. Applications	154
3. Measuring Techniques	155
4. Function Block Diagram	158
Acknowledgments	158
References	160

16. The Medium Energy Ion Mass Spectrometer (ONR-307-8-3)

by

H.D. Voss, E.G. Shelley, A.G. Ghielmetti, E. Hertzberg,
S.J. Battel, K.L. Appert, and R.R. Vondrak
Lockheed Palo Alto Research Laboratory
Palo Alto, CA 94304

1. SCIENTIFIC OBJECTIVES

The primary objective of the ONR-307 instrument complement is to obtain the necessary data to construct models of the energetic particle and plasma environment of the Earth's radiation belts. The Medium Energy Ion Mass Spectrometer (IMS-HI) measures both the energetic ion composition energy spectra and pitch angle distributions, and the energetic neutral particle energy spectra and pitch angle distributions, with good mass, temporal, spatial, and energy resolution. The IMS-HI is located at an angle of 75° to the spin axis to maximize pitch angle sampling. The ion energy range is approximately 20 to 8000 keV-AMU/q².

The IMS-HI extends the energy range of ion composition measurements well above that of the traditional IMS-LO instruments, which are also part of the ONR-307 Experiment. The principle of the IMS-HI is based on ion momentum separation in a magnetic field followed by energy and mass defect analysis using an array of cooled silicon solid state sensors. The technique of cooling solid state

detectors for high resolution (< 2 keV FWHM) energetic ion measurements in spacecraft instruments was reviewed by Voss et al¹ and was successfully demonstrated in the Stimulated Emission of Energetic Particles (SEEP) experiment on the S81-1 satellite.² The IMS-HI features a parallel architecture with simultaneous mass and energy analysis at relatively high sensitivity.

2. APPLICATIONS

One of the key unknowns of the radiation belt models is the medium energy ($30 < E < 600$ keV) ion composition of the Earth's ring current.³ The reason is that the major part of the ring current plasma falls in the gap between measurements of ion composition by traditional electrostatic and magnetic deflection systems ($E < \sim 30$ keV) and measurements by differential energy loss and total energy deposition in solid state detector instruments ($E > \sim 600$ keV). The IMS-HI incorporates elements of these two traditional techniques to measure directly this important energy/mass range that is not accessible by application of either traditional technique independently.

A knowledge of the ring current ion composition is important from a geophysical standpoint and for obtaining an accurate radiation belt model to correctly predict electronic component and material irradiation effects. It is known, for example, that the irradiation effects on materials such as thermal control surfaces on long-lived satellites is strongly dependent on the mass of the impinging ions. This is particularly important at geosynchronous altitudes.

Lyons and Evans,⁴ Spjeldvik and Fritz,⁵ and Tinsley⁶ have demonstrated the

-
1. Voss, H.D., Reagan, J.B., Imhof, W.L., Murray, D.O., Simpson, D.A., Cauffman, D.P., and Bakke, J.C. (1982) Low temperature characteristics of solid state detectors for energetic x-ray, ion and electron spectrometers, IEEE Trans. Nucl. Sci. 29:164.
 2. Imhof, W.L., Reagan, J.B., Voss, H.D., Gaines, E.E., Datlowe, D.W., Mobilia, J., Helliwell, R.A., Inan, U.S., Katsufakis, J., and Joiner, R.G. (1983) The modulated precipitation of radiation belt electrons by controlled signals from VLF transmitters, Geophys. Res. Lett. 10:8, 615.
 3. Williams, D.J. (1979) Ring current composition and sources, in Dynamics of the Magnetosphere, S.I. Akasofu, Ed., D. Reidel, Dordrecht, Holland, pp. 407-424.
 4. Lyons, L.R., and Evans, D.S. (1976) The inconsistency between proton charge exchange and the observed ring current decay, J. Geophys. Res. 81:6197.
 5. Spjeldvik, W.N., and Fritz, T.A. (1978) Energetic ionized helium in the quiet time radiation belts: Theory and comparison with observations, J. Geophys. Res. 83:654.
 6. Tinsley, B.A. (1978) Effects of charge exchange involving H and H⁺ in the upper atmosphere, Planet. Space Sci. 26:847.

importance of including ions and neutrals other than protons to explain the decay rates observed in the ring current recovery phase. The ions of the ring current, by charge exchange with thermal hydrogen atoms, become neutrals and can thus escape from the Earth's environment. This is a significant loss process of the ring current medium energy ions.⁶ A relatively small percentage of these ions are directed toward the Earth, where they ionize the low latitude atmosphere. These can be used as tracers of the ring current composition.

Low altitude satellite measurements of energetic ions associated with the ring current have been reported by Moritz⁷ and Mizera and Blake;⁸ helium emissions have been measured by Meier and Weller.⁹ Rocket measurements of helium and hydrogen at the equator during the ring current recovery phase were reported by Voss and Smith.¹⁰ Measuring the ring current energetic neutrals over the regions of space covered by the CRRES orbit will provide additional information on the ring current decay rates, spatial geometry, and temporal changes weighted by the appropriate cross sections and neutral hydrogen density. Both the direct medium energy ion composition and the indirect neutral atom tracers can be analyzed with the IMS-HI Spectrometer.

3. MEASURING TECHNIQUES

The IMS-HI is based on ion momentum separation in a magnetic field followed by energy and mass defect analysis using an array of cooled silicon solid state sensors as shown in Figure 49. The entrance collimator defines the ion beam angular resolution using a series of rectangular baffles and includes a broom magnet to reject electrons with energy less than 1 MeV.

At the collimator exit, an annular solid state detector with a central hole measures the integral ion and neutral energy spectrum of the beam supplied to the magnet for momentum analysis. A 7-kG magnetic field then disperses the collimated ions onto a set of six passively cooled (-50°C) silicon surface barrier detectors. The energy range, which varies with ion species, is approximately

-
7. Mortiz, J. (1972) Energetic protons at low equatorial altitudes: A newly discovered radiation belt phenomenon and its explanation, J. Geophys. Res. 38:701.
 8. Mizera, P. F., and Blake, J. B. (1973) Observations of ring current protons at low altitudes, J. Geophys. Res. 28:1058.
 9. Meier, R. R., and Weller, C. S. (1975) Observations of equatorial EUV bands: Evidence for low-altitude precipitation of ring current helium, J. Geophys. Res. 80:2813.
 10. Voss, H. D., and Smith, L. G. (1980) Rocket observations of energetic ions in the nighttime equatorial precipitation zone, Space Res. 20:149.

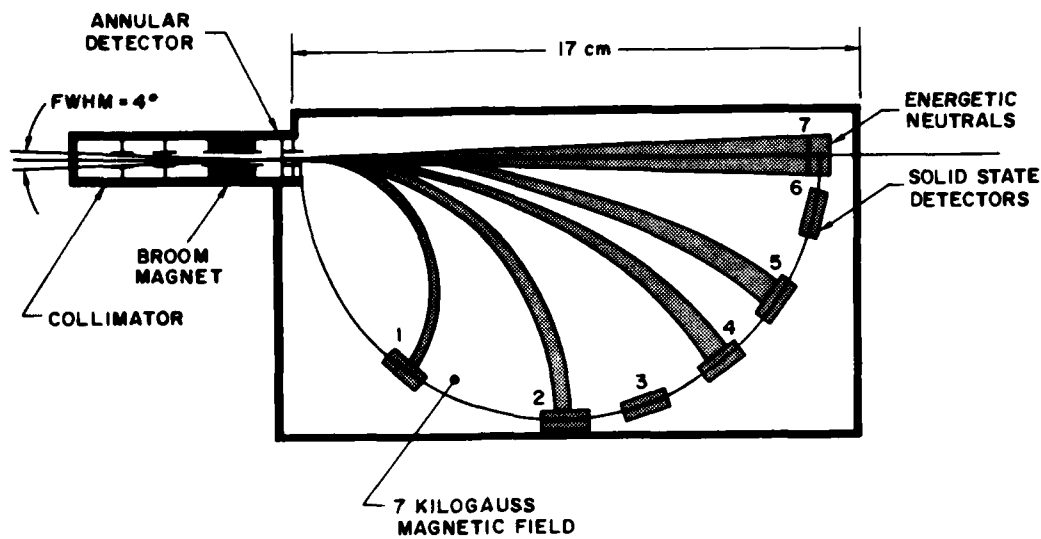


Figure 49. Schematic Diagram of the Medium Energy Ion Mass Spectrometer (IMS-HI)

$EM/q^2 = 20-8000 \text{ keV-AMU}/q^2$. A seventh sensor, located directly in line with the collimator, measures energetic neutrals (ion rejection is approximately 100 MeV-AMU/q).

The instrument features simultaneous mass and energy analysis at relatively large geometrical factors (10^{-3} to 10^{-2} cm^{-2} ster). Simultaneous measurements of charge states can be identified for each M/q^2 and for the same M/q^2 , in some cases, within the solid state detector due to dead zone and mass defect energy losses for equal M/q^2 (for example, O^{++} and He^+). Because of the multisensor design and parallel processing electronics, the dynamic range in flux covered is approximately six orders of magnitude.

A simulation of the ion separation in a 7-kG magnetic field is shown in the position-energy diagram of Figure 50. The image plane, S, is defined as the arc length, beginning at the collimator, for a radius, $R=8 \text{ cm}$. Solid-state detectors 1 - 7 are located at angle, θ , of 40° , 65° , 90° , 115° , 140° , 165° , and 179° , respectively. Solid state detectors 1 - 6 are n-type silicon having either 20 or 40 grams cm^{-2} of gold surface deposit. The neutral and annular detectors are of p-type silicon to improve light rejection and radiation damage sensitivity. The mass defect in solid state detectors results from energy loss of non-ionizing nuclear collisions within the solid that reduce the efficiency of electronic signal generation. The mass defect increases with atomic weight of the nuclei in a well un-

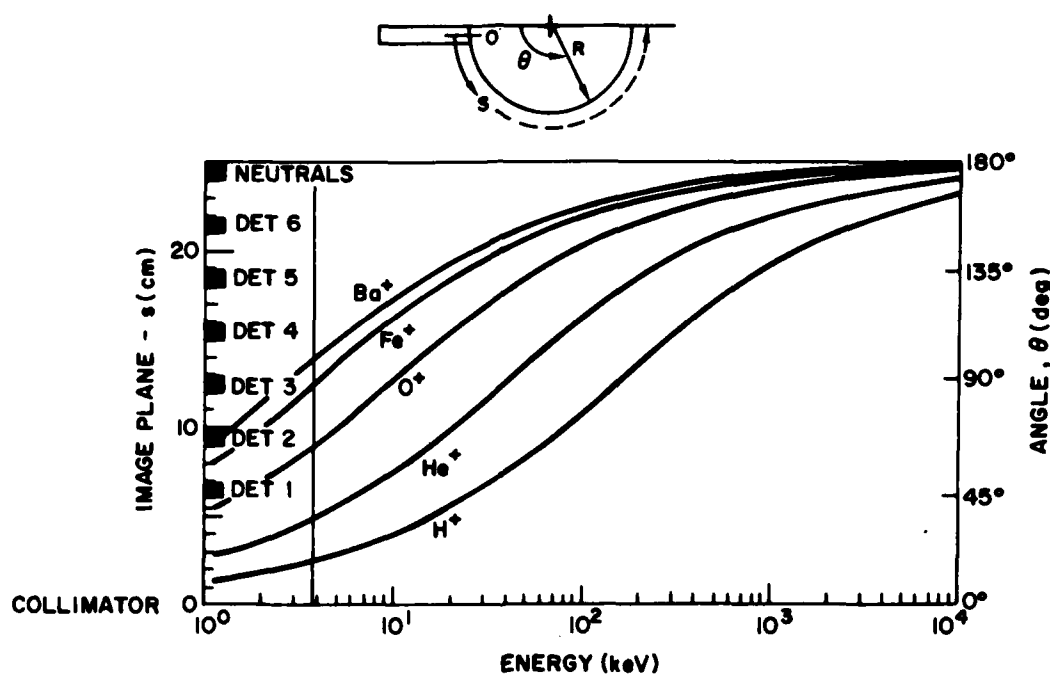


Figure 50. Position-Energy Plot for the Medium Energy Ion Mass Spectrometer (IMS-HI) for Singly Charged Ions in a 7-kG Magnetic Field

derstood way,¹¹ and causes further mass separation, with commensurate energy scatter, for the heavier nuclei.

The magnet section consists of a yoke, pole pieces, and a rare earth permanent magnet. To produce a homogeneous magnetic field of about 7000 G in the 5-mm gap and minimize weight, the best commercially available magnetic material (SmCo5 with 25 MGOe energy product) is used. The yoke completely surrounds the magnetic field, permitting one to reduce the magnetic resistivity in the return flux section and to minimize the magnetic stray fields. Shape and dimensions are optimized to save weight and to assure a uniform magnetic induction anywhere within the yoke. The resultant complex shape necessitates the use of numerical machining methods to meet the weight requirement and design goal of <~100 nT magnetic stray field at a distance of 1 meter. A yoke material (Hyperco 50) that possesses relatively high permeability (2000-4000) at high induction levels (20 kG) was chosen. The design weight of the 7-kG flight magnet assembly is about 5.7 kilograms.

11. Forcinal, G., Siffert, P., and Coche, A. (1968) Pulse height defects due to nuclear collisions measured with thin window silicon surface barrier detector, *IEEE Trans. Nucl. Sci.* (NS-15):475.

4. FUNCTION BLOCK DIAGRAM

A function block diagram of the IMS-HI is shown in Figure 51. Variable pulse height signals from the ion sensors are each routed for analysis to a peak detector circuit and analog multiplexer. Each peak detector circuit is allowed to track and hold the highest peak value for input pulses below the programmable threshold, V_T , and to hold and stop sampling for input pulses above V_T . The sample interval for each detector is 45 μ sec. The read and reset of each peak detector circuit is controlled by the master clock strobes so that a continuous and sequential scan is made of each detector.

Simultaneous with the reset command, the 256-channel analog-to-digital converter is activated, and the resulting digital pulse height (8 bits) is placed on the address bus of the energy look-up table. Also placed on the address bus of the RAM are the 3 bits that specify which detector is being processed. The content of this memory cell (16 bits) is read into the accumulator, incremented by one, and then read back into the memory cell. An address counter is then used to sequentially step through the entire RAM for telemetry readout. A data compressor packs the 16-bit sum into an 8-bit byte for serial interface with the satellite telemetry.

The two basic modes of instrument operation are Mass Lock and Mass Scan. In the Mass Scan mode, each of the seven solid state sensors is pulse height analyzed into 256 levels of which 64 intervals are accumulated in memory and read out every eight seconds. This mode is used to scan all mass peaks within the range of the sensor relative to the background continuum. In the Mass Lock mode, each of the seven solid state sensors is pulse height analyzed into 256 levels, of which four intervals (typically, four ions) are accumulated in memory and read out every half second. This mode is used for making rapid spectral snapshots of four ions as a function of pitch angle. Baseline operation of the instrument will be a toggle mode (32.768 sec) between the Mass Lock mode and the Mass Scan mode.

Acknowledgments

The authors wish to thank T. C. Sanders, D. A. Simpson, L. A. Hooker, and V. F. Waltz for their efforts in the design, development, and fabrication of this instrument. We also deeply appreciate the assistance of R. D. Sharp and Jack Quinn.

This effort was supported by the Office of Naval Research under contract N00014-83-C-0476 and by the Lockheed Independent Research Program.

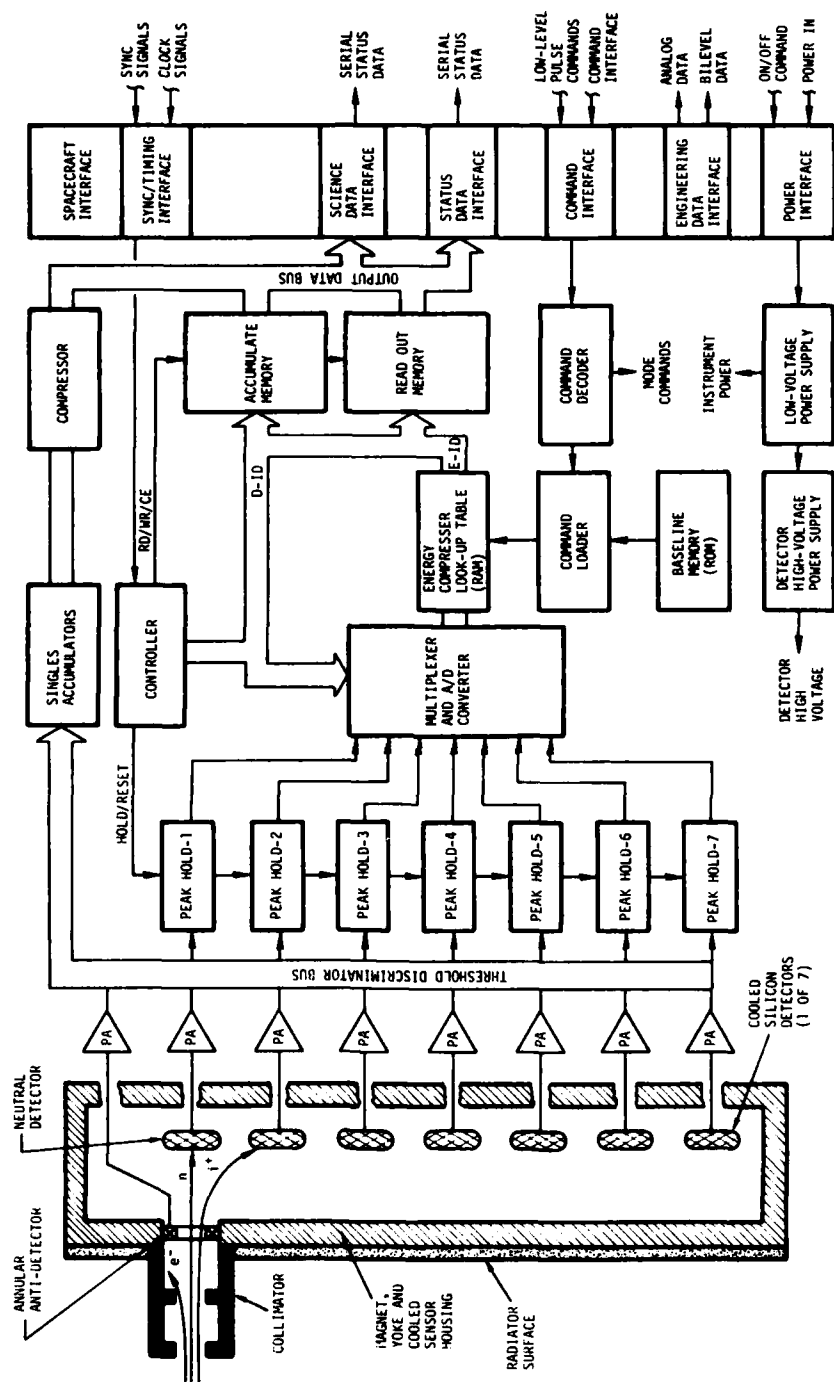


Figure 51. Function Block Diagram for the Medium Energy Ion Mass Spectrometer (IM-S-HI)

References

1. Voss, H.D., Reagan, J.B., Imhof, W.L., Murray, D.O., Simpson, D.A., Cauffman, D.P., and Bakke, J.C. (1982) Low temperature characteristics of solid state detectors for energetic x-ray, ion and electron spectrometers, IEEE Trans. Nucl. Sci. (NS-29):164.
2. Imhof, W.L., Reagan, J.B., Voss, H.D., Gaines, E.E., Datlowe, D.W., Mobilia, J., Helliwell, R.A., Inan, U.S., Katsufakis, J., and Joiner, R.G. (1983) The modulated precipitation of radiation belt electrons by controlled signals from VLF transmitters, Geophys. Res. Lett. 10:8, 615.
3. Williams, D.J. (1979) Ring current composition and sources, in Dynamics of the Magnetosphere, S.I. Akasofu, Ed., R. Reidel, Dordrecht, Holland, pp. 407-424.
4. Lyons, L.R., and Evans, D.S. (1976) The inconsistency between proton charge exchange and the observed ring current decay, J. Geophys. Res. 81:6197.
5. Spjeldvik, W.N., and Fritz, T.A. (1978) Energetic ionized helium in the quiet time radiation belts: Theory and comparison with observations, J. Geophys. Res. 83:654.
6. Tinsley, B.A. (1978) Effects of charge exchange involving H and H⁺ in the upper atmosphere, Planet. Space Sci. 26:847.
7. Mortiz, J. (1972) Energetic protons at low equatorial altitudes: A newly discovered radiation belt phenomenon and its explanation, J. Geophys. Res. 38:701.
8. Mizera, P.F., and Blake, J.B. (1973) Observations of ring current protons at low altitudes, J. Geophys. Res. 28:1058.
9. Meier, R.R., and Weller, C.S. (1975) Observations of equatorial EUV bands: Evidence for low-altitude precipitation of ring current helium, J. Geophys. Res. 80:2813.
10. Voss, H.D., and Smith, L.G. (1980) Rocket observations of energetic ions in the nighttime equatorial precipitation zone, Space Res. 20:149.

11. Forcinal, G., Siffert, P., and Coche, A. (1968) Pulse height defects due to nuclear collisions measured with thin window silicon surface barrier detector, IEEE Trans. Nucl. Sci. (NS-15):475.

Contents

1. Scientific Objectives	163
2. Applications	164
3. Measuring Techniques	165
4. Function Block Diagram	171
References	173

**17. The Experiment for High Energy,
Heavy Nuclei Composition (ONR-604)**

by

J.A. Simpson, M.G. Munoz, and M. Perkins
Laboratory for Astrophysics and Space Research
Enrico Fermi Institute
University of Chicago
Chicago, IL 60637

J.P. Wefel
Department of Physics and Astronomy
Louisiana State University
Baton Rouge, LA 70803

I. SCIENTIFIC OBJECTIVES

The overall scientific objectives of the Experiment for High Energy, Heavy Nuclei Composition (ONR-604) are (a) to obtain new data on the isotopic and elemental composition of high energy, heavy charged particles to assist in understanding the high energy conversion processes in solar flares; (b) to discover observable solar conditions leading to the explosive phase of a solar flare; and (c) to determine the high energy, heavy ion fluxes in selected regions of the magnetosphere to determine its importance as a source of radiation damage and "soft upsets" in electronic devices.

More specifically, the primary objectives of this experiment are: (1) to study

solar flare energy conversion and high energy particle acceleration mechanisms on the Sun; (2) to monitor solar flare particle flux levels; (3) to measure the high energy galactic cosmic ray composition as a "template" for solar flare observations; and (4) to determine the composition of any heavy ions observed in the magnetosphere.

Secondary objectives include: (1) to examine constraints imposed on stellar nucleosynthesis models and their application to the Sun; (2) to determine parameters for models of the origin, acceleration, and propagation of charged particles into the Earth's magnetosphere; (3) to study the access of solar particles into the Earth's magnetosphere; (4) to determine trapping times for particles observed in the magnetosphere; and (5) to verify by space flight the new technology embodied in the solid-state position sensing detectors.¹

2. APPLICATIONS

Review papers of the current status of heavy nuclei composition measurements are in McGuire,² Mewaldt,³ and Simpson.⁴ For further details, see also Adams et al.,⁵ Dietrich and Simpson,^{6,7} and Anglin et al.⁸

-
1. Lamport, J.E., Mason, G.M., Perkins, M.A., and Tuzzolino, A.J. (1976) A large area circular position sensitive Si detector, Nucl. Instr. and Methods 134:71.
 2. McGuire, R.E. (1983) The composition, propagation and acceleration of energetic solar particles: A review of United States Research 1979-1982, Rev. Geophys. Space Phys. 21:305.
 3. Mewaldt, R.A. (1980) Spacecraft measurements of the elemental and isotopic composition of solar energetic particles, in Proc. Conf. Ancient Sun, R.O. Pepin, J.A. Eddy, and R.E. Kerrill, Eds., pp. 81-101.
 4. Simpson, J.A. (1983) Elemental and isotopic composition of the galactic cosmic rays, Ann. Rev. Nucl. Part. Sci. 33:33.
 5. Adams, J.H., Jr., Silberberg, R., and Tsao, C.H. (1981) Cosmic ray effects on microelectronics, Part I: The near-Earth particle environment, NRL Memorandum Report 4506.
 6. Dietrich, W.F., and Simpson, J.A. (1979) The isotopic and elemental abundances of Neon nuclei accelerated in solar flares, Astrophys. J. Lett. 231:L91.
 7. Dietrich, W.F., and Simpson, J.A. (1981) The isotopic composition of Magnesium nuclei in solar flares, Astrophys. J. 245:L41.
 8. Anglin, J.D., Dietrich, W.F., and Simpson, J.A. (1977) Associations with large ³He enrichments, Proc. 15th Internat'l. Cosmic Ray Conf. Plovdiv 5:43.

3. MEASURING TECHNIQUES

Figure 52 shows a schematic diagram of the cross-section of the charged particle telescope. To achieve the high mass resolution needed for isotopic separation of heavy ions, the trajectory of each charged particle entering the acceptance cone of the telescope must be measured, both to correct the path length in the other detectors and to determine the arrival direction of the particles from space. Position-sensing detectors (PSDs) developed and fabricated at the University of Chicago measure the trajectory (Figure 53). As shown in the figure, the PSD collects the charge liberated by the passage of the particle with a series of gold strips on its top surface. This signal is read out through a resistive divider network and compared with the total signal from the detector, obtained from the charge collected on the back surface contact, to obtain one coordinate of the point of incidence of the particle. Two sets of PSDs (three per set for redundancy) are used in the telescope to obtain the trajectory of the particle. Calibration of this system with accelerator particles shows that the position can be measured to < 0.1 mm, and the angle of incidence of the particle determined to $< 1^\circ$.

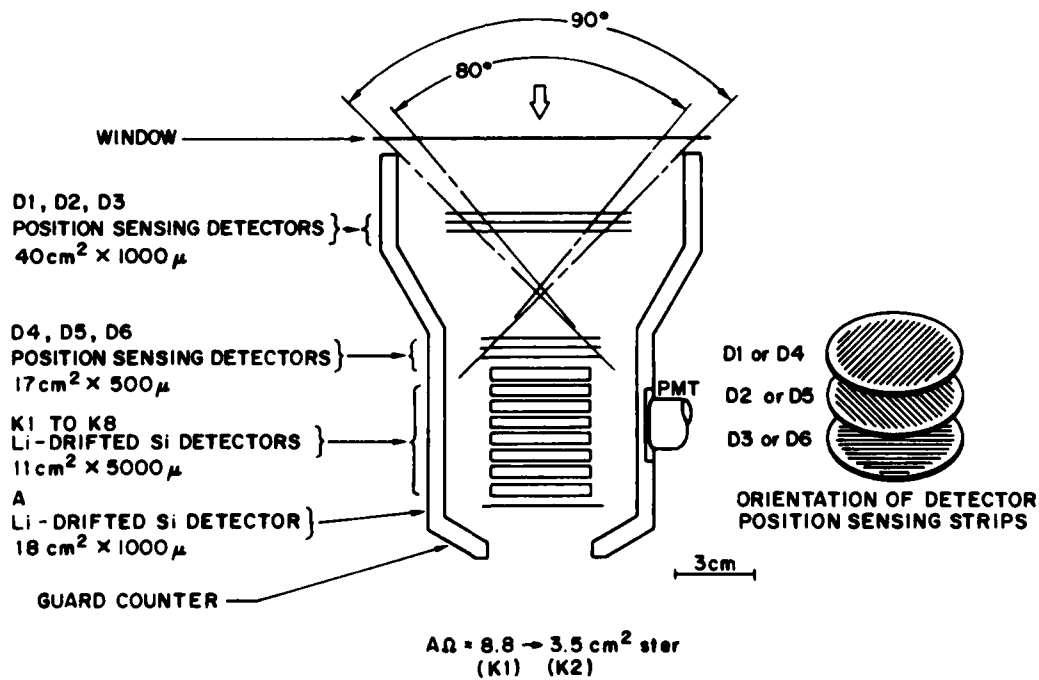


Figure 52. Schematic of the Cross Section of the Charged Particle Telescope in the Experiment for High Energy, Heavy Nuclei Composition

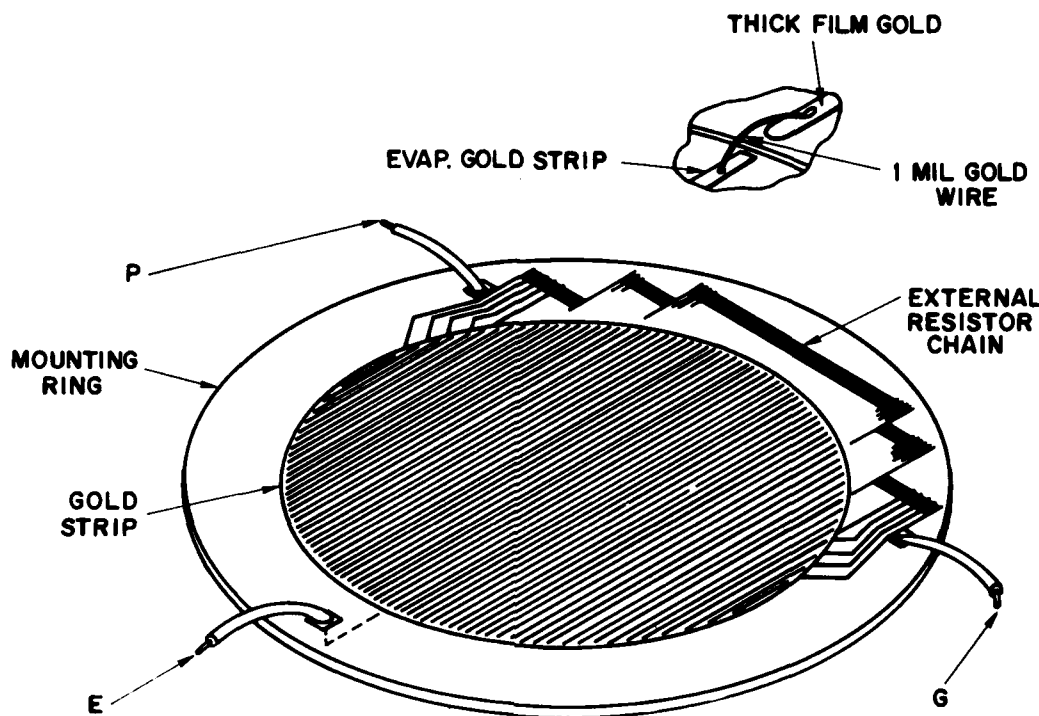


Figure 53. Schematic of the Position Sensing Detector

The charge and mass of each particle is determined by the well known technique of multiple dE/dx versus residual energy using the measurements provided by the stack of high quality, 5-mm-thick lithium-drifted silicon detectors, corrected for the trajectory of the individual particle. For this analysis, the particle must come to rest within the instrument, which determines the energy range for studying each type of particle. As shown in Figure 52, the entire stack is surrounded by a scintillator guard counter in anticoincidence to eliminate out-of-geometry events and to eliminate particles that exit from the side of the apparatus. A ground-commandable operations mode provides detailed analysis of proton and alpha particle flux levels. Thus, complete measurements can be obtained for any particle population observed.

To separate isotopes for elements as heavy as nickel, the dE/dx and residual energy signals must be measured to a precision level of 0.1 percent. This stringent constraint has been met by developing exceptionally linear, highly stable electronic circuits to analyze the signals from each detector. Each analysis chain is individually calibrated, and the entire instrument performance has been evaluated

with high energy heavy ion beams obtained from the Lawrence Berkeley Laboratory Bevalac accelerator.

The performance of each analysis chain is monitored during flight by an on-board calibrator that sends a sequence of 2000 pulses spanning the entire range of signal sizes. Further in-flight calibration and normalization are provided by measurement of galactic cosmic ray events. For these high precision measurements, the temperature must remain stable and constant to within $\sim 3^{\circ}\text{C}$ over the orbit. Consequently, the instrument power must be on during 100 percent of the orbital period.

Because the anticoincidence scintillator guard subtends a large solid angle and is used in the instrument logic, it must be shielded from the high counting rates induced by electrons trapped in the magnetosphere. Passive shielding to eliminate $< 4\text{ MeV}$ electrons is provided by an AZ31B magnesium shield and a tantalum collar. The lower part of the scintillator is located well within the instrument package and is surrounded on five sides by electronic modules which offer additional shielding. The backward moving particles are shielded additionally by the space-craft structure.

For further protection against accumulated radiation damage to the detectors D1, D2, and D3 (where the average geometrical factor is $87\text{ cm}^{-2}\text{-ster}$), a 3-mm external aluminum window shield is placed over the telescope. This shield lowers the magnetospheric integrated proton and electron radiation doses for detectors D1, D2, and D3 below their tolerance threshold while moving slightly upwards the energy intervals for measuring the heavy particles, the main objective of the experiment.

The instrument also measures protons and alpha particles over the energy range 25-119 MeV. In quiet regions of space, a priority system ensures that the heavy nuclei are analyzed in preference to protons and alphas. In regions of high background radiation, a commandable heavy particle "normal mode" is invoked. This raises the thresholds on the detectors D1 through D6 to suppress the high firing rates induced by trapped protons and electrons while still permitting the rare heavy ions to be analyzed. In normal mode, the "proton mode" thresholds of detectors D1 through D6 are increased by a factor of 5.8 and, as a consequence, the instrument becomes practically insensitive to protons.

Table 19 gives a resume of the ONR-604 vital statistics. Table 20 gives a summary of telescope geometry data and counting rate measurements. The left portion shows the maximum incident angle (θ_m) from D1 to the bottom of the indicated detector, the geometrical factor through the window to the bottom of each detector, and the proton energy needed at 0° to penetrate the indicated detector (see Figure 52). The right portion lists the instrument counting rates, where the name refers to the detector where the particle comes to rest; the particle deter-

Table 19. Experiment for High Energy, Heavy Nuclei Composition: Vital Statistics

Weight	32 (+1, -0) lbs
Volume: Package and Telescope	12.0 x 17.0 x 11.75 in.
Viewing: a) Direction	Telescope Axis Normal to S/C Spin Axis
b) Cone (unobstructed)	93° (Full Angle)
Geometrical Factor	90 to 3 cm ² -ster
Power	6.0 Watts, Average; Less than 8.0 Watts, Peak
Bit Rate	360 Bits/Readout (0.512 sec readout; 750 b/s at Interface)
Operating Duty Cycle	100%
Energy Range (Isotopes)	25-570 MeV/Nucleon
Charge Range For Isotopic Separation	Hydrogen to Nickel
Mass Resolution at Iron	$\sigma \sim 0.22$ AMU

mining the indicated rate; and the energy interval corresponding to that rate. P1, P2, and P3 are used in the internal logic, and their counting rates provide the normalization for the heavy nuclei that are pulse height analyzed. The exact energy intervals for the different counting rates must be determined by detailed Monte Carlo studies that include all of the inactive material (detector rings, holders, hardware, etc) around the telescope within the anticoincidence scintillator. Finally, each detector's singles counting rate is recorded to monitor detector performance and background levels.

The highest quality isotopic data is obtained for particles stopping in K2 and below. However, the telescope can also measure particles--

- (a) stopping in K1,
- (b) stopping in D2-D6, or
- (c) penetrating K8.

For (a) and (b), the signal from the E contact of the PSDs provides energy loss information. For events stopping in D2 or D3, the path length uncertainty is given by $\sec \theta$ where θ is the maximum angle through the window = 69° for D2,

Table 20. Experiment for High Energy, Heavy Nuclei Composition: Telescope Geometry and Counting Rates

Detector	θ_m (deg)	A_g (cm ² -sr)	E_p (MeV)	Rate	Particle	ΔE (proton mode) (MeV)
Window	--	379.4	--			
D1	--	93.6	28.3	D1	Protons	24.8- 44.5
D2	87.1	86.6	31.7	D2	"	28.3- 48.2
D3	84.1	80.0	35.1	D4	"	35.1- 43.9
D4	50.0	16.3	36.6	D5	"	36.6- 45.5
D5	47.9	14.9	38.5	K1	"	40.0- 59.4
D6	46.0	13.7	40.0	K2	"	52.0- 70.6
K1	39.2	7.5	52.0	K3	"	62.1- 79.9
K2	36.7	6.4	62.1	K4	"	71.2- 88.5
K3	34.4	5.5	71.2	K5	"	79.3- 96.5
K4	32.4	4.8	79.3	K6	"	87.0-103.5
K5	30.6	4.1	87.0	K7K8	"	94.0-116.9
K6	28.9	3.6	94.0	A	"	107.5-275
K7	27.4	3.2	100.8	P3	"	24.8-275
K8	26.1	2.8	107.5	P2	⁴ He	42 -105
A	--	2.8	108.5	P1	²⁴ Mg	127 -352

Note the large geometrical factor for events in D1, D2, and D3.

which gives a spread of a factor of 2.8. Thus, D1, D2, and D3 analysis can separate protons and helium, but no heavier elements. For particles stopping in D4, the spread is reduced to a factor of 1.44. For particles stopping in D5-K1, trajectory information is available, and elemental separation is limited only by the

quality of the E signals from the PSDs. In fact, there is even some isotopic capability for these events. Finally, the chemical composition of events penetrating the entire stack can be studied over a limited energy interval.

Figure 54 shows the incident kinetic energy intervals in the telescope corresponding to detector penetration ranges (essentially equal to the energies triggering the low thresholds in proton mode) for isotopes H¹ through Ni⁵⁹. For every isotope, the inclined lines connect the points for zero incidence angle (bottom) with the points at 30° incidence angle (top).

The ONR-604 has been calibrated in July 1977, April 1978, and July 1979 with beams of C, Ne, Ar, and Fe particles (with energies such that the particles stopped in the telescope) accelerated at the Bevatron/Bevalac of the Lawrence Berkeley Laboratory. A final calibration, which will also include protons and helium nuclei, will be carried out at this facility for integration before delivery.

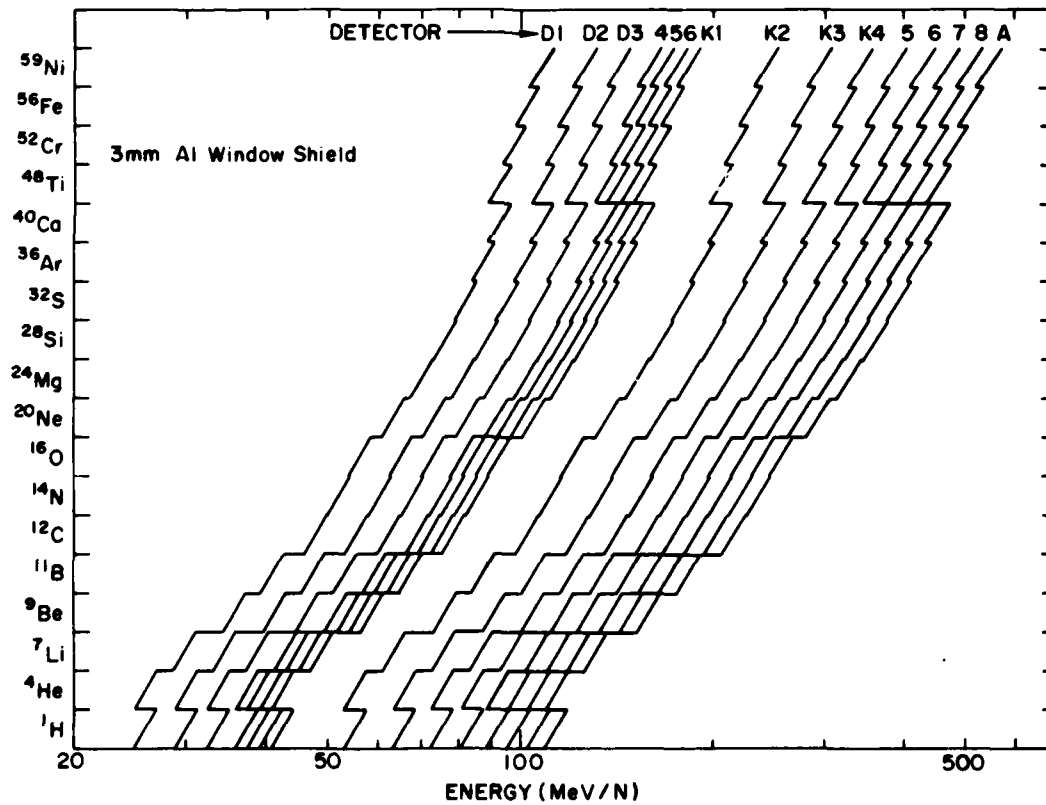


Figure 54. Kinetic Energy Intervals for Given Detector Penetration Ranges for Isotopes H¹ Through Ni⁵⁹

4. FUNCTION BLOCK DIAGRAM

Figure 55 is a function block diagram of the instrument electronics. Besides measuring pulse height analysis (PHA), the instrument has internal accumulators that count and store both single-detector counting rates and coincidence counting rates (see Table 20); thus, the absolute sampling rate and the absolute flux levels can be deduced. A priority system ensures that the rare events are preferentially analyzed and stored. A ground commandable operations mode is provided for the detailed analysis of proton and alpha particle flux levels.

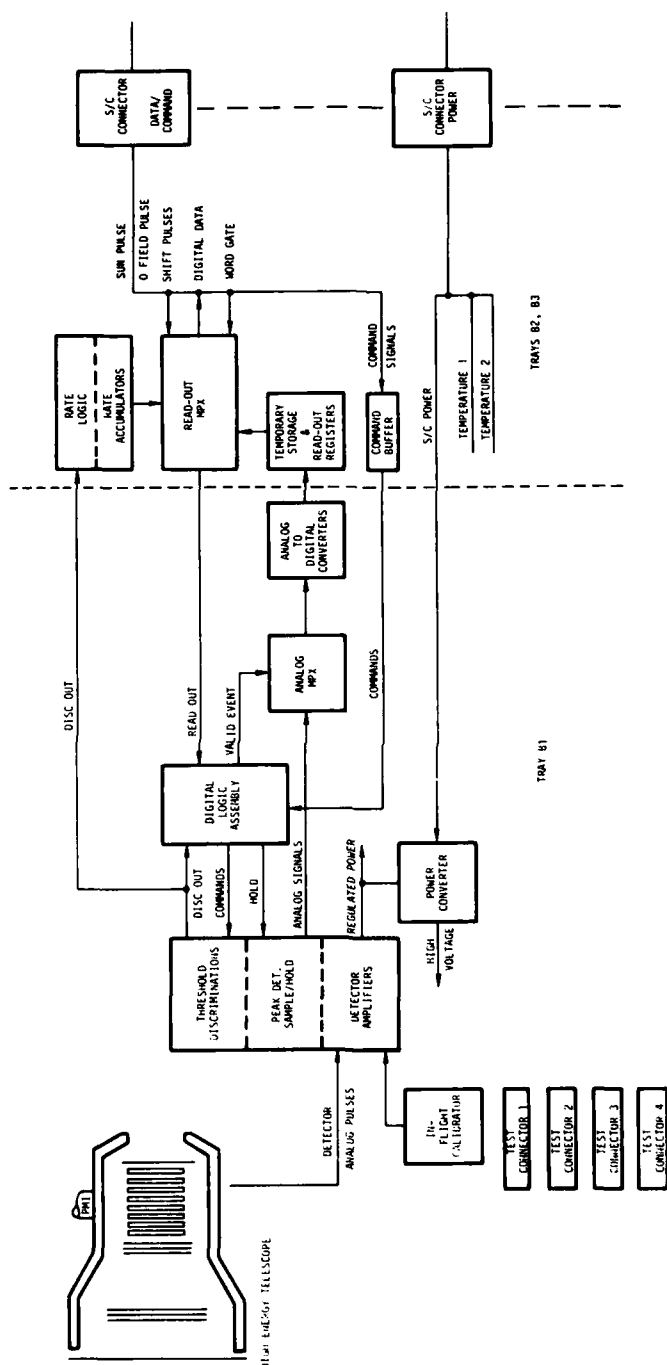


Figure 55. Function Block Diagram for the High Energy Heavy Nuclei Composition Experiments

References

1. Lampert, J.E., Mason, G.M., Perkins, M.A., and Tuzzolino, A.J. (1976) A large area circular position sensitive Si detector, Nucl. Instr. and Methods 134:71.
2. McGuire, R.E. (1983) The composition, propagation and acceleration of energetic solar particles: A review of United States Research 1979-1982, Rev. Geophys. Space Phys. 21:305.
3. Mewaldt, R.A. (1980) Spacecraft measurements of the elemental and isotopic composition of solar energetic particles, in Proc. Conf. Ancient Sun, R.O. Pepin, J.A. Eddy, and R.B. Berrill, Eds., pp. 81-101.
4. Simpson, J.A. (1983) Elemental and isotopic composition of the galactic cosmic rays, Ann. Rev. Nucl. Part. Sci. 33:33.
5. Adams, J.H., Jr., Silberberg, R., and Tsao, C.H. (1981) Cosmic ray effects on microelectronics, Part I: The near-Earth particle environment, NRL Memorandum Report 4506.
6. Dietrich, W.F., and Simpson, J.A. (1979) The isotopic and elemental abundances of Neon nuclei accelerated in solar flares, Astrophys. J. Lett. 231:L91.
7. Dietrich, W.F., and Simpson, J.A. (1981) The isotopic composition of Magnesium nuclei in solar flares, Astrophys. J. 245:L41.
8. Anglin, J.D., Dietrich, W.F., and Simpson, J.A. (1977) Associations with large ^3He enrichments, Proc. 15th Internat. Cosmic Ray Conf. Plovdiv 5:43.

Contents

1. Scientific Objectives	175
2. Application	176
3. Measuring Techniques	176
4. Function Block Diagram	178
References	180

18. The Space Radiation Dosimeter (AFGL-701-2)

by

D.A. Hardy
Air Force Geophysics Laboratory
Space Physics Division
Hanscom AFB, MA 01731

F. Hanser and B. Sellers
Panametrics, Inc.
Waltham, MA 02154

I. SCIENTIFIC OBJECTIVES

The primary purpose of the Space Radiation Dosimeter is to measure the radiation dose from both electrons and protons as well as the number of nuclear star events occurring behind four different thicknesses of aluminum shielding. In addition, it provides some information on the integral flux of electrons and protons at energies above the thresholds defined by the shields. The experiment will provide information on the relationship between the flux of high energy particles incident to the spacecraft and the actual radiation dose to which microelectronic components are exposed. This information is necessary for determining the relationship between variations in the Earth's radiation belts and the behavior and lifetime of microelectronic components.

2. APPLICATION

The basic measurement technique is to determine the amount of energy deposited in a simple solid state detector from particles with sufficient energy to penetrate an omnidirectional aluminum shield of known thickness. Numerous detectors of this type have been flown since the early 1960s.^{1, 2, 3, 4, 5} Most of these, however, have concentrated on measuring the integral flux of particles above the threshold rather than the dose. Only recently have results been reported for instruments that measure the dose from all types of radiation.⁶

3. MEASURING TECHNIQUES

Figure 56 is a schematic drawing of one of the four sensors of the Space Radiation Dosimeter.⁷ The active measuring element is a solid state p-i-n diffused junction silicon semiconductor with a guard ring. The specific devices are from the YAG series manufactured by EG & G, Inc. With these devices, we are able to set a threshold of 50 keV for the energy deposition, allowing us to detect both the high energy particles and most of the bremsstrahlung produced in the shield without compromising on orbit lifetime. Although many detectors in the past have used "volume"-type devices (detection area dimensions comparable with device thickness), the devices we use are of the planar type (detection area dimension larger than thickness). This choice most nearly models real microelectronic components that are primarily planar.

Each device is mounted behind a hemispheric aluminum shield. The aluminum

-
1. Mozer, F.S., Elliott, D.D., Mihalov, J.D., Paulikas, G.A., Vampola, A.L., and Freden, S.C. (1963) Preliminary analysis of the fluxes and spectrums of trapped particles after the nuclear test of July 9, 1962, J. Geophys. Res. 68:641.
 2. Paulikas, G.A., and Freden, S.C. (1964) Precipitation of energetic electrons into the atmosphere, J. Geophys. Res. 69:1239.
 3. Paulikas, G.A., Blake, J.B., and Imamoto, S.S. (1975) ATS energetic particle radiation measurement at synchronous altitude, IEEE Trans. Aerospace and Electronic Systems (AES-11) 6:1138.
 4. Gary, S.A., and Cashian, R.E. (1971) Solar Proton Monitor for TIROS-M and ITOS Spacecraft, COM-73-10138.
 5. Grubb, R.M. (1975) The SMS/GOES Space Environment Monitor Sub-System, NOAA TM ERL SEL-42.
 6. Pruett, B.G. (1980) Comparison of DMSP and NTS-2 dosimeter measurements with predictions, J. Spacecraft 17:270.
 7. Sellers, B., Kelliher, R., Hanser, F.A., and Morel, P.R. (1981) Design, Fabrication, Calibration, Testing and Satellite Integration of a Space Radiation Dosimeter, AFGL-TR-81-0354, AD A113085.

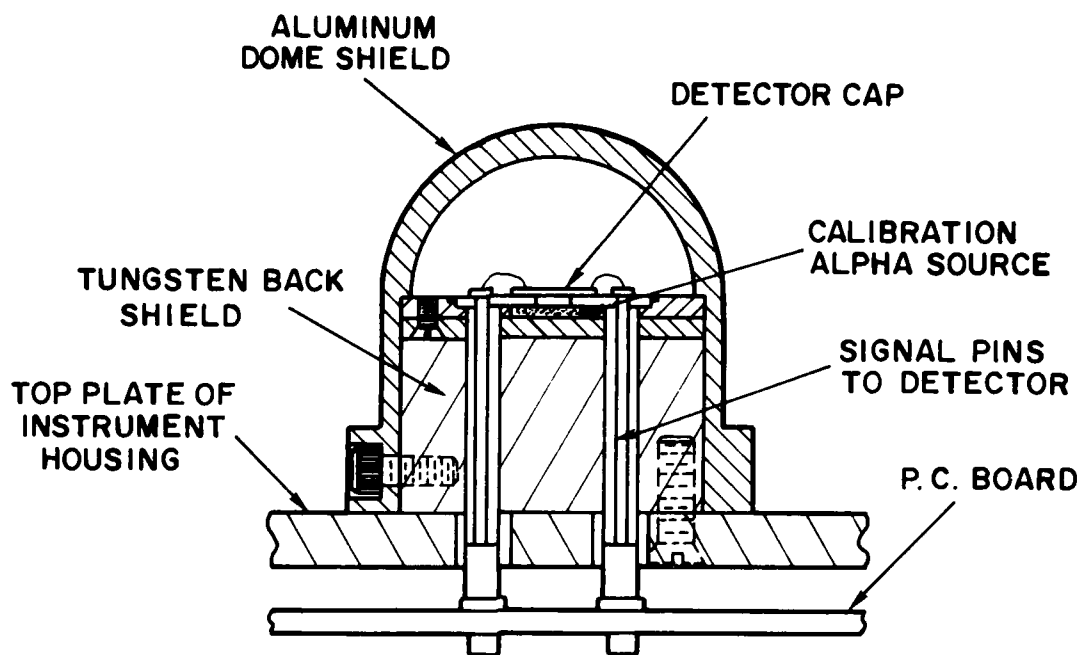


Figure 56. Schematic Diagram of One of the Four Sensors of the Space Radiation Dosimeter

shields are chosen to provide electron energy thresholds for the four sensors of 1, 2.5, 5, and 10 MeV, and for protons of 20, 35, 51, and 75 MeV. The 1-MeV threshold sensor has a detector area of 0.051 cm^2 , and the remaining three each have areas of 1.00 cm^2 . Particles that penetrate the shield and bremsstrahlung produced in the shield that impact the active element will both deposit energy in the device, producing a charge pulse. The charge pulse is shaped and amplified. The pulse height is proportional to the energy deposition in the detector.

Energy depositions between 50 keV and 1 MeV are summed to give the low linear energy transfer (LOLET) dose; depositions between 1 MeV and 10 MeV are summed to give the high linear energy transfer (HILET) dose; and depositions above ~ 40 MeV are counted as very high linear energy transfer (VHLET) events. The LOLET dose comes primarily from electrons, high energy protons (above 100-200 MeV), and bremsstrahlung. The HILET dose is primarily from protons below 100-200 MeV. The VHLET dose comes from nuclear star interactions of high energy protons, from heavier cosmic rays, and from the very small percentage of trapped radiation particles that have long path lengths in the detectors.

The dose is taken to be directly proportional to the total energy deposited in the detector. Each pulse is analyzed to determine whether it will be counted for electron or proton dose or a nuclear star event. The pulse height is then digitized

and added to the sum of all other pulse heights measured in the accumulation interval. In addition, the total number of pulses measured in the accumulation interval is also recorded for both electrons and ions. Without significant bremsstrahlung, this number of counts should be directly proportional to the integral flux of electrons and ions above the threshold produced by the aluminum shield.

We believe that the two lowest threshold detectors should provide both good flux and dose determinations, while the two remaining detectors will provide primarily dose data.

4. FUNCTION BLOCK DIAGRAM

A function block diagram is shown in Figure 57, where data flows from top to bottom. Particles or bremsstrahlung incident on the solid state component produce a charge proportional to the deposited energy. This charge is injected into a preamplifier. The resultant outputs are analog pulses with a peak voltage proportional to the injected charge. This analog signal is fed to the digitizer, which classifies the pulse as electron-, proton-, or nuclear star-induced, based on the level of deposited energy. Once classified, the peak voltage is quantized by 16 levels. In addition, for each event classified, a counter for electrons, protons, or nuclear stars is incremented. The pulses from the quantized peak voltage are fed to four additional counters, two for normal electron and proton dose, and one for calibration. The outputs from these counters are then multiplexed into the satellite telemetry.

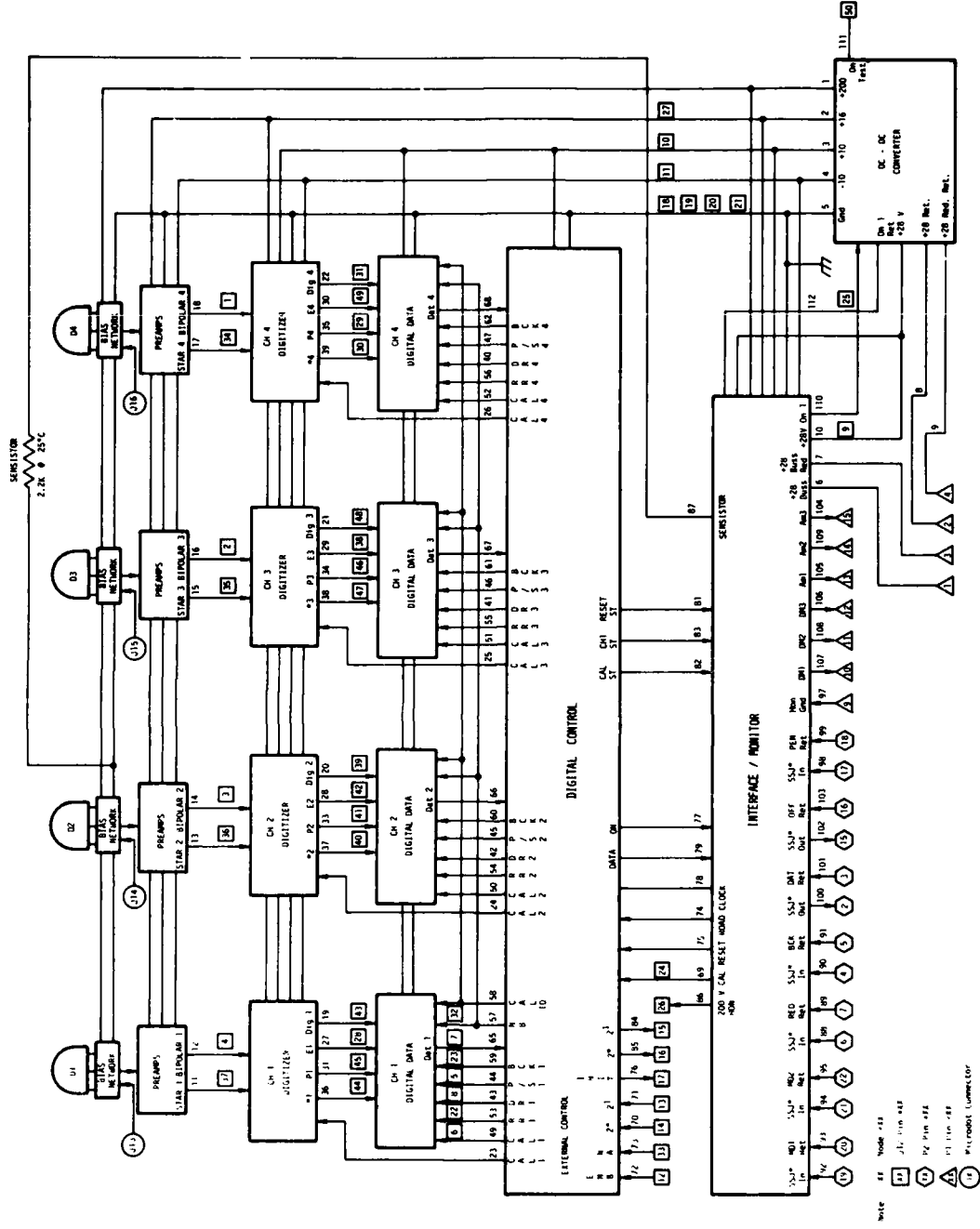


Figure 57. Function Block Diagram for the Space Radiation Dosimeter

References

1. Mozer, F.S., Elliott, D.D., Mihalov, J.D., Paulikas, G.A., Vampola, A.L., and Freden, S.C. (1963) Preliminary analysis of the fluxes and spectrums of trapped particles after the nuclear test of July 9, 1962, J. Geophys. Res. 68:641.
2. Paulikas, G.A., and Freden, S.C. (1964) Precipitation of energetic electrons into the atmosphere, J. Geophys. Res. 69:1239.
3. Paulikas, G.A., Blake, J.B., and Imamoto, S.S. (1975) ATS energetic particle radiation measurement at synchronous altitude, IEEE Trans. Aerospace and Electronic Systems (AES-11) 6:1138.
4. Gary, S.A., and Cashian, R.E. (1971) Solar Proton Monitor for TIROS-M and ITOS Spacecraft, COM-73-10138.
5. Grubb, R.M. (1975) The SMS/GOES Space Environment Monitor Sub-System, NOAA TM ERL SEL-42.
6. Pruett, B.G. (1980) Comparison of DMSP and NTS-2 dosimeter measurements with predictions, J. Spacecraft 17:270.
7. Sellers, B., Kelliher, R., Hanser, F.A., and Morel, P.R. (1981) Design, Fabrication, Calibration, Testing and Satellite Integration of a Space Radiation Dosimeter, AFGL-TR-81-0354, AD A113085.

Contents

1. Scientific Objectives	181
2. Application	181
3. Measuring Techniques	182
4. Function Block Diagram	182
Acknowledgments	184
References	185

19. The MOS Dosimeter (AFGL-701-3)

by

Leon S. August and James C. Ritter
Naval Research Laboratory
Washington, D.C. 20375

1. SCIENTIFIC OBJECTIVES

The objective of the Metal Oxide Semiconductor (MOS) Dosimeter is to measure integrated dose, D , as a function of depth in aluminum. Radiation soft PMOS transistors are placed beneath various thicknesses of aluminum to get the desired dose-depth curve. The integrated dose is determined by measuring the shift in transistor threshold voltage. The relationship between shift in threshold voltage and D is determined with a calibrated radiation source, usually Co-60 gamma rays.

2. APPLICATION

The first space-qualified integrating radiation dosimeter using a special MOS transistor was introduced by Holmes-Siedle as a consequence of work aimed at understanding and reducing the degradation of logic circuits containing MOS devices. High energy positive charges became stably trapped in the transistor, changing the threshold voltage for operation. For a P channel MOS, a direct measurement

of the threshold voltage can be made in a constant current circuit. Specifically, it is the voltage intercept at a drain current of $10\ \mu A$.¹

PMOS transistors can operate as a dosimeter in two ways. As originally designed,¹ the upper limit for expected total dose is 30 krad. A positive gate bias makes possible a total-dose measurement of 50 krad.² Extensive modification with source, drain, and gate grounded during irradiation but read out normally can increase the total-dose upper limit to 2.5 Mrad.³

In the package to be flown, four sensors (PMOS transistors) will be operated at positive gate biases. By using different thicknesses of aluminum above the sensors, a measure of the integrated doses caused primarily by electrons and protons at different depths is obtainable. This information is of substantial interest since even radiation soft devices flown in space survive for much longer than would be predicted from laboratory experiments and from the integrated dose predictions of the currently accepted space radiation models.

The integrated doses resulting primarily from electrons and protons can be compared with the calculations based on the currently employed space radiation models and the models to be developed based on the SPACERAD results. These results can also be compared with the results from the AFGL dosimeter (AFGL-701-2).

3. MEASURING TECHNIQUES

Measurement of the integrated dose is very simple. The parameter measured is the shift in threshold voltage, which is related to dose according to the relationship $\Delta V_T = R A D$. Since the threshold cannot be reset during flight, the total shift is measured as a function of time, and therefore provides a measure of integrated flux. In the above expression, R and A are constants to be determined in the laboratory. The closest similar technology is thermoluminescent dosimeters (TLDs). However, using TLDs in space does not appear practical.

4. FUNCTION BLOCK DIAGRAM

The principal circuit employed in the MOS dosimeter is illustrated in the

1. Adams, L., and Holmes-Siedle, A. (1978) The development of an MOS dosimeter for use in space, IEEE Trans. Nucl. Sci. NS-25:1607.
2. August, L.S. (1982) Estimating and reducing errors in MOS dosimeters caused by exposure to different radiations, IEEE Trans. Nucl. Sci. NS-29:2000.
3. August, L.S. (1984) Design criteria for a high-dose MOS dosimeter for use in space, IEEE Trans. Nucl. Sci. NS-31:801.

block diagram (Figure 58). The circuit provides the needed positive gate bias during the expose mode of operation and the constant current from source to drain through the PMOS transistor that determines the threshold voltage in the read mode. Similar circuits exist for each of the four PMOS transistors. VA is the analog voltage output that falls in the range from 0 to 5 V that is telemetered and from which the threshold voltage is determined.

In the expose mode, VREG is shorted to ground, and the offset voltage of the

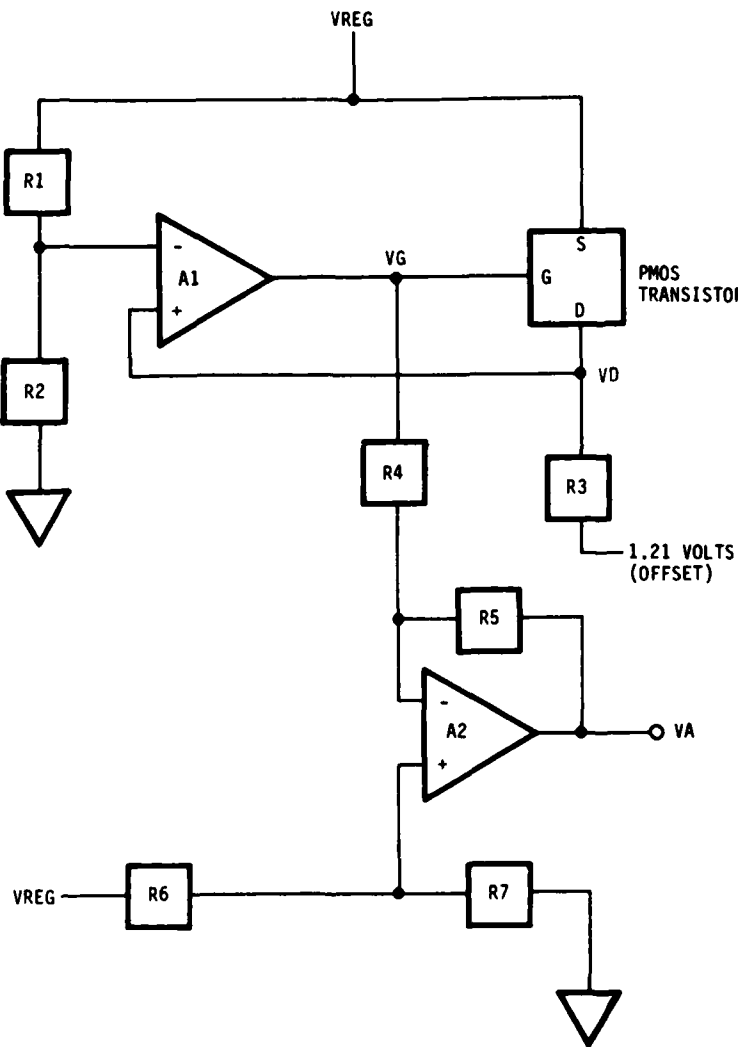


Figure 58. Function Block Diagram for the MOS Dosimeter

1.21 V from a Zener diode acts through R3 to cause the output of the operational amplifier A1 to saturate at a high value, and thereby applies a positive gate bias of 11.4 V.

In the read mode, the source to drain current flowing through the PMOS transistor is regulated by the output of A1, which is applied to the PMOS gate. Current regulation is achieved as follows: The drain voltage, V_D , of the PMOS transistor is applied to the positive (noninverting) input of A1. The output of the operational amplifier A1 seeks a level such that V_D is equal to the voltage at the negative (inverting) input to A1. The R's are resistors.

Further details pertaining to the flight instrument and circuitry are discussed by August et al.⁴

Acknowledgements

Thanks are due to A. Holmes-Siedle and G. Brucker for helpful discussions as well as assistance in acquiring suitable PMOS transistors. This research was funded by the Naval Electronic Systems Command, Code 615, under the NRL/-NAVELEX Spacecraft Survivability/Vulnerability Program.

4. August, L.S., Circle, R.R., Ritter, J.C., and Tobin, J.S. (1983) An MOS dosimeter for use in space, IEEE Trans. Nucl. Sci. NS-30:508.

References

1. Adams, L., and Holmes-Siedle, A. (1978) The development of an MOS dosimeter for use in space, IEEE Trans. Nucl. Sci. NS-25:1607.
2. August, L.S. (1982) Estimating and reducing errors in MOS dosimeters caused by exposure to different radiations, IEEE Trans. Nucl. Sci. NS-29:2000.
3. August, L.S. (1984) Design criteria for a high-dose MOS dosimeter for use in space, IEEE Trans. Nucl. Sci. NS-31:801.
4. August, L.S., Circle, R.R., Ritter, J.C., and Tobin, J.S. (1983) An MOS dosimeter for use in space, IEEE Trans. Nucl. Sci. NS-30:508.

END

FILMED

12-85

DTIC